CHARACTERIZATION OF TROPHOBLAST GLYCOPROTEIN

IN RETINAL ROD BIPOLAR CELLS

By

Colin M Wakeham

A DISSERTATION

Presented to the Neuroscience Graduate Program

Vollum Institute

And the Oregon Health & Science University School of Medicine

in partial fulfillment of the requirements for the degree of

Doctor of Philosophy

Table of Contents

List of Abbreviations

Abbreviation	Expanded Name
5T4	Trophoblast Glycoprotein
AII-AC	AII Amacrine Cell
A17-AC	A17 Amacrine Cell
AC	Amacrine Cell
AMPA	α-Amino-3-Hydroxy-5-Methyl-4-Isoxazoleproprionic Acid
BASP1	Brain Acid Soluble Protein 1
Bis-I	Bisindolylmaleimide I
BC	Bipolar Cell
BORG4	Binder of Rho GTPase 4
CACNA1S	Calcium Channel, Voltage-Dependent, L-Type, Alpha 1S Subunit
C_m	Membrane Capacitance
CNQX	Cyanquixaline
CPPG	(RS)-α-Cyclopropyl-4-phophonophenylglycine
CSNB	Congenital Stationary Night Blindness
CT	C-Terminal
CtBP2	C-Terminal Binding Protein 2
DAG	Diacylglycerol
DE	Differential Expression
ERG	Electroretinogram
INL	Inner Nuclear Layer
IPL	Inner Plexiform Layer
GABA	γ-Aminobutyric Acid
GCL	Ganglion Cell Layer
GPCR	G-Protein-Coupled Receptor
GPR179	G-Protein Receptor 179
HC	Horizontal Cell
KO	Knockout
L-AP4	L-2-Amino-4-Phosphonobutyric Acid (L-APB)
LC-MS/MS	Liquid Chromatography Tandem Mass Spectrometry
LRR	Leucine-Rich Repeat
mGluR6	Metabotropic Glutamate Receptor 6
NHERF1	Na^+/H^+ Exchange Regulatory Factor 1

NT	N-Terminal
OFF-BC	OFF-type Bipolar Cell
OMR	Optomotor Response
ON-BC	ON-type Bipolar Cell
ONL	Outer Nuclear Layer
OP	Oscillatory Potential
OPL	Outer Plexiform Layer
PBS	Phosphate-Buffered Saline
PDB	Phorbol 12,13-Dibutyrate
PKCα	Protein Kinase C-Alpha
PMA	Phorbol 12-Myristate 13-Acetate
PSM	Peptide Spectrum Match
RBC	Rod Bipolar Cell
RGC	Retinal Ganglion Cell
R_m	Membrane Resistance
RPE	Retinal Pigment Epithelium
R_s	Series Resistance
TMT	Tandem Mass Tag
TPBG	Trophoblast Glycoprotein
TPMPA	(1,2,5,6-Tetrahydropyridin-4-yl)Methylphosphinic Acid
TRPM1	Transient Receptor Potential Melastatin-1
WAIF1	Wnt-Activated Inhibitory Factor 1 (Trophoblast Glycoprotein)
WT	Wild Type

List of Figures

Figure 4.12: Figure Supplement 3: TPBG Does Not Alter the RBC Voltage-Current Relationship in RBCs

Acknowledgements

Abstract

Rod bipolar cells (RBCs) are the first interneurons in the primary rod visual pathway. RBCs transmit light-driven signals from rods in the outer retina and contribute to retinal output through downstream amacrine cells (ACs) in the inner retina. This thesis presents my work identifying and characterizing trophoblast glycoprotein (TPBG), a leucine-rich repeat transmembrane protein recently identified in RBCs. Similar leucine-rich repeat proteins in RBCs are essential for synaptic targeting, correct localization of signal transduction proteins, and regulating the RBC light response across different light intensities. In Chapter 1, I introduce the neural organization of the retina and the mechanisms of synaptic transmission in the rod-RBC-AC circuit. I then summarize the evidence supporting the role of PKCα in modulating RBC activity and survey the functions of other important leucine-rich repeat proteins in RBCs. In Chapter 2, we used a novel multiplexed tandem mass tagged proteomics approach we used to identify TPBG as a PKCα-dependent phosphoprotein in mouse RBCs. Because TPBG had not yet been characterized in the retina, in Chapter 3 we examined TPBG localization and expression patterns in development and in the adult retina using immunolabeling techniques. We found that TPBG is highly enriched in the dendrites and axon terminals of RBCs and in the projections of a novel class of amacrine cells. TPBG expression in RBCs is abolished in the absence of TRPM1, the primary signal transduction channel in RBC dendrites. In the developing retina, TPBG expression increases dramatically just before eye opening, similar to TRPM1. In Chapter 4, we used immunofluorescence and electrophysiology to investigate the consequences of genetic deletion of TPBG in RBCs. We found that TPBG is not required for the development of normally functioning synapses between rods and RBCs in the outer plexiform layer, but we did find that TPBG knockout impairs vesicle exocytosis efficiency and glutamate release in RBC axon terminals in the inner plexiform layer. Finally, Chapter 5 discusses potential next steps in the study of TPBG and PKCα in RBCs. Overall, our results suggest that TPBG is required for efficient synaptic transmission between RBCs and downstream amacrine cells and is critical for normal retinal signaling.

Chapter 1: Introduction

Accurate processing of external stimuli is essential for survival. Organisms interact with the world through complex sensory systems that collect information from the surrounding environment and use it to shape appropriate behavioral responses. One ubiquitous external cue, light, has been instrumental in the behavioral and physiological evolution of most types of organisms since the beginning of life on Earth. Photosynthetic cyanobacteria migrate toward light to increase their photosynthetic yield in a process called phototaxis, whereas unicellular bacteria-devouring protists move toward light to access more food [1]. Plants have a similar mechanism, called phototropism, where they orient their leaves to maximize sun exposure [2]. Animals have developed a wide range of light-sensing organs, from the small pigmented eye-spots in flatworms to the multifaceted compound eyes of insects. Light-sensing in mammals and birds has evolved to a new level with the development of large complex eyes and multi-layered retinas that can isolate and process all of the salient features of the environment simultaneously and recombine them into an accurate and reproducible representation of the surrounding world [3,4].

The mammalian retina is a self-contained set of interconnected circuits with one input (light), one output (the optic nerve), and no neuronal feedback from the rest of the brain. It contains only three layers of neurons, but is capable of complex processing despite this relative structural simplicity [5,6]. The retina is easily accessible to experimental manipulation and can be isolated from the eye intact without disrupting any internal connections between neurons. It is an optically transparent tissue, making imaging and targeting specific cell types for electrophysiological experimentation relatively straightforward. Finally, with the advent of advanced morphological, genetic and functional techniques, researchers are honing in on a complete atlas of discrete cell-types [7]. Thus, the retina is a powerful model tissue that can provide vital insight into the molecular mechanisms and circuit function of the nervous system.

Organization of the Retina

The mammalian retina contains at least 100 distinct neuronal cell-types assembled in a stereotyped, laminar arrangement. The five major classes of retinal neurons are organized into three neuronal layers and each class is localized to a specific layer: photoreceptors stratify to the outer nuclear layer (ONL); bipolar cells, horizontal cells, and amacrine to the inner nuclear layer (INL); and ganglion cells and displaced amacrine cells to the ganglion cell layer (GCL). Between the three neuronal layers are the two plexiform layers where cells form synaptic connections with each other (**Figure 1.1**). Photoreceptors project into the outer plexiform layer (OPL) where they synapse with bipolar cell dendrites and horizontal cells. Horizontal cells project laterally across

the OPL and modulate photoreceptor-to-bipolar cell synaptic transmission via feedback inhibition. Bipolar cell axons then project into the inner plexiform layer (IPL) where they form synapses with ganglion cells and amacrine cells. Amacrine cell output modulates synaptic transmission in the IPL. Finally, ganglion cell axons project into the nerve fiber layer and exit the retina as the optic nerve. Generally, the photoreceptors, bipolar cells, and ganglion cells form a vertical excitatory transduction pathway that passes light-dependent information through the retina to the optic nerve and visual centers of the brain. Horizontal cells and amacrine cells provide lateral inhibition to the cells of the vertical pathway, allowing for the encoding of different aspects of the visual scene [6,8,9].

Photoreceptors (**Figure 1.1; blue**), the sensory cells of the retina, transform the energy from light into electrochemical signals by absorbing incident photons with photosensitive proteins called opsins. There are two main subclasses of photoreceptor, the rods and cones, which differ in sensitivity to light intensity and wavelength. Rods are extremely sensitive to low intensity light, and can even respond to single photons, so are useful for dark (scotopic) nighttime vision such as on a moonless night [10,11]. All rods contain a single type of opsin, rhodopsin, and therefore provide achromatic output. Cones are less sensitive than rods, but saturate at much higher intensities and provide useful daytime (photopic) vision. Different cones contain opsins with distinct absorption spectra, and differential excitation of cones can be interpreted by downstream neurons as color. Under mid-range (mesopic) lighting conditions, such as nighttime on a lit street, a combination of rods and cones support vision. Both rod and cone axon terminals contain specialized structures called synaptic ribbons at their active zones that promote fast, precise, and sustained neurotransmitter release over a wide range of light intensities [12,13].

Photoreceptor output to downstream bipolar cells in the OPL is augmented by horizontal cells (HCs; **Figure 1.1; magenta**), which provide negative feedback inhibition to photoreceptor axon terminals and negative feedforward inhibition to bipolar cell dendrites [14,15]. The retinas of most mammalian species contain two subtypes of HCs: A-type and B-type (also called H1 and H2 in some species). A-type HCs do not contain axons whereas B-type ACs do [16]. In mammals, the dendrites of both types of HCs contact cones, but only the axons of B-type HCs contact rods [17]. HCs form lateral networks of inhibition across the OPL via gap junction coupling that enhances edge detection through a process of surround inhibition, creating the center-surround properties of bipolar cells that act to maximize contrast and acuity [18,19]. HCs also function to adjust the overall gain of the outer retina to be within the operating range of inner retinal neurons [20].
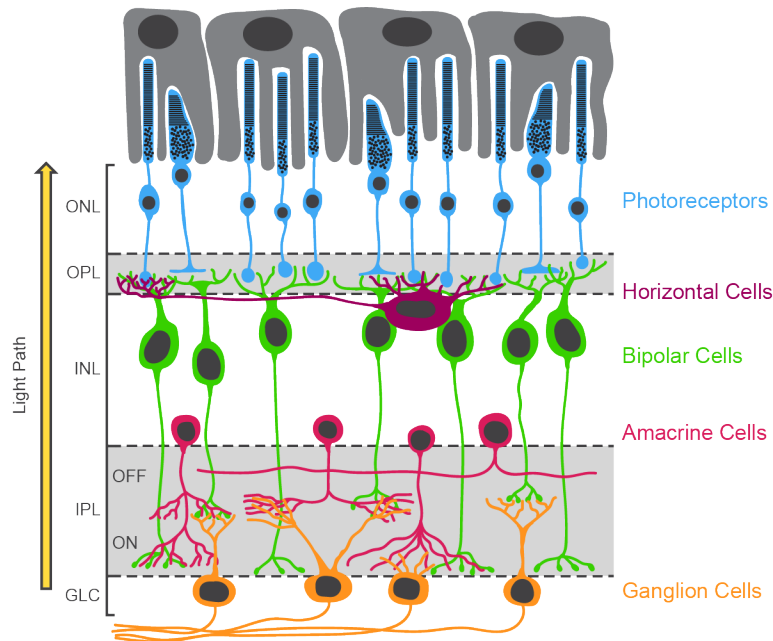
Figure 1.1: Organization of the retina. The retina is a highly laminated structure consisting of three neuronal layers separated by two synaptic layers (**light gray background**). In the back of the eye are the photoreceptors (**blue**) where phototransduction occurs. Photoreceptor cell bodies are located in the ONL and their axons project into the OPL where they form synapses with bipolar cell dendrites. Bipolar cells (**green**) are located in the INL and project their axons into the IPL where they form synapses with ganglion cells (**orange**). Ganglion cells are located in the GCL and their axons form the optic nerve. These cells constitute the excitatory vertical transduction pathway. There are also two classes of inhibitory interneurons in the retina. Horizontal cells (**magenta**) are localized to the top of the INL and project laterally across the OPL and amacrine cells (**pink**) are localized to the bottom of the INL and project laterally across the IPL. There are also some displaced amacrine cells which are localized to the GCL. ONL: outer nuclear layer; OPL: outer plexiform layer; INL: inner nuclear layer; IPL: inner plexiform layer; GCL: ganglion cell layer.

Bipolar cells (BCs; **Figure 1.1; green**) are the first interneurons in the vertical pathway and are responsible for sampling photoreceptor output and distributing it into ON and OFF visual streams: the ON pathway is excited by light increments and the OFF pathway is excited by light decrements. ON and OFF signals are generated in BCs by the expression of different glutamate receptors in their dendrites. There are currently 15 genetically identified subtypes of BCs in mice, including nine ON-type BCs (ON-BCs) and six OFF-type BCs (OFF-BCs). Of the 15 BC subtypes, 14 of them sample from cone photoreceptors and only one, the rod bipolar cell (RBC), is an ON-BC that samples directly from rod photoreceptors [21,22]. Bipolar cells differ in their connectivity to photoreceptors and postsynaptic targets. One BC samples directly from rods (the rod bipolar cell), others from cones, and some receive mixed rod-cone input. Among cone BCs, some receive input from specific cone subtypes and others are nonselective [23–25]. Bipolar cell axons stratify to different layers (sublamina) of the IPL depending on their light responses and their downstream amacrine cell or ganglion cell targets: OFF-BCs project to sublamina 1 and 2 in the proximal IPL and ON-BCs project to sublamina 3-5 in the distal IPL [26]. Like photoreceptors, BCs form ribbon

synapses, allowing for rapid and sustained neurotransmitter release over a large range of light intensities [12].

Amacrine cells (ACs; **Figure 1.1; pink**) are the most diverse class of retinal neurons, with at least 45 subtypes based on morphological and connectome analyses [26–29] and 63 subtypes identified in mice using high-throughput single-cell RNA sequencing [30]. Although ACs perform many functions, one primary role is to decorrelate visual feature representations present in upstream BCs and shape the feature selectivity and receptive fields of downstream ganglion cells [31]. One specialized AC, the AII amacrine cell (AII-AC) is responsible for the transfer of signals between rod and cone visual streams via crossover excitation and inhibition [32]. The AII-AC is the primary means by which RBCs transmit rod-driven signals to ganglion cells.

Retinal ganglion cells (RGCs; **Figure 1.1; orange**) are the only output neurons of the retina and therefore must be able to encode all of the salient components of the visual field. Each of the approximately 30 subtypes of RGC in mice are sensitive to distinct visual features, including color, contrast, and direction and speed of object motion [33]. The ON and OFF streams from bipolar cells are maintained in the ganglion cell layer as some RGC dendrites stratify to either the ON or the OFF sublamina of the IPL. Other RGCs are bistratified, meaning they project to both layers and therefore encode both ON and OFF signals. RGCs are also responsible for converting the graded potentials of most retinal neurons into action potentials that can be interpreted by downstream brain regions for further processing. Intrinsically photosensitive RGCs (ipRGCs) are a special type of ganglion cell containing the photopigment melanopsin that project to the hypothalamus, the thalamus, the amygdala, and the midbrain. ipRGCs encode ambient light intensities to synchronize circadian rhythms and contribute to the pupillary light reflex [34].

Circuitry and Signal Transduction of the Rod-RBC-AII Pathway

Rods detect photons and convert them into electrochemical signals by phototransduction in specialized finger-like projections called outer segments. Rod outer segments are packed with the G protein-coupled receptor rhodopsin, each of which is covalently bound to the chromophore retinal. Retinal is bound in the 11-*cis* conformation, but the absorption of an incident photon causes the 11-*cis*-retinal to isomerize to all-*trans*-retinal, which induces a conformational change in rhodopsin and initiates a G-protein signal transduction cascade. Activated G-proteins inhibit the production of cyclic-GMP, which in turn causes the deactivation of cyclic-GMP-gated cation channels and subsequent rod hyperpolarization [35,36]. Hyperpolarized rods release less of the neurotransmitter glutamate, therefore tonic glutamate release in the OPL is reduced by light.

RBCs contribute to the majority of rod-driven scotopic vision. In the OPL, RBC dendrites insert into rod axon terminals (spherules) in close proximity to the site of glutamate release, with each spherule containing a single invagination with two HC axons and two RBC dendrites [37,38] (**Figure 1.2A and B**). RBCs, like all ON-BCs, *depolarize* in response to photoreceptor *hyperpolarization* and the concomitant reduction in glutamate release due to a unique, sign-inverting G protein-mediated signal transduction cascade [39]. Glutamate release from photoreceptors is detected by the metabotropic glutamate receptor mGluR6 [40–42] that is negatively coupled to the TRPM1 [43–45] cation channel. Thus, a light stimulus relieves tonic TRPM1 inhibition and permits cation influx and subsequent ON-BC depolarization (**Figure 1.2C**). Additional proteins implicated in the mGluR6-TRPM1 cascade include GPR179 [46–48], nyctalopin [49–51], and LRIT3 [52–54].
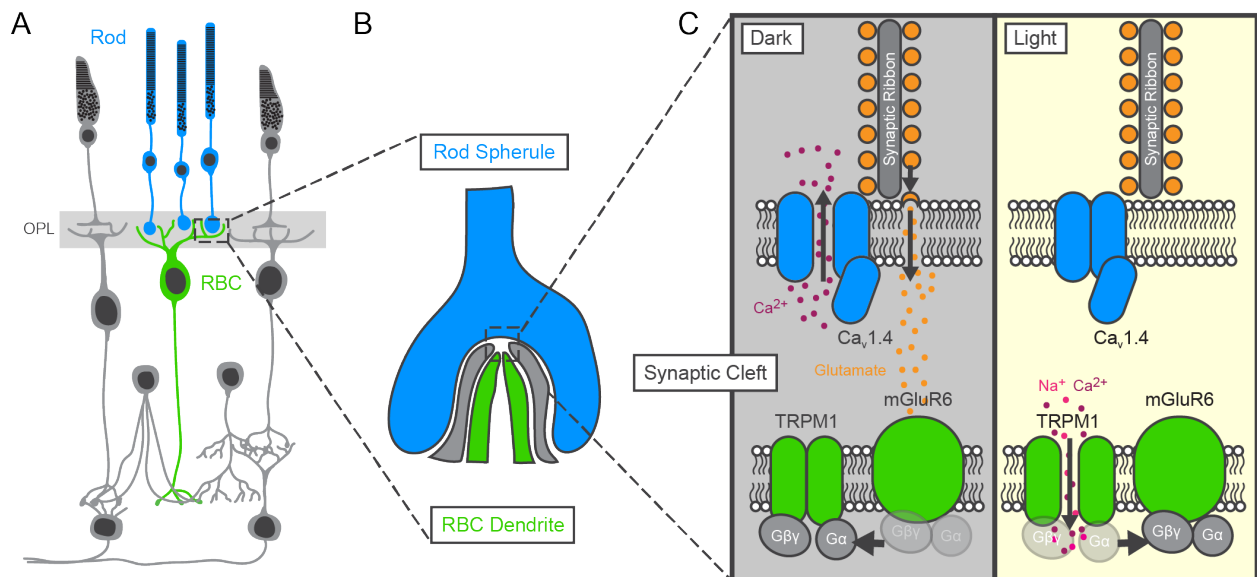
Figure 1.2: Signal transduction between rods and rod bipolar cells. **(A)** Rods signal to RBCs in a specialized rod spherule located in the OPL. **(B)** The rod spherule is invaginated by two HCs (**gray**) and two RBCs (**green**). Synaptic transmission occurs in the tips of the RBC dendrites directly opposite the synaptic ribbon. **(C)** In the dark (left), sustained release of glutamate by the rod is sensed by mGluR6, which releases the G-proteins G_α and $G_{\beta\gamma}$ to tonically inhibit TRPM1. The RBC remains hyperpolarized. In the light (right), the release of glutamate is relieved and the tonic inhibition of TRPM1 is relaxed. The influx of cations through TRPM1 causes the RBC to depolarize. RBC: rod bipolar cell; TRPM1: transient receptor potential melastatin-1.

Each RBC projects a narrow axon into sublamina 5 of the IPL that terminates in several large synaptic boutons (**Figure 1.3A**). An RBC bouton contains multiple stereotypical synapses each containing one RBC synaptic ribbon, one A17 amacrine cell (A17-AC), and one AII-AC. When a depolarized potential propagates into the RBC axon terminal (**Figure 1.3B**), L-type voltage-gated calcium channels open and the resulting influx of Ca^{2+} initiates vesicle fusion and

glutamate release into the dyad synapse [55–58]. Both AII-ACs and A17-ACs express calcium-permeable AMPA receptors (AMPARs) that detect the incoming glutamate and the resulting Ca^{2+} influx causes both ACs to depolarize[59,60]. In A17-ACs, this Ca^{2+} influx triggers the release of the neurotransmitter γ-aminobutyric acid (GABA) back into the synaptic cleft. GABA is detected by ionotropic $GABA_A$ and $GABA_A\rho$ receptors on the RBC axon terminal, which initiate an influx of Cl^- into the RBC terminal to produce a reciprocal inhibitory feedback circuit [59–65]. Reciprocal GABAergic inhibition by A17-ACs provides dynamic control of RBC output to AII-ACs and helps shape the receptive field properties of downstream neurons.
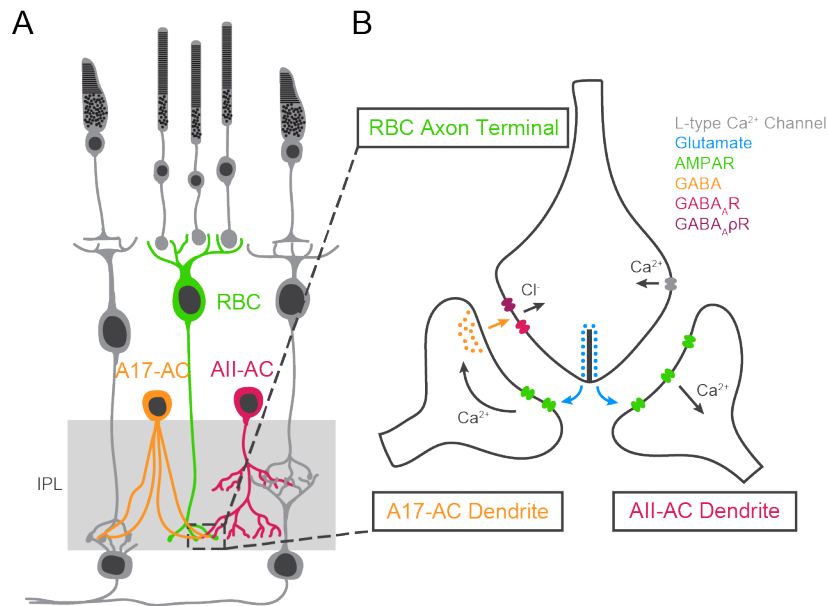
Figure 1.3: Signal transduction between rod bipolar cells and amacrine cells*. **(A)** RBCs project to the innermost IPL where they form synapses with A17-ACs and AII-ACs. **(B)** RBC depolarization results in Ca^{2+} influx through L-type voltage-gated Ca^{2+} channels that initiates vesicle fusion and glutamate release into the synaptic cleft. Glutamate is detected by Ca^{2+}-permeable AMPARs in A17- and AII-AC dendrites. Ca^{2+} influx into A17-ACs results in GABA release back into the synaptic cleft that is detected by GABA receptors in RBC terminals, forming an inhibitory reciprocal feedback circuit. RBC: rod bipolar cell; AC: amacrine cell.

AII-ACs are narrow-field bistratified ACs located in the distal INL near the INL/IPL border. AII-AC dendrites project to the ON and OFF sublamina of the IPL where they form gap junction-mediated electrical synapses with ON-cone BCs [32,66,67] and inhibitory glycinergic synapses with OFF-cone BCs [68]. AII-ACs form the primary link between the rod and cone visual pathways by transferring excitatory responses to the ON-cone channel and simultaneously inhibiting the OFF-cone channel (**Figure 1.4**). The reverse is also true: a hyperpolarized AII-AC will reduce its excitatory input to the ON-cone channel and reduce its inhibitory input to the OFF-cone channel. Although evidence indicates that AII-ACs most commonly synapse with Type 2 OFF-cone BCs and Type 6 ON-cone BCs, synaptic connections have been found between AII-ACs and nearly

all cone BCs [22], suggesting that AIIs distribute rod-driven signals to most if not all RGC subtypes. Because RBCs do not make any known direct connections to RGCs, AII-ACs form the sole link between RBCs and retinal output.
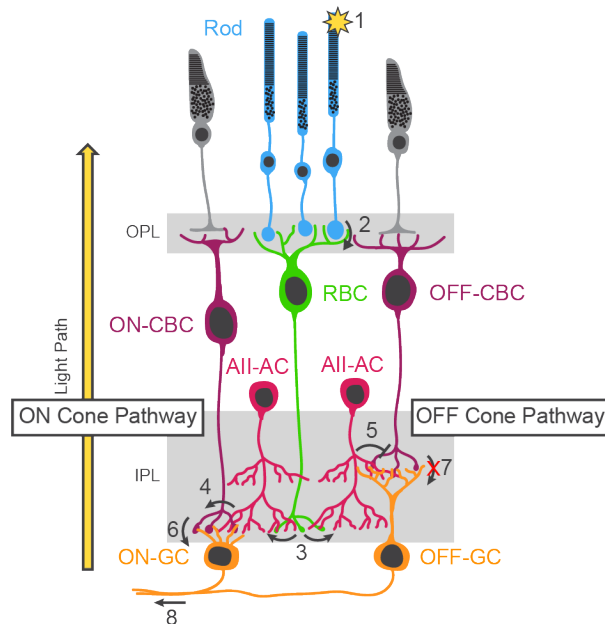
Figure 1.4: A summary of the rod visual pathway. **(1)** Photons are absorbed in the rod outer segment causing hyperpolarization and **(2)** relief of rod-driven tonic glutamatergic inhibition of RBCs. **(3)** RBCs provide excitatory input to AII-ACs that provide **(4)** gap-junction-mediated excitatory input to ON-CBCs and **(5)** glycinergic inhibition to OFF-CBCs. **(6)** ON-CBCs provide excitatory input to ON-GCs and **(7)** input to OFF-GCs from OFF-CBCs is suppressed by inhibition from AII-ACs. Finally, **(8)** ON signals are transmitted to the visual centers of the brain through the optic nerve. Though two AII-ACs are shown in this figure, a single AII can mediate connections to both cone streams. RBC: rod bipolar cell; AII-AC: AII amacrine cell; ON-CBC: ON-type cone bipolar cell; OFF-CBC: OFF-type cone bipolar cell; ON-GC; ON-type ganglion cell; OFF-GC: OFF-type ganglion cell.

The Modulation of Rod Bipolar Cells by Protein Kinase C-Alpha

RBCs are the first interneurons in the rod visual pathway, the primary pathway for low-light, achromatic vision. Because they serve as the only dedicated bipolar cell in the rod pathway, they must be able to encode all modalities of rod-dependent signals. Despite being colloquially known for night vision, rods actually operate over a 6 log-unit range of light intensities. Due to converging inputs from 20 – 40 rods, each RBC has an even larger dynamic range and operates throughout the full range of light conditions [69]. Rods saturate after moderate light intensities [70], but RBCs maintain the ability to encode contrast even in brighter light conditions through its connections to the cone pathway [71]. In daylight, RBCs convey cone-driven HC-mediated surround inhibition to the inner retina [72]. Therefore, RBCs are able to shift between different operational modes depending on the light intensity.

The wide dynamic range in RBC light responses suggests that RBCs have active mechanisms to alter their responses across light conditions. To date, an exact mechanism for this

regulation has not been clearly established, but evidence suggests an important role for protein kinase C-alpha (PKCα). PKCα is a serine-threonine protein kinase and is a potent activator of many cell signaling pathways [73]. Although PKCα is constitutively expressed in most tissues and cell-types, it is highly enriched specifically in RBCs and has been used as an immunofluorescent RBC marker for decades [74–76]. PKCα is activated by a coincident increase in intracellular Ca^{2+} and by binding to diacylglycerol (DAG), thus PKCα can be recruited to the membrane and activated by DAG analogues such as phorbol esters [77].

Distribution of PKCα to both the dendrites and synaptic terminals of RBCs suggests it is likely to have compartment-specific functions and potentially multiple complex effects on RBC physiology. The first evidence that PKCα regulates RBCs came from a set of studies using phorbol 12-myristate 13-acetate (PMA) and the PKCα inhibitor bisindolylmaleimide I (bis-I) to control PKCα activity in RBC axon terminals. These studies found that the reserve component of glutamate vesicle release is potentiated by the application of PMA and that this potentiation is reversed by bis-I. Since only the reserve component of vesicle release was affected, rather than the ready releasable pool, the authors hypothesize that PKCα may be involved in the replenishment of synaptic vesicles to the synaptic ribbon [78–80]. PKCα also regulates F-actin polymerization in synaptic terminals. Phorbol esters accelerated the growth of F-actin filaments in the terminals, whereas PKCα inhibitors blocked F-actin growth [81]. F-actin is required for synaptic vesicle trafficking and release, so these authors hypothesized that PKCα may regulate synaptic vesicle release through manipulation of actin dynamics [82]. These studies indicate that PKCα kinase activity may enhance RBC glutamate release.

PKCα also regulates GABA receptor responses in RBC synaptic terminals. The application of the phorbol esters PMA and phorbol 12,13-dibutyrate (PBD) significantly attenuated GABA$_A$-mediated Cl$^-$ currents to a puff of GABA in the IPL. The PKCα inhibitor calphostin C had no direct effect on GABA$_A$ responses, but prevented the effect of PBD [83]. PMA also downregulated GABA$_A\rho$ (GABA$_C$) receptors that could be reversed by the PKCα inhibitor tamoxifen and by the intracellular introduction of phosphatase through a patch pipette [84]. These two studies support the hypothesis that PKCα activation reduces inhibitory reciprocal feedback through postsynaptic GABA receptors.

Additionally, PKCα regulates the initiation of the RBC light response by altering whole-cell TRPM1 cation channel currents. Bath application of diC8-PIP$_2$, a drug that reduces DAG production, depressed TRPM1 currents, whereas the DAG analogue 2-acetyl-1-oleoyl-sn-glycerol (OAG) potentiated them. This effect was observed in RBCs, but not in ON-cone bipolar cells,

which also express TRPM1 but not PKCα. The potentiating effect of OAG was not observed in PKCα knockout RBCs or when PKCα was blocked with a PKC inhibitory peptide. The authors also found that PKCα relieves intracellular magnesium-dependent TRPM1 inactivation [85].

Finally, there have been two major studies examining the effects of PKCα knockout on the scotopic electroretinogram (ERG), an electrophysiological technique that records RBC activity *in vivo*. In one study, PKCα knockout delayed both the rising and falling phases of the scotopic ERG b-wave, indicating that PKCα shapes RBC output by influencing both the activation and termination of the RBC light response [86]. The second study reported that PKCα knockout increases the amplitude and duration of the scotopic ERG b-wave, but this effect was only apparent after progressively brighter stimulus intensities, suggesting that PKCα suppressed the RBC light response in a light intensity-dependent manner [87].

Overall, previous work examining PKCα in RBCs paints a complex picture consistent with multiple functions of PKCα in different RBC compartments. Studies in RBC synaptic terminals indicate that PKCα increases RBC synaptic vesicle release and independently attenuates the reciprocal feedback current through GABA receptors. In RBC dendrites, PKCα enhances TRPM1 conductance by relieving magnesium-dependent inhibition. This work suggests that PKCα has a potentiating effect on the RBC light response. However, ERG studies using PKCα knockout mice indicate that PKCα might have an overall suppressive effect on RBC activity. The disparity between these results could be due to different experimental methods used. Pharmacological methods using patch clamp electrophysiology have the advantage of isolating the synapses and channels of interest and preventing compensation. ERG recordings, on the other hand, do not attempt to isolate specific mechanisms, but contain the sum total of all PKCα-mediated effects, including potential network effects, and present a more holistic picture of RBC activity that can be better extrapolated to behavior. Both techniques are useful in helping uncover the complex roles of PKCα in RBC physiology, but specific mechanisms remain unclear. In Chapter 2, we identify a new PKCα-dependent leucine-rich repeat phosphoprotein in RBCs that may help elucidate the function of PKCα in the retina.

Leucine-Rich Repeat Proteins Regulate Synapse Formation and Function

Leucine-rich repeat transmembrane proteins form a large family containing over 300 members across all domains of life, from viruses to eukaryotes. Different classes of leucine-rich repeat proteins are involved in diverse functions including cell adhesion, synapse formation, DNA repair, DNA and RNA processing, and immunity, but all share a conserved structural motif called

a leucine-rich repeat (LRR) domain [88]. A leucine-rich repeat domain contains between 2 and 45 repeated tandem LRR sequences (LxxLxLxxN/CxL) of 20 to 30 amino acids each [89,90]. The LRR motifs are always extracellular and are arranged in a stereotypical "α/β horseshoe fold" with an outer convex face of α-helices, an inner concave face of β-sheets, and a hydrophobic leucine-rich interior core. LRR motifs are usually flanked by N-terminal and C-terminal repeats enriched in cysteine residues. Despite suspected separate evolutionary lineages, the major function of all LRR domains is thought to be protein-protein interactions [88–90]. The number of LRR motifs in different proteins dictates the length and curvature of the horseshoe and contributes to the diversity of binding partners [90]. This section will examine four LRR protein families expressed in the retina that are critical to cell morphology and the development and maintenance of functional synapses. Unsurprisingly, mutations in the genes coding for these LRR proteins are often associated with disrupted vision in humans.

Nyctalopin (often referred to in the literature by its gene name *Nyx*) is a glycosylated LRR protein with eleven LRR sequences that is localized to the tips of ON-bipolar cell dendrites. Unlike most LRRs, nyctalopin does not have a transmembrane domain and instead is anchored to the membrane with a glycosylphosphatidylinositol (GPI) anchor [91]. It was the first LRR discovered in the retina and was identified in a screen for gene mutations associated with congenital stationary night blindness (CSNB), a human disease affecting ON pathway function [92,93]. Derived from the clinical term for night blindness (nyctalopia), early examination of nyctalopin mutations established a characteristic *nob* (**no** ERG **b**-wave) phenotype, indicating that nyctalopin is required for ON-bipolar cell signaling [51,94]. Initial immunofluorescent analysis of *nob* mice found a normal distribution of synaptic transmission proteins in both photoreceptor axon terminals (bassoon and $Ca_v1.4$) and ON-bipolar cell dendrites (mGluR6, PKCα, and the G-protein Gα_o), suggesting that nyctalopin is not required for the normal localization patterns of these proteins [95]. Only when TRPM1 was identified was a role for nyctalopin discovered. Two separate groups used immunoprecipitation and yeast two-hybrid techniques to establish TRPM1 as a nyctalopin binding partner. TRPM1 is absent from ON-bipolar cell dendrites in nyctalopin knockout mice, though nyctalopin distribution is normal in the TRPM1 knockout, suggesting that nyctalopin is required for the localization of TRPM1 but not the reverse [49,50]. Furthermore, nyctalopin interacts with mGluR6, indicating these three proteins may form a large macromolecular signaling complex [49].

The leucine-rich repeat, immunoglobulin-like domain and transmembrane domain-containing (LRIT) family of LRR proteins contains three members (LRIT1-3). All three LRIT proteins contain an immunoglobulin-like domain and a fibronectin type III domain. LRIT1 and LRIT3 both contain five LRR sequences and their intracellular C-terminal tails are capped with

PDZ-interacting motifs. LRIT2 contains only four LRRs and lacks the C-terminal binding domain [96]. LRIT1 was identified by two groups using microarray and proteomics approaches and was found in cone synaptic terminals. One group found that LRIT1 forms trans-synaptic interactions with mGluR6 in ON-cone bipolar cells [97], whereas the other group identified the cone scaffold protein FRMPD2 as part of the LRIT1-mGluR6 trans-synaptic complex [96]. Both groups found morphological and visual deficits in LRIT1 knockout retinas, suggesting that LRIT1 is required for synapse formation between cones and ON-cone bipolar cells [96,97]. LRIT2, on the other hand, was localized to ON-bipolar cells and was found to be dispensable for photoreceptor synapse formation. LRIT2 immunoprecipitates with both LRIT1 and mGluR6, supporting its inclusion in the growing trans-synaptic mGluR6 anchoring complex [96]. LRIT3 was initially discovered in a screen for genes associated with CNSB [98]. Although early immunofluorescent studies indicated that LRIT3 was localized to ON-bipolar cell dendrites [54], more recent *in situ* hybridization experiments found LRIT3 transcripts in rod photoreceptors. Furthermore, rod-specific viral expression of LRIT3 in LRIT3 knockout mice recapitulated normal LRIT3 expression patterns in the OPL [52]. Like nyctalopin, LRIT3 knockout results in a *nob* phenotype and completely abolishes ON pathway signaling. Also, like nyctalopin, LRIT3 is required to localize TRPM1 to the dendritic tips of ON-bipolar cells [54], but its presynaptic location suggests trans-synaptic interactions [52]. A recent study found that LRIT3 is required for nyctalopin expression [99].

The extracellular leucine-rich repeat and fibronectin type III domain-containing (ELFN) family of cellular adhesion proteins consists of two paralogs: ELFN1 and ELFN2. ELFN proteins are heavily glycosylated and, as the name suggests, contain five extracellular N-terminal LRR sequences and a fibronectin type III domain. ELFN1 was first identified in the retina using an unbiased proteomics screen for proteins that immunoprecipitated with mGluR6. ELFN1 is expressed in rods, suggesting that it forms a trans-synaptic complex with mGluR6 at the rod-to-RBC synapse. Knockout of ELFN1 in mice abolished the scotopic ERG b-wave (the aforementioned *nob* phenotype), however, the scotopic a-wave and photopic responses were maintained, suggesting that ELFN1 is required for the RBC-specific light response. Electron micrographs found that synaptic contacts between rods and RBCs are significantly disrupted in the ELFN1 knockout [100,101]. ELFN2, on the other hand, is localized exclusively to cones and forms a trans-synaptic complex with mGluR6 in ON-cone bipolar cells. Unexpectedly, ELFN2 knockout does not affect cone synapses, but instead results in compensatory expression of ELFN1 in cones. Only double knockout of both proteins abolishes ON-cone bipolar cell light responses. Further analysis found that ELFN1 is expressed in developing cones, but is replaced by ELFN2 as the cones mature [102,103]. Overall, these data suggest that ELFN1 alone is required for the

development and maintenance of rod to RBC synapses, but cone to ON-cone bipolar cell synapses require the dynamic temporal expression of both ELFN1 and ELFN2.

The leucine-rich repeat transmembrane neuronal (LRRTM) family contains four members, though only LRRTM4 has been characterized in the retina. LRRTM4 contains ten LRR domains and was localized to RBC dendritic tips. Based on immunoprecipitation, the extracellular domain of LRRTM4 interacts with pikachurin, a heparan sulfate proteoglycan component of the extracellular matrix between photoreceptors and ON-type bipolar cells that forms a bridge between presynaptic dystroglycan and postsynaptic GPR179. In the OPL, knockout of LRRTM4 resulted in a slight reduction of GPR179, suggesting that LRRTM4 is yet another member of the trans-synaptic signaling complex between rods and RBCs [104]. Another group detected LRRTM4 in RBC axon terminals in the IPL colocalized with both $GABA_A$ and $GABA_{A}\rho$ immunofluorescence. In the IPL, knockout resulted in a reduction in the clustering of both GABA receptors as well as a disruption of the stereotypical dyad arrangement of the RBC synapse. RBC axon terminals are normally apposed by a single AII-AC and a single A17-AC. However, in the LRRTM4 knockout, the RBC axon was just as likely to be apposed by a single AC or even sometimes formed a triad synapse. The authors conclude that LRRTM4 is required for the organization of reciprocal $GABA_A$ and $GABA_{A}\rho$ synapses in RBC axon terminals and disruption of these inhibitory synapses in the knockout disturbs the development of the stereotypical arrangement of RBC dyad synapses [105].

LRR proteins in the retina are responsible for clustering critical synaptic signaling proteins and provide trans-synaptic contacts that promote the development and maintenance of synapses. In the next chapters, we examine the localization and expression patterns of the novel retinal LRR protein trophoblast glycoprotein (TPBG; Chapter 3). TPBG is a transmembrane protein with eight extracellular LRRs and we anticipate that the formation of extracellular interactions between TPBG's LRR domain and other proteins will be critical to its function. We also outline the proteomics technique we used to identify TPBG as a novel $PKC\alpha$-dependent phosphoprotein in RBCs (Chapter 2) and show that TPBG knockout results in reduced exocytosis and synaptic vesicle release (Chapter 4). Our results suggest that TPBG may provide a new link between $PKC\alpha$ and the regulation of RBC function.

Chapter 2: Manuscript I

Identification of PKCα-dependent phosphoproteins in mouse retina

Colin M Wakeham[1], Phillip A Wilmarth[2], Jennifer M Cunliffe[2], John E Klimek[2], Gaoying Ren[1], Larry L David[2,3], Catherine W Morgans[1]

[1]Department of Physiology and Pharmacology, Oregon Health and Science University, Portland, OR 97239, USA

[2]Proteomics Shared Resource, Oregon Health and Science University, Portland, OR 97239, USA

[3]Department of Biochemistry and Molecular Biology, Oregon Health and Science University, Portland, OR 97239, USA

Author contributions

Study design: CMW, LLD, CWM; Experimentation: CMW, JMC, PAW, GR, CWM**;** PAW Pipeline script development: PAW**;** Data analysis: CMW, PAW, JEK, LLD, CWM; Figure and manuscript preparation: CMW, JMC, PAW, JEK, LLD, CWM; Editing and review: CMW, JMC, PAW, GR, JEK, LLD, CWM; Repository preparation: CMW, PAW; Supplemental files preparation: CMW, PAW

Abstract

Adjusting to a wide range of light intensities is an essential feature of retinal rod bipolar cell (RBC) function. While persuasive evidence suggests this modulation involves phosphorylation by protein kinase C-alpha (PKCα), the targets of PKCα phosphorylation in the retina have not been identified. PKCα activity and phosphorylation in RBCs was examined by immunofluorescence confocal microscopy using a conformation-specific PKCα antibody and antibodies to phosphorylated PKC motifs. PKCα activity was dependent on light and expression of TRPM1, and RBC dendrites were the primary sites of light-dependent phosphorylation. PKCα-dependent retinal phosphoproteins were identified using a phosphoproteomics approach to compare total protein and phosphopeptide abundance between phorbol ester-treated wild type and PKCα knockout (PKCα-KO) mouse retinas. Phosphopeptide mass spectrometry identified over 1100 phosphopeptides in mouse retina, with 12 displaying significantly greater phosphorylation in WT compared to PKCα-KO samples. The differentially phosphorylated proteins fall into the following functional groups: cytoskeleton/trafficking (4 proteins), ECM/adhesion (2 proteins), signaling (2 proteins), transcriptional regulation (3 proteins), and homeostasis/metabolism (1 protein). Two strongly differentially expressed phosphoproteins, BORG4 and TPBG, were localized to the synaptic layers of the retina, and may play a role in PKCα-dependent modulation of RBC physiology. Data are available via ProteomeXchange with identifier PXD012906.

Significance

Retinal rod bipolar cells (RBCs), the second-order neurons of the mammalian rod visual pathway, are able to modulate their sensitivity to remain functional across a wide range of light intensities, from starlight to daylight. Evidence suggests that this modulation requires the serine/threonine kinase, PKCα, though the specific mechanism by which PKCα modulates RBC physiology is unknown. This study examined PKCα phosophorylation patterns in mouse rod bipolar cells and then used a phosphoproteomics approach to identify PKCα-dependent phosphoproteins in the mouse retina. A small number of retinal proteins showed significant PKCα-dependent phosphorylation, including BORG4 and TPBG, suggesting a potential contribution to PKCα-dependent modulation of RBC physiology.

Highlights

- PKCα is a major source of phosphorylation in retinal RBC dendrites and its activity in RBCs is light-dependent.

- Proteins showing differential phosphorylation between phorbol ester-treated wild type and PKCα-KO retinas belong to the following major functional groups: cytoskeleton/trafficking (4 proteins), ECM/adhesion (2 proteins), signaling (2 proteins), transcriptional regulation (3 proteins), and homeostasis/metabolism (1 protein).
- The PKCα-dependent phosphoproteins, BORG4 and TPBG, are present in the synaptic layers of the retina and may be involved in PKCα-dependent modulation of RBC physiology.

Introduction

Rod bipolar cells (RBCs) are key retinal interneurons in the rod visual pathway that receive light-driven synaptic input from rod photoreceptors and drive retinal output via synapses onto AII amacrine cells. RBCs serve different visual functions depending on luminance conditions. When dark adapted, they are able to transmit single photon responses [11,106], allowing for useful vision in starlight. RBCs are also able to transmit contrast changes against dim background light [71,107], and have recently been shown to influence vision in daylight [72]. Little is known about how RBCs adjust their sensitivity and gain to transition between these modes, but compelling evidence suggests phosphorylation by protein kinase C-alpha (PKCα) may play a role.

PKCα is a serine/threonine protein kinase that undergoes calcium-dependent translocation from the cytosol to the plasma membrane, where it is activated upon binding to diacylglycerol (DAG). It is a powerful modulator of signal transduction pathways and is so abundant in RBCs that it is used as a cell marker to identify RBCs with retinal immunofluorescence [74–76]. The light response of RBCs is reflected in the b-wave of the dark-adapted electroretinogram (ERG), and comparison of ERGs from wild type (WT) and PKCα knockout (PKCα-KO) mice reveal that genetic deletion of PKCα results in increases in both amplitude and duration of the scotopic b-wave [86,87]. This effect is particularly dramatic at brighter light intensities, suggesting that PKCα modulates the light response in an intensity-dependent manner. If the effect of PKCα on the light response is due to its kinase activity, then RBC proteins phosphorylated by PKCα are also likely to be involved in the modulation of RBC activity.

We used a multiplexed tandem mass tag (TMT; [108]) mass spectrometry-based phosphoproteomics approach to identify proteins that were differentially phosphorylated between WT and PKCα-KO retinas in order to gain insight into the biochemical mechanisms and pathways that mediate the effect of PKCα in RBCs. Phosphopeptide abundance is expected to be dynamic, so TMT acquisition methods that have improved accuracy and wider dynamic ranges are

necessary [109]. The larger number of replicates available with high-resolution instruments and TMT tags require improved data normalization and statistical testing methods, and we have successfully applied analysis techniques developed for large-scale protein expression studies [110] to phosphopeptide abundance data. Since PKCα-dependent changes in protein phosphorylation may be due to changes in total protein abundance, we also identified proteins that were differentially expressed between WT and PKCα-KO retinas.

Experimental Procedures

Experimental design and statistical rationale

For quantification of immunofluorescence (**Figure 2.2C**), we used retina sections from 4 WT and 3 TRPM-1-KO mice, each with 4 technical replicates. For the multiplexed TMT mass spectrometry experiments, we used 4 WT and 5 PKCα-KO mice. The 5 x 5 study design (one WT sample was lost) was the maximum number of samples accommodated by 10-plex TMT. For both total protein and phosphopeptide experiments, all nine samples were pooled after isobaric labeling and run simultaneously to reduce variability between samples. The statistical tests used are described within the Statistical analysis of differential expression section.

Animals

All studies were approved by the Institutional Animal Care and Use Committee at Oregon Health and Science University. Wild type mice used were C57BL/6J (Jackson Laboratory; Bar Harbor, ME, USA; Cat# 000664). The PKCα-KO mouse strain was B6;129-Pkrca*tm1Jmk*/J (Jackson Laboratory; Cat# 009068; [87]. The TRPM1-KO mouse strain was TRPM1*tm1Lex* (Texas A&M Institute of Genomic Medicine; College Station, TX, USA; [45].

PKCα activation by PMA treatment for immunoblotting or immunofluorescence

Freshly dissected retinas from WT and PKCα-KO mice were incubated at 37°C in 1 µM phorbol 12-myristate 13-acetate (PMA; Sigma-Aldrich; St. Louis, MO, USA; Cat# P8139) diluted in bicarbonate buffered Ames medium (US Biological Life Sciences; Salem, MA, USA; Cat# A1372-25) for 0 min, 15 min, 30 min, or 60 min. The retinas were then washed three times with Ames medium before being either fixed for cryo-sectioning or processed for western blotting.

Immunoblotting

Retinas were suspended in chilled lysis buffer (50 mM Tris pH 7.4, 150 mM NaCl, 1 mM EDTA, 1% Triton X-100, 1% deoxycholate, 0.1% SDS) with 1X protease/phosphatase inhibitor cocktail (Cell Signaling Technology; Danvers, MA, USA; Cat# 5872). The retinas were then homogenized and incubated on ice for 1 hour. Lysates were centrifuged for 15 min at 28,000 x g and 4°C, and the pellets discarded. Lysates were stored at -20°C. Equal quantities of WT and PKCα-KO retinal proteins were subjected to electrophoresis on precast NuPAGE 1mm 4-12% Bis-Tris gels (Thermo Scientific; Waltham, MA, USA; Cat# NP0322BOX). The separated proteins were transferred to polyvinylidene difluoride (PVDF) membranes and then blocked with Odyssey Blocking Buffer (LI-COR Biosciences; Lincoln, NE, USA; Cat# 927-50003) for 1 hr. The blots were probed with primary antibody for 1 hr at room temperature. The membranes were washed 3 x 5 min with TBST (Tris-buffered saline with 0.1% Tween-20) and then incubated for 1 hr at room temperature with secondary antibody and washed 3 x 5 min with TBST. Immunoreactive bands were visualized with a LI-COR Odyssey CLx Imaging System at 700 or 800 nm.

Primary antibodies used for immunoblotting were rabbit anti-PKC motif phosphoserine [(R/KXpSX(R/K)] MultiMab mAb mix (1:250; Cell Signaling Technology; Cat# 6967), mouse anti-Cdc42EP4 (1:1000; Thermo Fisher Scientific; Cat# MA5-21509), rabbit anti-Borg4 (1:200; Bethyl Laboratories; Montgomery, TX, USA; Cat# A302-379A), rabbit anti-5T4 (1:5000; Abcam; Cambridge, UK; Cat# ab129058), rabbit anti-NHERF1 (1:5000; Abcam; Cambridge, UK; Cat# ab3452). Secondary antibodies used were 680RD anti-rabbit (1:10,000; LI-COR Biosciences; Cat# 925-68071) and 800CW anti-mouse (1:10,000; LI-COR Biosciences; Cat# 925-32212).

Retinal immunofluorescence

Mouse eyecups were prepared by cutting the sclera behind the ora serrata and removing the cornea and lens. Eyecups were fixed for 30 min by immersion in 4% paraformaldehyde, followed by washing in PBS. The fixed tissue was cryoprotected via sequential immersion in 10, 20, and 30% sucrose, and then embedded in Tissue-Tek O.C.T. Compound (Sakura Finetek; Torrance, CA, USA; Cat# 4583) and frozen. Sections were cut at 25 µm thickness on a cryostat and mounted onto glass slides, then air dried and stored at -20° C. Thawed retina sections were blocked at room temperature for 1 hr in Antibody Incubation Solution (AIS: 3% normal horse serum, 0.5% Triton X-100, 0.025% NaN3 in PBS). The sections were then incubated in primary antibody diluted in AIS for 1 hr at room temperature. After washing with 3x with PBS, the sections were incubated for 1 hr at room temperature in secondary antibody diluted 1:1000 in AIS. The

slides were washed again 3x in PBS and coverslips applied with Lerner Aqua-Mount (Thermo Scientific; Cat# 13800).

Primary antibodies used for immunofluorescence were the same as used for immunoblotting unless indicated: rabbit anti-PKC motif phosphoserine [(R/KXpSX(R/K)] MultiMab mAb mix; 1:250), rabbit anti-PKCα (1:5000; Sigma-Aldrich; Cat# P4334), mouse anti-PKCα clone MC5 (1:5000; Sigma-Aldrich; Cat# P5704), rabbit anti-Borg4 (1:500), rabbit anti-5T4 (1:500;), rabbit anti-NHERF1 (1:100). Secondary antibodies used were anti-rabbit-AF488 (1:1000; Jackson ImmunoResearch Labs; West Grove, PA, USA; Cat# 11-545-144) and anti-mouse-Cy3 (1:1000 Jackson ImmunoResearch Labs; Cat# 115-165-003).

Scanning confocal imaging

Confocal immunofluorescence images were taken with a Leica TCS SP8 X confocal microscope (Leica; Wetzlar, Germany) using a Leica HC PL APO CS2 63x/1.40 oil immersion objective (Leica; Cat#15506350) and Leica HyD hybrid detectors, or with an Olympus Fluoview 1000 microscope (Olympus; Tokyo, Japan) using a 60x/1.42 oil immersion objective. Laser lines used were AF488 (499 nm), and Cy3 (554 nm). Detection windows used were AF488 (509-544nm) and Cy3 (564-758) nm. Brightness and contrast were adjusted using Olympus Fluoview software, Leica LAS X software, or ImageJ [111,112].

Preparation of retinas for TMT analysis

To maximize the difference between groups, retinas from wild type (n = 4) and PKCα-KO (n = 5) mice were extracted and treated for 1 hour at 37°C with 1 µM PMA diluted in bicarbonate buffered Ames medium. Following treatment, retinas were washed three times with Ames medium before being placed in chilled lysis buffer (50 mM HEPES, pH 8.5, 8 M urea, 1 mM NaF, 1 mM sodium orthovanadate, 10 mM sodium pyrophosphate, 1 mM beta-glycerophosphate), and lysed by probe sonication (Sonic Dismembrator 60; Thermo Scientific) 3 x 15 seconds at a setting of 4 with cooling on ice for 30 seconds between treatments. Protein concentrations were determined using the Pierce BCA Protein Assay Kit (Thermo Scientific; Cat# 223227) and approximately 500 µg of protein in 250 µL of lysis buffer was used for further processing. Protein disulfides were reduced with 5 µL of 1.25 M dithiothreitol at 55° C for 30 min, then alkylated by adding 22 µL of 1 M iodoacetamide and incubation at room temperature in the dark for 15 min, followed by an additional 5 µL of 1.25 M dithiothreitol. Water was added to dilute the urea concentration to 2 M. Sequence grade modified trypsin (Promega; Madison, WI, USA; Cat# V5111) was added at a 25:1 protein:trypsin ratio and samples were incubated overnight at 37° C before being acidified

with trifluoroacetic acid (TFA) to a final concentration of 1%. Remaining particulates were removed by centrifugation at 16,000 x g for 10 min.

Peptides were purified by solid phase extraction using 1 cc (50 mg) Waters Sep-Pak Vac tC18 cartridges (Waters Corporation; Milford, MA, USA; Cat# WAT054960). Briefly, the cartridges were conditioned twice with 1 mL acetonitrile (ACN) and twice with 300 µL of 50% ACN/0.5% acetic acid, then equilibrated twice with 1 mL 0.1% TFA. The samples were loaded and passed through the bed, then were washed twice with 1 mL 0.1% TFA followed by 200 µL of 0.5% acetic acid. Finally, the samples were eluted twice with 500 µL of 50% ACN/0.5% acetic acid. Peptide concentrations were determined using the Pierce Quantitative Colorimetric Peptide Assay (Thermo Scientific; Cat# 23275). Approximately 300 µg of peptide was recovered from each digest. Fifteen µg of each sample was reserved for TMT analysis of total protein abundance, and the remainder was used for the phosphopeptide enrichment experiment.

Phosphopeptide enrichment

Phosphopeptides were enriched following previously described methods [113,114] with small modifications. Titanosphere TiO2 5 µm beads (GL Biosciences; Tokyo, Japan; Cat# 5020-75000) were washed three times in 2 M lactic acid/50% ACN, then resuspended in the same solution at 24 mg/mL. Approximately 285 µg of dried peptide for each sample was resuspended in 950 µL of 2 M lactic acid/50% ACN and 100 µL (2.4 mg) of the bead suspension was added to each sample, ensuring an 8:1 ratio of beads:peptide. The bead:peptide mixture was rotated at room temperature for 1 hour, then washed twice with 500 µL 2M lactic acid/50% ACN, 0.1% TFA/50% ACN, then 0.1% TFA/25% ACN. The enriched phosphopeptides were eluted from the beads by vortexing in 100 µL of 50 mM K2HPO4 at pH 10 for 5 min. The elution step was repeated once and the 200 µL of eluate was dried by vacuum centrifugation.

The enriched phosphopeptides were then purified by solid phase extraction using UltraMicro Spin columns (The Nest Group Inc.; Southborough, MA, USA). The dried phosphopeptides were resuspended in 60 µL 1% TFA and the pH was tested to ensure the samples were acidic. The columns were conditioned three times with 100 µL 80% ACN/0.1% TFA and equilibrated three times with 50 µL of 0.1% TFA. The samples were loaded and passed through the columns three times, washed three times with 25 µL of 0.1% TFA, eluted three times with 50 µL 80% ACN/0.1% formic acid, and dried by vacuum centrifugation before TMT labeling.

TMT labeling and mass spectrometric analysis

In preparation for TMT labeling, nine dried unfractionated peptide samples (4 WT and 5 KO) and nine phosphopeptide enriched samples (4 WT and 5 KO) were dissolved in 25 µL of 100 mM triethylammonium bicarbonate buffer, and TMT 10-plex reagents (Thermo Scientific; Cat# 90110) were dissolved at a concentration of 15 µg/µL in anhydrous ACN. Each of the samples was then labeled by adding 12 µL (180 µg) of an individual TMT reagent, followed by shaking at room temperature for 1 hr. Two µL of each of the nine labeled samples in each group were pooled, and 2 µL of 5% hydroxylamine was added. The samples were incubated for 15 min, dried by vacuum centrifugation, dissolved in 21 µL of 5% formic acid, and peptides were analyzed by a single 2-hour LC-MS/MS method using an Orbitrap Fusion as described below. The run was performed to normalize the total reporter ion intensity of each multiplexed sample and to check labeling efficiency. After the normalization and efficiency run, the remaining unmixed samples were then quenched by the addition of 2 µL 5% hydroxylamine, then combined in adjusted volumes to yield equal summed reporter ion intensities during the subsequent two-dimensional LC/MS.

Following volume-based normalization, the combined samples were dried by vacuum centrifugation, and TMT-labeled samples were reconstituted in 20 µL water. The reconstituted peptides were separated by two-dimensional nano reverse-phase liquid chromatography (Dionex NCS-3500 UltiMate RSLCnano UPLC) EasySpray NanoSource (Thermo Scientific), ionized using an EasySpray NanoSource (Thermo Scientific), and SPS MS3 data acquired with an Orbitrap Fusion Tribrid mass spectrometer (Thermo Scientific). The liquid chromatography details and mass spectrometer settings were as previously described [110] with the modification that non-enriched peptides were eluted from the first dimension high pH column using sequential injections of 20 µL volumes of 14, 17, 20, 21, 22, 23, 24, 25, 26, 27, 28, 29, 30, 35, 40, 50, and 90% ACN in 10 mM ammonium formate, pH 9, and enriched phosphopeptides were eluted by sequential 20 µL injections of 4, 6, 8, 10, 12, 18, 20, 22, 25, 30, and 60% ACN in 10 mM ammonium formate, pH 9.

TMT data analysis

The binary instrument files were processed with Proteome Discoverer version 1.4 (Thermo Scientific) to extract fragment ion spectra, precursor information (m/z values and peptide charge state), and TMT reporter ion peak intensities. The fragment ion spectra were searched against a canonical Uniprot Swiss-Prot mouse protein database (downloaded 07/07/2016 from

https://www.uniprot.org) with 16,794 entries. There were 179 common contaminant entries appended for a total of 16,973 sequences.

The SEQUEST [115] search engine was used with a parent ion mass tolerance of 1.25 Da and fragment ion tolerance of 1.0005 Da. Trypsin cleavage with up to two missed cleavages was specified. A static modification of +57.0215 Da was applied to all cysteine residues and a variable modification of +15.9949 was applied to methionine. Confident peptide-to-spectrum matches (PSMs) were obtained using the percolator [116] node, and only peptides with q values < 0.05 were accepted. Parsimonious protein inference was used in Proteome Discoverer to produce final protein lists, and the results were exported to tab-delimited files for post processing using in-house Python scripts (https://www.github.com/pwilmart/PAW_pipeline.git). For the protein expression analysis of the total protein preparations, the reporter ion intensities from all unique (matching to just one protein) peptides were summed into protein reporter ion intensities. Any contaminant proteins were excluded from further analysis. Reporter ion data from PSMs where the trimmed average reporter ion intensity did not exceed 500 were excluded. Any final protein reporter ion sums of zero were replaced with a value of 150 (the smallest non-zero reporter ion intensities observed were approximately 350) to avoid mathematical errors during visualizations and statistical testing.

The data from the phosphopeptide enrichment experiment was searched with additional variable modifications of +79.9799 on serine, threonine, or tyrosine residues, and only peptides with q < 0.01 were accepted. The phosphorylation site localization node phosphoRS [117] was configured after the search node in Proteome Discoverer. Phosphorylation enrichment experiments are peptide centric, so data aggregation was done differently than for protein expression. Peptide sequences were aggregated by summing reporter ion intensities within each channel to reduce variance and increase statistical power. All PSMs assigned to the same base peptide sequence were aggregated in the same modification state, which was determined by integral peptide MH+ mass (the peptide in a 1+ charge state). Localization information from phosphoRS was simplified to the same number of top probabilities as the number of phosphorylation modifications present in the peptides. The reporter ion intensities from the combined reports were used for differential expression (DE) testing as described below. Any contaminant protein matches were excluded from further analysis. Minimum intensity filtering and zero replacement was done similarly to the total protein analysis.

For immunofluorescence quantification, data are represented in text as the mean ± SEM and p-values were calculated using an unpaired t-test.

For TMT data, the table of non-contaminant reporter ion intensities for proteins or for aggregated phosphopeptides were exported to tab-delimited files and imported into R (https://www.r-project.org) for statistical analysis using the edgeR [118,119] Bioconductor package. Normalization was done using a "library size" factor and the trimmed mean of M-values normalization [120] function in edgeR was used to correct for sample loading and compositional bias. DE testing was performed pairwise using the exact test with Benjamini-Hochberg multiple testing corrections [121]. The results from edgeR analyses were exported and added to the combined data summaries. Annotation information was added from Uniprot using a script available at https://github.com/pwilmart/annotations.

Data availability

The mass spectrometry proteomics data have been deposited to the ProteomeXchange Consortium via the PRIDE partner repository [122], with the dataset identifier PXD012906.

Results

RBC dendrites are major sites of light-dependent PKCα phosphorylation

To visualize sites of PKCα phosphorylation in the retina, we used a monoclonal antibody mix that binds to canonical PKC substrate motifs containing a phosphorylated serine (PKC motif p-serine). Anti-PKC motif phosphoserine immunofluorescence between wild type and PKCα-KO retina sections indicates that RBC dendrites are the main sites of PKCα phosphorylation in the mouse retina (**Figure 2.1A and B**). The small immunofluorescent puncta in the outer plexiform layer (OPL) are presumptive RBC dendrites, whereas the larger patches of phosphoserine immunofluorescence (arrows) are associated with cone pedicles. The small immunofluorescent puncta are visible throughout the wild type OPL but are greatly reduced in intensity in the PKCα-KO retina, while immunofluorescence corresponding to cone pedicles is unchanged. These results suggest that PKCα phosphorylates targets in RBC dendrites of wild type adult mice, and that a different PKC isoform phosphorylates targets associated with cone pedicles.

To examine whether PKCα activity is light-dependent, we used a conformation-dependent monoclonal PKCα antibody which binds an epitope in the hinge region of PKCα that is inaccessible in the inactive state [123]. Retina sections from light-adapted and dark-adapted mice were double-labeled with the conformation-specific antibody (anti-PKCα-A) and a non-

conformation-specific PKCα antibody (anti-PKCα-B; **Figure 2.2**). Both antibodies strongly label RBC cell bodies and dendrites in sections from light-adapted retina, with co-localization of the two secondary antibodies appearing white (**Figure 2.2A**, left). By contrast, only anti-PKCα-B labels RBCs in sections from dark adapted retina (**Figure 2.2A**, right). These results suggest that PKCα is active in RBC dendrites in the light-adapted state. This was supported by labeling of light- and dark-adapted retina sections for phosphorylated PKC motifs. The anti-PKC motif phosphoserine antibody labeled puncta in the OPL of light-adapted retina (**Figure 2.2B**, left), similar to the wild type immunofluorescence seen in **Figure 2.1**. Anti-PKC motif phosphoserine immunofluorescence was absent in the OPL of the dark-adapted retina (**Figure 2.2B**, right). Together, the results from **Figures 2.1** and **2.2** indicate that PKCα is active in RBC dendrites in the light-adapted state.
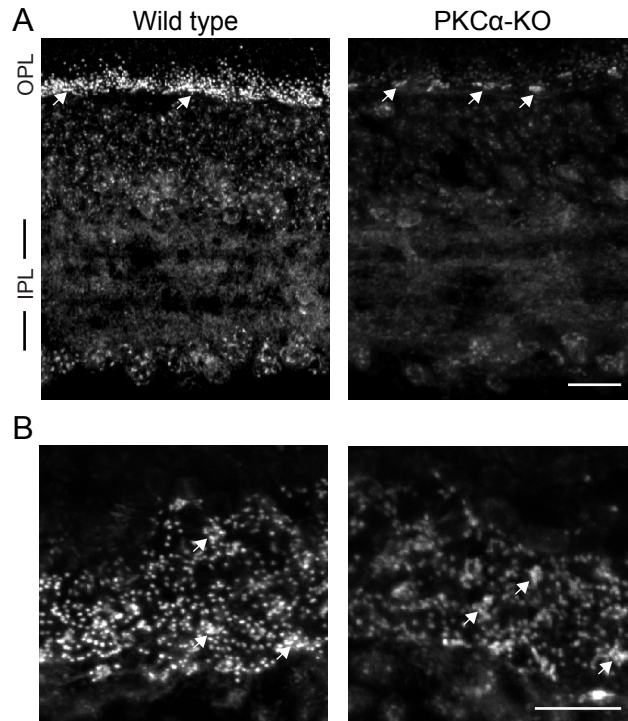
Figure 2.1: Phosphoserine labeling in the OPL is reduced in PKCα-KO retina. **(A)** Immunofluorescence confocal images of mouse retina sections from wild type and PKCα-KO retinas labeled with an antibody against phosphoserine residues within canonical PKC motif phosphoserine (PKC motif p-serine). **(B)** Images of PKC motif p-serine immunofluorescence in the outer plexiform layer of wild type and PKCα knockout (KO) retinas in obliquely cut sections. In both **A** and **B**, white arrows indicate labeling associated with presumptive cone pedicles. Scale bars: 20 μm. OPL: outer plexiform layer; IPL: inner plexiform layer.
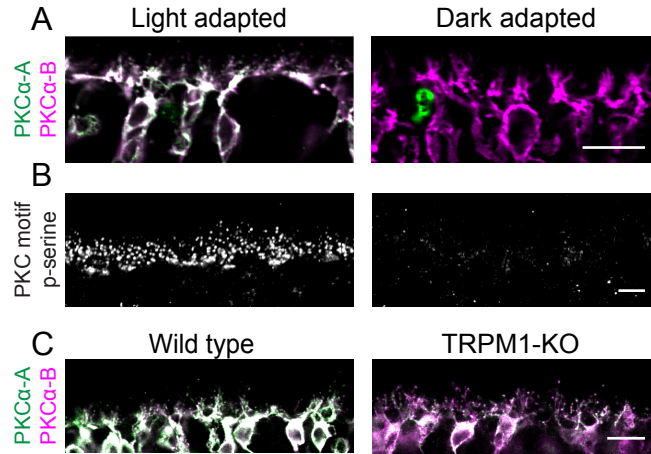
Figure 2.2: PKCα is active in light-adapted RBCs. **(A)** Light- and dark-adapted mouse retina sections double-labeled with two antibodies against PKCα; conformation-specific PKCα-A (green) binds only active PKCα, while PKCα-B (magenta) binds to both active and inactive PKCα. **(B)** Sections from light-adapted and dark-adapted mouse retina labeled with an antibody mixture against PKC motif phosphoserines (PKC motif p-serine). **(C)** WT and TRPM1-KO mouse retina sections double-labeled with conformation-specific PKCα-A (green) and conformation non-specific PKCα-B (magenta). Scale bars: 10 μm. OPL: outer plexiform layer.

Conventional PKC isoforms, including PKCα, require calcium for activation [124]. In RBC dendrites, a likely source of calcium is the Transient Receptor Potential cation channel subfamily M 1 (TRPM1) cation channel, which mediates an influx of sodium and calcium to generate the RBC light response [43,45,125]. The dependence of PKCα activation on TRPM1 was assessed by double-labeling retina sections from wild type and TRPM1 knockout (TRPM1-KO) mice with anti-PKCα-A and anti-PKCα-B to detect active and total PKCα, respectively, in RBC cell bodies and dendrites (**Figure 2.2C**), and the intensities of the immunofluorescence obtained with the two antibodies was compared. The average ratio of anti-PKCα-A (active) to anti-PKCα-B (total) immunofluorescence in wild type RBCs was 1.12 ± 0.12 (n = 4 mice, each with 4 technical replicates) compared to 0.70 ± 0.15 (n = 3 mice, each with 4 technical replicates) in TRPM1-KO RBCs ($p < 0.0001$), indicating that PKCα is less active in RBCs in the absence of TRPM1.

PKCα is a DAG-sensitive PKC isoform, and therefore PKCα phosphorylation can be potentiated by the DAG analogue phorbol 12-myristate 13-acetate (PMA). To confirm that PKCα is phosphorylating proteins in the retina *ex vivo*, we incubated freshly dissected wild type and PKCα-KO retinas in PMA before analyzing changes in protein phosphorylation by immunoblotting for PKC motif phosphoserines (PKC motif p-serine). PMA activation of other DAG-sensitive PKC isoforms expressed in the retina, such as PKCβ, should be relatively equivalent between WT and PKCα-KO samples and result in no difference in phosphorylation. PMA treatment resulted in a significant increase in intensity of several phosphoserine immunoreactive bands in the wild type samples at the 15, 30, and 60 min time-points compared to the PKCα-KO samples (**Figure 2.3A**)

demonstrating that PMA treatment increases differential phosphorylation between WT and PKCα-KO retinas. To identify sites of PMA-activated PKC phosphorylation in the wild type retina, PKC motif phosphoserine immunofluorescent labeling was performed on retina sections made from PMA-treated, light-adapted WT retinas. PMA incubation resulted in an increase in PKC motif phosphoserine immunofluorescence in presumptive RBC dendritic tips (**Figure 2.3B**).
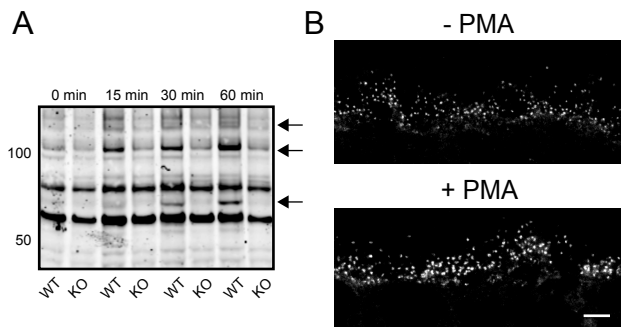
Figure 2.3: PMA increases phosphorylation by PKC isoforms in the mouse retina. (**A**) Wild type (WT) and PKCα knockout (PKCα-KO) retinas were incubated in PMA for 0, 15, 30, and 60 min followed by western blotting with an antibody against PKC motif phosphoserines. Arrows indicate candidate PKCα phosphorylation targets. **(B)** Immunofluorescent PKC motif phosphoserine labeling of wild type mouse OPL from retinas that were incubated with and without PMA for 1 hr. Scale bar: 10 μm. PMA: phorbol 12-myristate 13-acetate; OPL: outer plexiform layer.

Differential protein abundance in wild type and PKCα-KO retina

To identify retinal proteins whose expression is dependent on PKCα, four wild type and five PKCα-KO retinas were incubated with PMA for an hour immediately after dissection and then processed for multiplexed TMT mass spectrometry (Figure 2.4). Retinas were lysed and proteins digested with trypsin before TMT labeling and LCMS/MS. Peptide identification was performed with Proteome Discoverer using SEQUEST and Percolator. From 38,384 confidently identified PSMs, there were 34,969 unique peptides corresponding to 4,435 proteins (excluding contaminants; Figure 5, S1 – Total Protein and Phosphopeptide Abundance Analysis). Differential expression (DE) statistical testing was done with edgeR using the trimmed mean of M-values normalization and an exact pairwise test. After Benjamini-Hochberg p-value corrections for multiple comparisons to establish DE false discovery rates (FDRs), we grouped proteins with significant differential expression into significance groups based on FDR thresholds: not significant (FDR > 0.10 [4412 proteins]) low significance (0.10 > FDR > 0.05 [2 proteins]), medium significance (0.05 > FDR > 0.01 [5 proteins]), and high significance (FDR < 0.01 [16 proteins]).
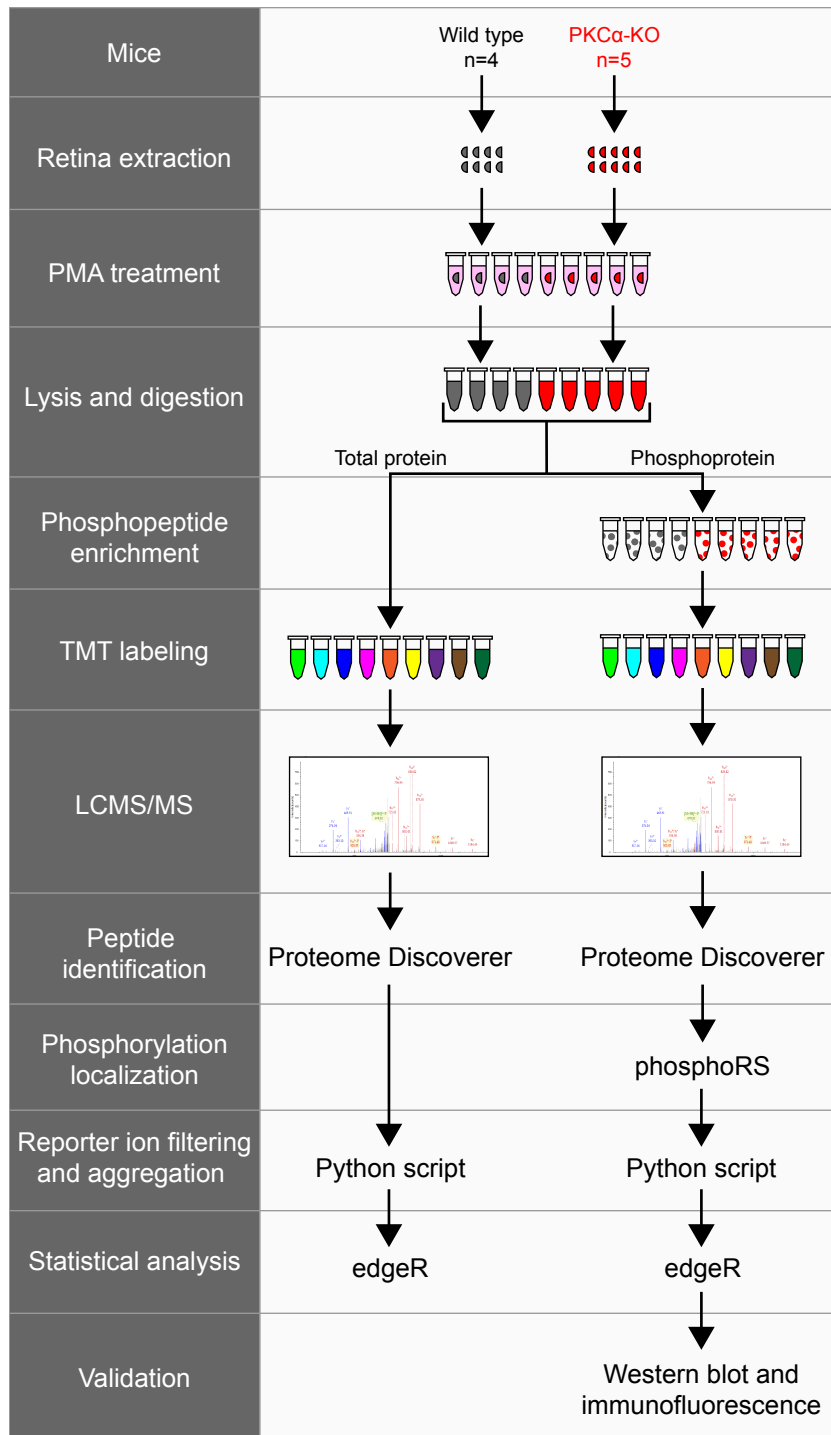
Figure 2.4: Experimental workflow of total protein and phosphopeptide identification. Wild type (n = 4) and PKCα knockout (KO) (n = 5) retinas were extracted and treated with PMA before lysis and trypsin digestion. A small fraction of each sample was removed for total protein analysis, while the rest of the samples underwent phosphopeptide enrichment. Following TMT labeling, samples were combined and analyzed by LCMS/MS. Tandem mass spectrometry data was collected on an Orbitrap Fusion and proteins were identified using Proteome Discoverer (SEQUEST and Percolator). Phosphorylation site localization was scored using phosphoRS, and reporter ion intensities were filtered and aggregated with an in-house Python script. TMT reporter ion intensities from total proteins or from phosphopeptides were tested for differential expression using the Bioconductor package edgeR. The presence of representative phosphoproteins was validated in the retina by western blot and confocal immunofluorescence microscopy. PMA: phorbol 12-myristate 13-acetate.

27

Plotting the mean reporter ion intensities between wild type and PKCα-KO samples (**Figure 2.5A**) revealed a small number of significantly different protein abundances in both WT (15 proteins) and KO (8 proteins). The proteins with the largest changes in abundance were KPCA (PKCα; 14-fold decrease in KO), and MTUS1 (Microtubule Associated Scaffold Protein 1; 24-fold increase in KO). A volcano plot comparing $\log_2$ fold change (WT / KO) with $-\log_{10}$ FDR (**Figure 2.5B**) depicts the 23 proteins passing the FDR < 0.1 cutoff for low significance. We did not attempt any isotopic corrections for reporter ions, so the degree of downregulation for PKCα is consistent with an absence of the kinase in the knockout. A list of all significant differentially expressed proteins can be seen in **Figure 2.5C**. The sample-to-sample reproducibility of the protein abundance experiment was excellent: the WT samples had a median coefficient of variance (CV) of 11.4%, the KO samples had a median CV of 15.5%, and the independent CV was 13.5%. Ninety-five percent of the expression changes were less than 1.25-fold different (S2.2 – Total Protein and Phosphopeptide Statistical Testing).

C Total protein abundance

	Gene (protein)	Fold change	FDR
Wild type > PKCα-KO	Prkca (PKCα)	14.34	3.98E-142
	Lyrm7	4.95	1.41E-02
	Mfap2	3.53	8.20E-02
	Dnajc18	2.96	5.13E-02
	Nfs1	2.17	1.27E-02
	Calb1	2.11	3.41E-02
	Fn3k	1.88	4.00E-04
	Hist1h3b	1.75	3.21E-05
	Atp1a2	1.63	1.27E-06
	Zfp41	1.58	7.38E-04
	Selenoh	1.50	2.07E-03
	Dnmt3a	1.45	2.18E-04
	Hmgp3	1.41	1.15E-02
	Dsah2	1.39	2.68E-02
	Pdlim3	1.35	6.81E-02
PKCα-KO > Wild type	Mtus1	24.16	8.28E-27
	Polr3k	6.41	1.03E-06
	Plxnb1	5.33	2.18E-04
	Rab3gap2	4.16	4.83E-03
	Bub1b	3.18	1.19E-02
	Scg5	2.04	6.66E-13
	Lrrc57	1.45	3.57E-03
	Aqp4	1.39	4.83E03

● Not Significant ● Low Significance ● Med Significance ● High Significance

***Figure 2.5: Identification of differentially expressed total proteins**. **(A)** Scatter plot of peak reporter ion intensities from wild type (WT) and PKCα knockout (KO) total protein abundance samples. The dotted line corresponds to an FC (WT / KO) of 1, with FC > 1 corresponding to increased abundance in WT vs KO, and FC < 1 corresponding to increased abundance in KO vs WT. **(B)** Volcano plot of $\log_2$ FC and $-\log_{10}$ FDR. The dotted lines correspond to FC = 1 and FDR = 0.1. FDR < 0.1 corresponds to proteins passing the low significance threshold, and FDR > 0.1 corresponds to proteins failing the low significance threshold. The low significance (orange) threshold was 0.1, the med significance threshold (green) was 0.05, and the high significance threshold (blue) was 0.01. **(C)** Table of all differentially abundant proteins with an FDR lower than the low significance threshold of 0.1. Fold change was calculated by dividing the mean reporter*

ion intensities of each protein from the genotype with higher abundance by that with lower abundance. Colors correspond to DE FDR thresholds. DE: differential expression; FC: fold change; FDR: false discovery rate.

Differential protein phosphorylation between wild type and PKCα-KO retina

To examine differences in protein phosphorylation between wild type and PKCα-KO retinas, phosphopeptides were enriched from the same retinal extracts used above (described in the Methods), and phosphopeptide abundance was analyzed by multiplexed TMT mass spectrometry. Peptide identification was performed with Proteome Discoverer using SEQUEST and Percolator, and phosphorylation localization was performed using phosphoRS. Results files were exported for post processing (filtering and aggregation) using an in-house Python script (PD1.4 TMT phospho processer.py available at https://github.com/pwilmart/PAW pipeline). The aggregated phosphopeptide reporter ion data was tested for differential expression using edgeR with multiple testing corrections, and phosphopeptides were grouped into significance groups based on differential expression FDR as described for total proteins.

We identified 1137 distinct phosphopeptides in wild type or PKCα-KO retina lysates (**Figure 2.6, S1 – Total Protein and Phosphopeptide Abundance Analysis**) 1113 were not significant (FDR > 0.10), seven showed low significance (0.10 > FDR > 0.05), four medium significance (0.05 > FDR > 0.01), and thirteen were highly significant (FDR < 0.01). Of the 24 significant phosphoproteins, only two showed differential expression in the total protein abundance analysis: Dnmt3a (DNA (Cytosine-5)-Methyltransferase 3A), which was significantly more abundant in the WT samples (1.5fold), and Scg5 (Neuroendrocrine Protein 7B2), which was significantly more abundant in the KO samples (2.04-fold). Plotting WT and KO peak ion intensities (**Figure 6A**) highlights five phosphopeptides with much greater expression in WT than KO. A volcano plot comparing $\log_2$ FC (WT / KO) with $-\log_{10}$ FDR (**Figure 2.6B**) shows the 24 phosphopeptides passing the FDR < 0.1 threshold (14 increased in WT and 10 increased in KO). A full list of all significant differentially expressed phosphopeptides, along with their total protein abundance changes, can be seen in **Figure 2.6C**. The reproducibility of the peptide-centric experiment was strong: the WT samples had a median CV of 13.9%, the KO samples had a median CV of 18.7%, and the median CV independent of condition was 16.2%. Ninety-five percent of the expression changes were less than 1.4-fold different (*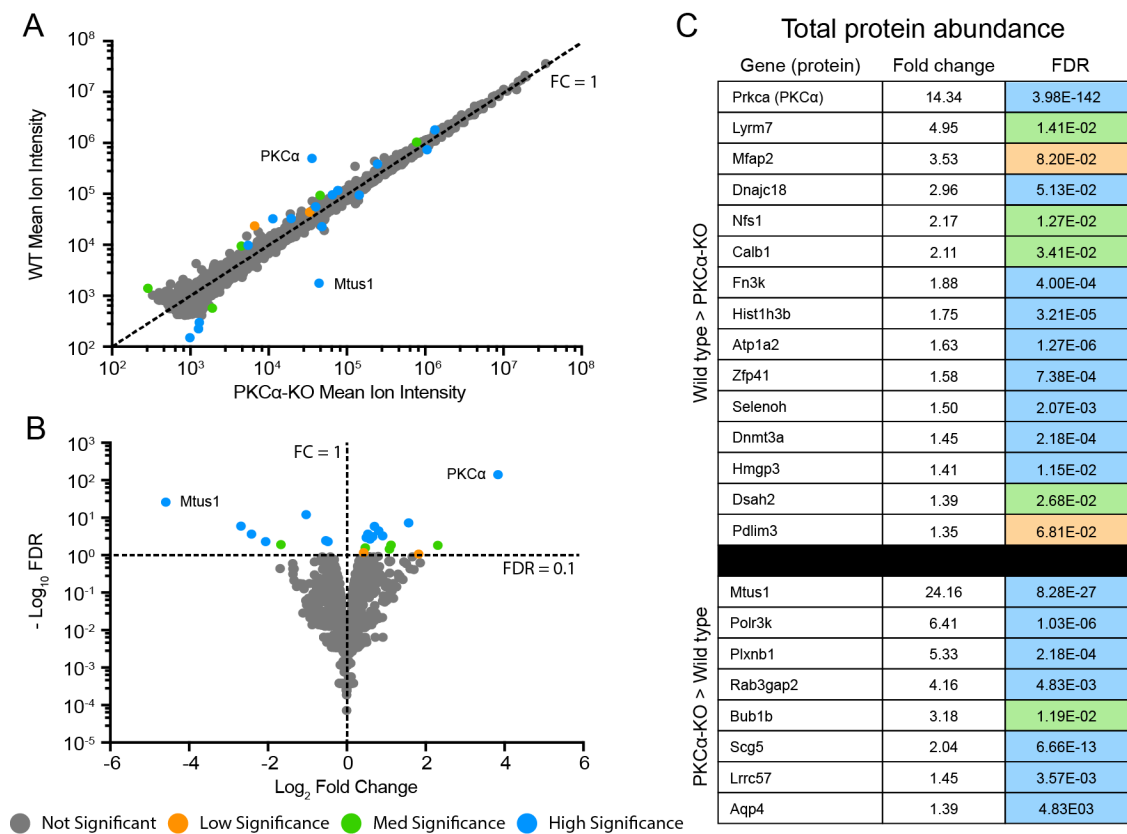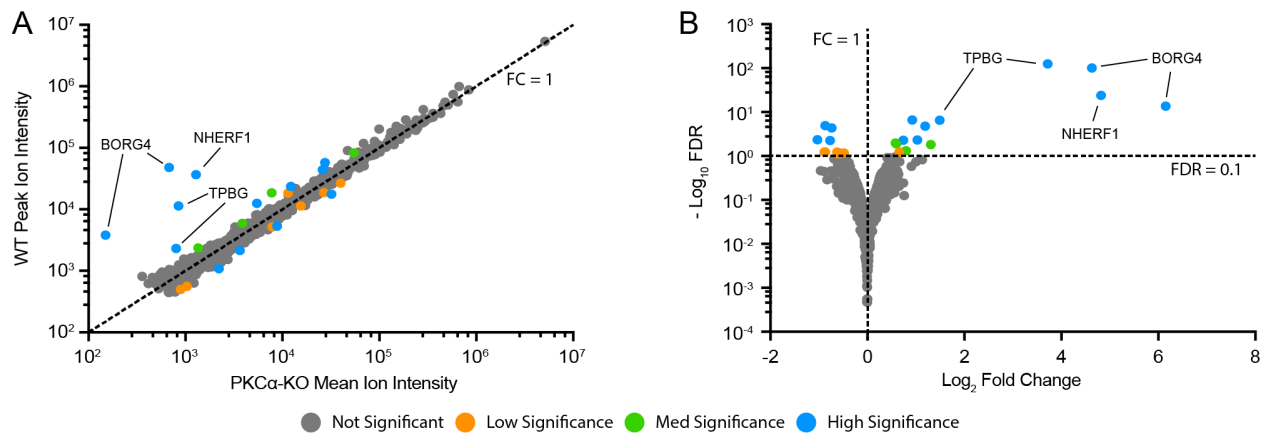*S2.2 – Total Protein and Phosphopeptide Statistical Testing**). Annotated fragment ion spectra for the phosphorylated peptides are shown in **S2.3 – Annotated Phosphopeptide Spectra**.

Phosphoprotein abundance

	Phosphopeptide sequence	Gene (protein)	Phosphopeptide		Total protein	
			Fold change	FDR	Fold change	FDR
Wild type > PKCα-KO	EADDESLDEQASASKLSLLSR	Cdc42ep4 (BORG4)	71.12	2.98E-14	1.00	9.99E-01
	EALVEPASESPRPALAR	Slc9a3r1 (NHERF1)	28.29	1.57E-24	1.02	9.93E-01
	AREADDESLDEQASASKLSLLSR	Cdc42ep4 (BORG4)	24.68	3.48E-103	1.00	9.99E-01
	LTNLSSNSDV	Tpbg	13.20	1.30E-127	1.09	9.89E-01
	LTNLSSNSDV	Tpbg	2.82	3.06E-07	1.09	9.90E-01
	SATRVIGGPVTPR	Pde6g	2.48	1.64E-02	-1.11	9.69E-01
	SLRRQQQPCMEPPESQLEPK	Znf512	2.29	1.63E-05	-1.03	9.92E-01
	RSSVRPGVVVPR	Ankrd33b	2.05	4.84E-03	1.08	9.52E-01
	RLSTHSPFR	Epb41	1.90	2.39E-07	1.02	9.98E-01
	SLAALDALNTDDENDEEEYEAWKVR	Dnmt3a	1.73	4.65E-02	-1.45	2.18E-04
	RVSNRGLAGTTIR	Amer2	1.68	5.18E-03	-1.08	9.63E-01
	DGRGAAQNIIPASTGAAK	Gapdh	1.58	5.91E-02	1.06	9.67E-01
	SEPQPEEGSPAAQK	Epb41l2	1.51	1.17E-02	1.04	9.89E-01
	QRSYNLVVAK	Mfap1	1.49	9.81E-03	-1.11	8.82E-01
PKCα-KO > Wild type	EGDGSATTDAAPATSPKAEEPSKAGDAPSEEK	Gap43	2.04	4.52E-03	1.13	8.85E-01
	SPPPSPTTQR	Dnm3	1.85	5.80E-02	1.03	9.92E-01
	ARPSQLPEQSSSAQQNGSVSDISPVQAAK	Kif2a	1.83	5.78E-02	-1.00	9.98E-01
	SSASVSLPPGTPEK	Crocc	1.83	1.16E-05	1.13	6.64E-01
	ARVDHGAEIITQSPSRSSVASPR	Map2	1.71	5.39E-03	1.05	9.89E-01
	SVPHFSEEEKEAE	Scg5	1.67	4.37E-05	2.04	6.66E-13
	SFSLGDLSHSPQTAQHVER	Ccdc177	1.54	5.78E-02	1.24	3.53E-01
	SLTNSHLEKR	Slc39a1	1.53	7.55E-02	NA	NA
	GPLPAAPPTAPERQPSWER	Rtn4	1.47	7.02E-02	1.06	9.78E-01
	SADRRLSGAQAELALQEESVR	Crocc	1.40	6.77E-02	1.13	6.64E-01

Figure 2.6: Identification of differentially expressed phosphopeptides. (**A**) Scatter plot of peak reporter ion intensities from wild type (WT) and PKCα knockout (KO) phosphopeptide abundance samples. The dotted line corresponds to an FC (WT / KO) of 1, with FC > 1 corresponding to increased abundance in WT vs KO, and FC < 1 corresponding to increased abundance in KO vs WT. (**B**) Volcano plot of $\log_2$ FC and $-\log_{10}$ FDR. The dotted lines correspond to FC = 1 and FDR = 0.1. FDR < 0.1 corresponds to proteins passing the low significance threshold, and FDR > 0.1 corresponds to proteins failing the low significance threshold. The low significance (orange) threshold was 0.1, the med significance threshold (green) was 0.05, and the high significance threshold (blue) was 0.01. (**C**) Table of all differentially abundance phosphopeptides with an FDR lower than the low significance threshold of 0.1. In the phosphopeptide sequence column, phosphorylated residues are in red. In the Total Protein Fold Change column, negative values indicate an increased abundance in the KO samples. Fold change was calculated by dividing the mean reporter ion intensities of each protein from the genotype with higher abundance by that with lower abundance. Fold change and DE FDR values were taken from the phosphopeptide abundance experiment and the total protein abundance experiment. Colors correspond to DE FDR thresholds. DE: differential expression; FC: fold change; FDR: false discovery rate.
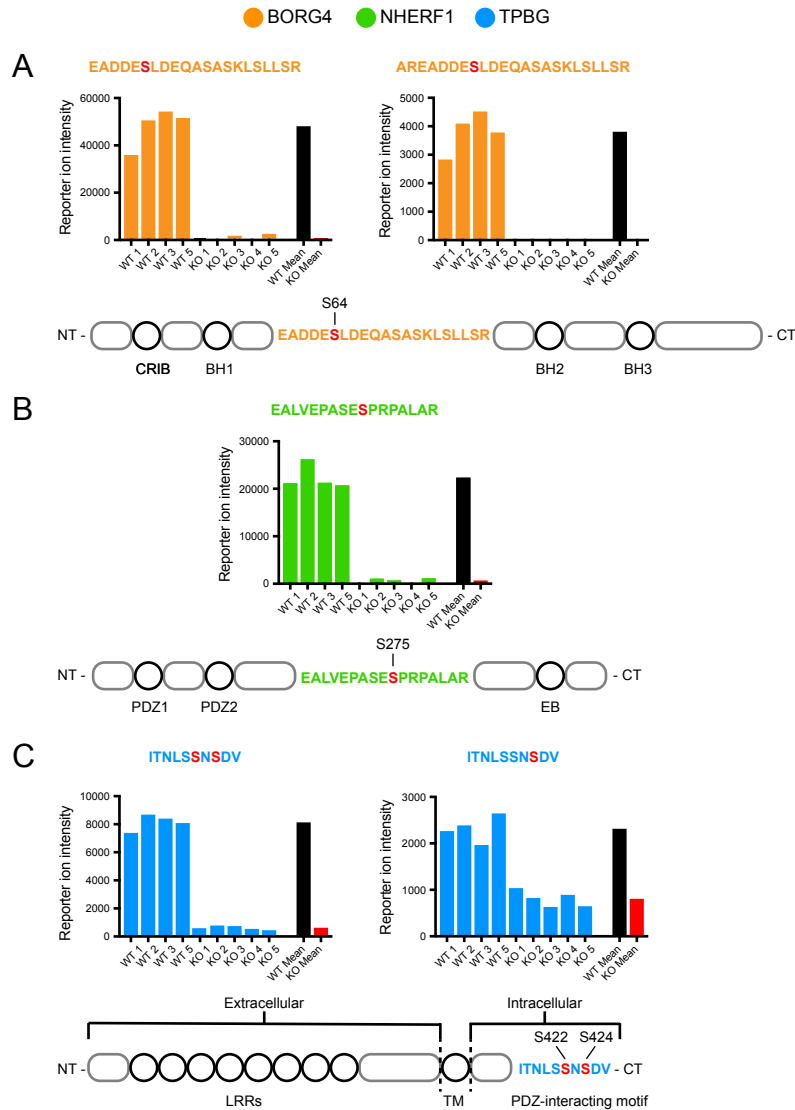
Figure 2.7: TMT data from representative phosphoproteins. Reporter ion intensity values from each TMT channel for the five phosphopeptide fragments with the largest differential expression between WT (n = 4) and PKCα-KO (n = 5): two from BORG4 (orange), one from NHERF1 (green), and two from TPBG (blue). For statistical significance of differential expression analysis of mean WT (**black**) and mean KO (**red**) reporter ion intensities, see S1 – Total Protein and Phosphopeptide Abundance Analysis. **(A)** Two phosphopeptide fragments from an overlapping region of BORG4, each containing a phosphorylated serine corresponding to S64 on the full-length protein. **(B)** One phosphopeptide fragment from NHERF1 with a phosphorylated serine corresponding to S275 on the full-length protein. **(C)** Two phosphopeptide fragments from the C-terminal tail of TPBG with two similar phosphorylation patterns: one with two phosphoserines corresponding to S422 and S424, and one with a single phosphoserine corresponding to S424 of the full-length protein.

Five phosphopeptides belonging to three proteins showed the largest and most significant differential abundance between the wild type and PKCα-KO samples (**Figure 2.7**). Two similar phosphopeptides were identified corresponding to BORG4 (Binder of Rho-GTPase, also called CDC42EP4) with phosphoserine residues observed at the peptide sites S6 (71-fold increase) and S8 (25-fold increase). Both peptides were generated by slightly different cleavage patterns of the

same amino acid sequence with the same phosphorylated serine residue corresponding to site S64 in full-length BORG4 (**Figure 2.7A**). One phosphopeptide fragment was identified from NHERF1 (Na⁺/H⁺ Exchanger Regulatory Factor 1, also called SLC9A3R1 and EBP50) with a phosphorylated serine residue at the peptide S10 position (28-fold increase) corresponding to S275 in the full-length protein (**Figures 2.7B**). The last two major significant phosphopeptides correspond to the same 10 amino acid sequence of TPBG (Trophoblast Glycoprotein, also called the 5T4 antigen and WAIF1) with two identified species: a doubly-phosphorylated peptide with phosphoserines at peptide S6 and S8 (13-fold increase), and a singly-phosphorylated peptide with just phosphorylated peptide S8 (2.8-fold increase). These two serine residues correspond to S422 and S424 in the C-terminal intracellular tail of TPBG (**Figure 2.7C**).

Grouping of significant protein and phosphoprotein results by biological function

Proteins identified in the total protein abundance (**Figure 2.8A**) and phosphoprotein abundance (**Figure 2.8B**) experiments were grouped into broad categories based on general biological function annotations added from Uniprot (https://github.com/pwilmart/annotations.git). PKCα-KO resulted in differential expression of proteins and phosphoproteins involved in many aspects of cellular physiology, particularly cytoskeletal rearrangement and vesicle trafficking (15 proteins), transcriptional regulation (8 proteins), and homeostasis and metabolism (5 proteins).

A   Significant Total Proteins

	Cytoskeleton/Trafficking	ECM/Adhesion	Cell Signaling	Transcriptional Regulation	Homeostasis/ Metabolism	Chaperone	Transporter
WT > KO	Mfap2 Pdlim3		Prkca Calb1	Dnajc17 Zfp41 Dnmt3a Hmgb3	Nfs1 Fn3k Selenoh Dsah2	Lyrm7 Hist1h3b	Atp1a2
KO > WT	Mtus1 Plxnb1 Bub1b	Lrrc57	Rab3gap2	Polr3k		Scg5	Aqp4

B   Significant Phosphoproteins

	Cytoskeleton/Trafficking	ECM/Adhesion	Cell Signaling	Transcriptional Regulation	Homeostasis/ Metabolism	Chaperone	Transporter
WT > KO	Borg4 Nherf1 Epb41 Epb41l2	Tpbg Mfap1a	Pde6g Amer2	Znf512 Ankrd33b Dnmt3a	Gapdh		
KO > WT	Gap43 Dnm3 Kif2a Crocc Map2 Rtn4			Ccdc177		Scg5	Slc39a1

Figure 2.8: Significant total proteins and phosphoproteins grouped by biological function*. Table of genes of identified total proteins (**A**) and phosphoproteins (**B**) with significant differential abundance between wild type and PKCα-KO samples grouped into broad categories based on general biological function gathered from Uniprot protein annotations.*

Localization of the major PKCα-dependent phosphoproteins in the mouse retina

We used immunoblotting and immunofluorescence confocal microscopy to examine the presence of the three most prominent PKCα-dependent phosphoprotein hits in the wild type retina: BORG4, NHERF1, and TPBG. Immunoblotting for BORG4 shows a distinct band at 38 kDa (**Figure 2.9A**) in agreement with the predicted molecular weight of BORG4. Immunofluorescence double-labeling of retina sections for BORG4 and PKCα shows punctate BORG4 labeling in the outer plexiform layer (OPL), but the BORG4 puncta are not strongly co-localized with PKCα **(Figure 2.9B)**. This is consistent with labeling of either RBC or horizontal cell dendritic tips, as they are closely apposed to one another within the rod spherule invagination [126,127]. BORG4 immunofluorescence was also detected in nuclei in the inner nuclear layer (INL) and ganglion cell layer.

Immunoblotting of retinal proteins for NHERF1 detected a strong band at ~50 kDa, the predicted molecular weight of NHERF1 (**Figure 2.9C**). Immunofluorescent labeling of retina sections revealed NHERF1 immunoreactivity at the level of the photoreceptor inner segments and in the retinal pigment epithelium (RPE; **Figure 2.9D**). It was not possible to determine whether NERF1 at the level of the inner segments is due to its presence in the photoreceptors themselves or the apical microvilli of the RPE, which surround the photoreceptor outer and inner segments. No NHERF1 immunofluorescence was seen in the synaptic layers of the retina.

Immunoblotting of retina lysate for TPBG labels a broad band centered around 72 kDa (**Figure 2.9E**). This is higher than the predicted molecular weight of 42 kDa, but is consistent with extensive glycosylation of TPBG [128]. Immunofluorescent localization of TPBG revealed strong immunoreactivity in the OPL as well as in large synaptic terminals at sublamina 5 of the inner plexiform layer (IPL**; Figure 2.9F**). In the OPL, TPBG labeling co-localizes with PKCα in RBC dendrites and cell bodies. In the IPL, TPBG immunoreactivity overlaps with all PKCα-positive RBC synaptic terminals. The immunofluorescence localization of TPBG to RBCs corroborates previous findings that TPBG mRNA is expressed primarily in RBCs [21]. The TPBG antibody also labeled a population of amacrine cells with cell bodies in the inner INL and dense dendritic projections to the middle of the IPL (**Figure 9F arrows**). The existence of a TPBG-positive amacrine cell population in the retina was observed by Imamura et al. in 2006 [129], but its identity has not been established.
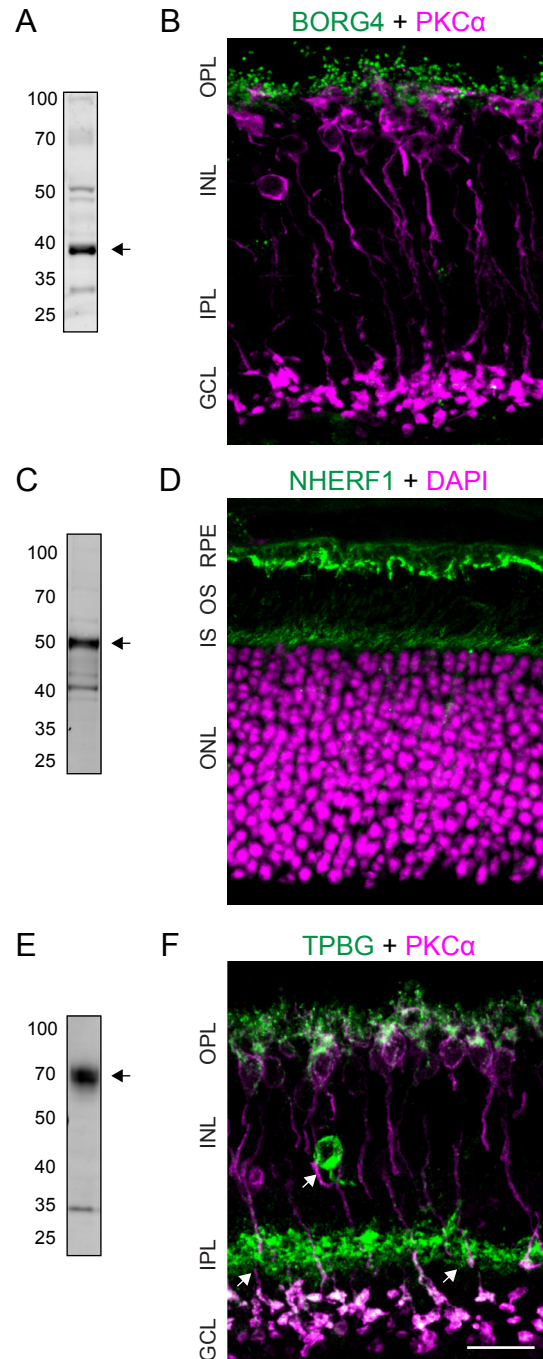
Figure 2.9: Validation of representative phosphoproteins in the mouse retina*. **(A)** Immunoblot of retinal lysate labeled with rabbit anti-BORG4 shows a band corresponding to BORG4 at ~38 kDa. **(B)** Confocal microscopy analysis of BORG4 and PKCα immunoreactivity in the retina using mouse anti-Cdc42EP2. **(C)** Immunoblot of retinal lysate shows a band corresponding to NHERF1 at ~50 kDa. **(D)** Confocal microscopy analysis of NHERF1 immunoreactivity in the retina with retinal layers labeled with DAPI. **(E)** Immunoblot of retinal lysate shows a smear corresponding to glycosylated TPBG at ~72 kDa. **(F)** Confocal microscopy analysis of TPBG and PKCα immunoreactivity in the retina. Scale bars: 20 μm. RPE: retinal pigment epithelium; OS: outer segments; IS: inner segments; ONL: outer nuclear layer; OPL: outer plexiform layer; INL: inner nuclear layer; IPL: inner plexiform layer; GCL: ganglion cell layer.

Discussion

RBCs are able to modulate their responses to changing light conditions and evidence suggests this process is regulated in part by PKCα [85–87]. The transient physiological effect of PKCα on the RBC dendrites is presumably mediated by its kinase activity, whereby PKCα-dependent phosphorylation changes the activity of downstream proteins. We show that RBC dendrites are the main sites of light- and PKCα-dependent phosphorylation (**Figure 2.1**). Using a conformation-specific PKCα antibody and an antibody mix that recognizes phosphorylated PKC substrate motifs, our results suggest that PKCα is active in light-adapted RBC dendrites. In the dark-adapted retina, PKCα is inactive and PKC substrate phosphorylation in the OPL is significantly reduced (**Figures 2.2A and 2.B**). Comparison of light-adapted wild type and PKCα-KO retinas confirmed that phosphorylation in RBC dendrites requires PKCα, and also indicated that phosphorylation in presumed cone bipolar cell dendrites is mediated by a different kinase. Deletion of TRPM1, a calcium-permeable cation channel responsible for signal transduction in ON-bipolar cell dendrites, also results in a significant reduction in RBC labeling with the conformation-specific PKCα antibody, suggesting that TRPM1-mediated calcium influx during the RBC light response is a primary source of calcium required for PKCα activation in RBC dendrites.

Differential abundance of retinal phosphopeptides between WT and PKCα-KO retinas could potentially be due to altered expression of proteins caused by the deletion of PKCα, and not due to changes in PKCα kinase activity. To identify proteins whose phosphorylation status is dependent on PKCα, but whose expression levels are unaffected, we compared both phosphoprotein and total protein abundance between WT and PKCα-KO mouse retinas using isobaric tagging and mass spectrometry. We identified over 4000 total proteins in either WT or PKCα-KO samples with 23 showing significantly different expression between groups. These proteins can be clustered into several general categories corresponding to biological ontology, most notably proteins involved in regulating cell shape and vesicle transport, transcriptional regulation, and homeostasis and metabolism. PKCα has been implicated in a variety of diverse cell signaling processes, including cell proliferation and morphology, inflammation, and tumorgenesis. Furthermore, PKCα activity has a major impact on gene expression by modulating transcription factors such as CREB, NF-κB, and c-REL [130]. Identifying proteins that show altered expression levels in PKCα-KO mouse retina could be valuable to the examination of many PKCα-dependent functions in RBCs, such as regulation of RBC morphology and development.

To identify RBC proteins that display PKCα-dependent phosphorylation, total retinal phosphopeptides were compared between wild type and PKCα-KO mice using isobaric tagging.

Normalizations and differential expression statistical testing for isobaric tagged phosphopeptides differs from traditional phosphoproteomic experiments where replicate numbers are smaller. When replicate numbers are greater than one or two, ratios are no longer an appropriate framework for the analysis. We extended our approach of working directly with aggregated reporter ion intensities for differential protein expression to phosphopeptide datasets. Our approach enables the use of robust statistical testing from genomics packages such as edgeR [119] or Limma [131]. The background of unchanged phosphorylation levels in the enrichment experiment, like that of the total protein experiment, was sufficient in these samples to use standard normalization approaches. Our normalizations and statistical testing for both experiments demonstrates that the same analysis steps used for total protein abundance can be successfully applied to the phosphopeptide datasets (S2 – Total Protein and Phosphopeptide Statistical Testing).

Of over 1100 distinct phosphopeptides identified by multiplex TMT mass spectrometry, 14 displayed significantly greater phosphorylation in wild type compared to PKCα-KO samples (**Figure 2.6**), suggesting their phosphorylation state is dependent on PKCα. These putative PKCα-dependent phosphoproteins may be phosphorylated directly by PKCα or may be phosphorylated by a different kinase whose activity is dependent on PKCα. Only one phosphoprotein, Dnmt3a, showed a significant decrease in abundance in PKCα-KO compared to WT in both the total protein and phosphopeptide experiments (**Figures 2.5 and 2.6**), indicating that reduced abundance of the Dnmt3a phosphopeptide may be due to downregulation of the protein in the KO. Three proteins, BORG4, NHERF1, and TPBG, displayed a particularly striking increase in phosphorylation in wild type compared to PKCα-KO samples (**Figures 2.6 and 2.7**). Of these proteins, BORG4 and NHERF1 are known substrates of PKCα [132,133].

Surprisingly, several of the major PKCα-dependent phosphoproteins identified in this study, including TPBG, do not conform to a strong consensus PKCα substrate motif, in which a phosphorylated serine is flanked by positively charged arginine and lysine residues (Kinexus Database; Vancouver, Canada; http://www.kinexusnet.ca). However, kinase substrate motifs are not always linear, contiguous sequences, but can also be formed structurally by bending of flexible loops that brings positively charged amino acids into proximity to the phosphorylated serine or threonine residues [134]. In the case of TPBG, the cytoplasmic domain is predicted to be unstructured and flexible, possibly allowing the phosphorylated serines at the C-terminal tail (S422 and S424) to be brought close to upstream pairs of lysines and arginines (R384 K385 and K388 and K389) to form a structural PKCα substrate motif. Alternatively, TPBG and other PKCα-dependent non-consensus phosphopeptides may be phosphorylated by a downstream kinase

that is dependent on PKCα activity. For example, casein kinase 2 (CK2) is a serine/threonine kinase that is activated by PKCα [135,136], and whose consensus substrate motif is a serine flanked by acidic residues (Kinexus Database). Two of the phosphopeptides that showed increased abundance in wild type samples compared to PKCα-KO contain a CK2 substrate motif (TPBG and Mfap2). The same site in Mfap2 has previously been demonstrated to be phosphorylated *in vitro*. The C-terminals of the NR2B subunit of the NMDA receptor is similar in sequence to the C-terminus of TPBG (LSSIESDV compared to LSSNSDV), and CK2 phosphorylation of the C-terminal serine in NR2B has been demonstrated to regulate trafficking of the receptor [137]. Ten phosphopeptides were more abundant in PKCα-KO samples than in wild type. These are likely to be phosphorylated by kinases that are inhibited by PKCα, such as GSK3 [138,139]. The consensus substrate motif for GSK3 kinase is a serine residue with a neighboring proline (Kinexus Database), and several of the phosphopeptides that are increased in the PKCα-KO samples fit this motif (examples: Dyn3, Crocc, Map2, and Rtn4).

We used immunofluorescence to localize three phosphoproteins that displayed the greatest differential phosphorylation between wild type and PKCα-KO samples. Immunofluorescence labeling of BORG4 resulted in bright puncta in the OPL (Figure 9) consistent with BORG4 localization to either RBC or horizontal cell dendrites, as well as immunofluorescence over most nuclei. BORG4 belongs to a protein family (BORG1-5) that bind to the Rho GTPase CDC42 as well as to septins, a family of GTP-binding cytoskeletal proteins that are involved in regulation of cell morphology through modulation of cytoskeletal rearrangement. BORG4 contains an N-terminal CCD42/Rac Interactive Binding Motif (CRIB) and three BORG Homology (BHs) domains that are conserved across all BORG family proteins [140]. Our proteomics data indicates that the serine residue S64 in BORG4, which is located between BH1 and BH2, is phosphorylated in a PKCα-dependent manner. Phosphorylation of BORG4 S64 has been previously recognized in large-scale analyses experiments of tissue-specific phosphorylation patterns [141,142] though not in retina. BORG4 and Septin-4 mRNAs have been previously found to be expressed in horizontal cells [143]. Our immunofluorescence labeling of BORG4 in retina resulted in bright puncta in the OPL consistent with BORG4 localization to either RBC or horizontal cell dendrites.

We detected NHERF1 immunofluorescence at the level of the photoreceptor inner segments in the region of the connecting cilia and in the retina pigment epithelium (RPE, Figure 9). NHERF1 is a scaffolding protein containing tandem PDZ domains and an Ezrin/Radixin/Moesin Binding (EB) domain. Our detection of strong NHERF1 immunofluorescence in the RPE consistent with previous reports localizing NHERF1 to the RPE

apical microvilli [144]. NHERF1 interacts with ezrin to maintain the structure of apical microvilli on epithelia. In the RPE, NHERF1 has been implicated in retinoid recycling [144] through its interactions with CRALBP [145,146]. PKCα is also expressed in the RPE [147] where it is involved in proliferation and migration [148], phagocytosis [149], and melanin production [150]; however, the specific role of PKCα-mediated phosphorylation of NHERF1 in the RPE is unknown.

Immunofluorescence confocal microscopy localized TPBG immunoreactivity to RBC dendrites and synaptic terminals, as well as to a class of amacrine cells (**Figure 9**). TPBG is a heavily glycosylated type-1 transmembrane protein with a large extracellular N-terminal domain and a short C-terminal intracellular tail. The N-terminal domain contains eight leucine-rich repeats (LRRs) and seven N-linked glycosylation sites. The C-terminal tail ends with the class-1 PDZ-interacting motif (S/T X Φ) SDV [151], which our proteomics data suggests is phosphorylated in a PKCα-dependent manner. Since phosphorylation of a PDZ-interacting motif typically prevents binding of a PDZ protein [152], PKCα might be regulating interactions between TPBG and PDZ proteins by stimulating phosphorylation of its C-terminal tail. As an oncofetal antigen, TPBG is present primarily during embryonic development [153,154], but is also expressed in many carcinomas [155]. In the adult, TPBG is expressed in the brain, retina, and ovaries [156,157]. In the embryo and in cancer tissue, TPBG is involved in regulating actin polymerization [158] filopodia formation [159], and chemotaxis [160,161], and its expression in tumors is linked to increased metastatic malignancy and poor survival outcomes in cancer patients [162,163]. In the adult olfactory bulb, TPBG is required to stimulate the development of input-dependent dendritic arborization and synaptogenesis of newborn granule cells [129,164–166]. The role of TPBG in the retina is not yet understood; however, a recent transcriptomic classification of retinal cell types identified TPBG mRNA as being highly enriched in RBCs [21]. This is consistent with our immunofluorescent analysis which localized TPBG to RBC dendrites and synaptic terminals.

Conclusions

The molecular mechanisms of PKCα-mediated modulation of the RBC light response have not been thoroughly explored. In this study, we have shown that PKCα phosphorylation in the retina occurs predominately in RBC dendrites in the light. Using a phosphoproteomics approach, we have identified a small number of phosphoproteins with significantly increased PKCα-dependent phosphorylation in the PMA-treated retina. These differentially phosphorylated proteins fall into several broad functional groups, including cytoskeleton/trafficking (4 proteins), structure and adhesion (2 proteins), cell signaling (2 proteins), transcriptional regulation (3

38

proteins), and homeostasis/metabolism (1 protein). Two strongly differentially expressed phosphoproteins, BORG4 and TPBG, are localized to the synaptic layers of the retina, and may play a role in PKCα-dependent modulation of RBC function.

Supplementary Materials

Supplementary File 2.1: Total protein and phosphopeptide results

Supplementary File 2.2: Total protein and phosphopeptide data analysis

Supplementary File 2.3: Annotated phosphopeptide spectra

Supplementary materials can be downloaded from:

Journal of Proteomics, June 2019

https://doi.org/10.1016/j.jprot.2019.103423

Chapter 3: Manuscript II

Expression and distribution of trophoblast glycoprotein in the mouse retina

Colin M Wakeham[1], Gaoying Ren[1], Catherine W Morgans[1]

[1]Department of Chemical Physiology & Biochemistry, Oregon Health & Science University, Portland, OR 97239, USA

Author contributions

Study design: CMW, CWM; Experimentation: CMW, GR; Figure and manuscript preparation: CMW, CWM; Editing and review: CMW, GR, CWM

Abstract

We recently identified the leucine-rich repeat (LRR) adhesion protein, trophoblast glycoprotein (TPBG), as a novel PKCα-dependent phosphoprotein in retinal rod bipolar cells (RBCs). Since TPBG has not been thoroughly examined in the retina, this study characterizes the localization and expression patterns of TPBG in the developing and adult mouse retina using two antibodies, one against the N-terminal LRR domain and the other against the C-terminal PDZ-interacting motif. Both antibodies labeled RBC dendrites in the OPL and axon terminals in the IPL, as well as putative amacrine cells with cell bodies in the inner nuclear layer (INL) and a dense layer in the middle of the inner plexiform layer (IPL). In live transfected HEK293 cells, TPBG was localized to the plasma membrane with the N-terminal LRR domain facing the extracellular space. TPBG immunofluorescence in RBCs was strongly altered by the loss of TRPM1 in the adult retina, with significantly less dendritic and axon terminal labeling in TRPM1 knockout compared to wild type, despite no change in total TPBG detected by immunoblotting. During retinal development, TPBG expression increases dramatically just prior to eye opening with a time course closely correlated with that of TRPM1 expression. In the retina, LRR proteins have been implicated in the development and maintenance of functional bipolar cell synapses, and TPBG may play a similar role in RBCs.

Introduction

Rod bipolar cells (RBCs) are the first excitatory interneurons in the primary rod pathway. They receive light-dependent synaptic input from rod photoreceptors in the outer plexiform layer (OPL) and contribute to retinal output via AII amacrine cells in the inner plexiform layer (IPL). RBCs have mostly been studied in the context of dark-adapted, low-light vision [167], yet evidence suggests that RBCs contribute to retinal output under a diverse range of lighting conditions. Under completely dark-adapted conditions, RBCs are sensitive to s[5,90]e-photon responses in rods [11,106], while under mesopic conditions, RBCs contribute to the perception of contrast [71,107]. In bright light, RBCs may modulate the cone pathway when rods are saturated [72]. The molecular mechanisms required for RBC adaptation to changing luminance conditions are mostly unknown, but compelling evidence implicates the commonly-used RBC marker protein kinase C-alpha (PKCα; [85–87,168]).

To gain insight into the mechanisms by which PKCα modulates the RBC light response, we sought to identify RBC proteins that undergo PKCα-dependent phosphorylation. Using a multiplexed tandem mass tag mass spectroscopy-based approach, we previously identified trophoblast glycoprotein (TPBG, also known as 5T4 or WAIF1 [Wnt-activated inhibitory factor 1])

as a novel PKCα-dependent phosphoprotein in RBCs [168]. TPBG is a type 1 transmembrane glycoprotein with an N-terminal extracellular domain composed of eight leucine rich repeats (LRRs) interspersed by seven N-linked glycosylation sites. The intracellular cytoplasmic domain is capped by a class 1 PDZ-interacting motif [151] and contains two serines, which were significantly more likely to be phosphorylated in wild type retinas compared to PKCα knockout [168].

TPBG was first identified in trophoblasts [169] and has been mainly studied in embryonic development and in cancer [156], where it is required for chemokine signaling [160,161], and where it is diagnostic for metastasis and poor prognosis in cancer patients [162,163]. In mammalian embryonic cell lines, TPBG influences cytoskeletal organization and cell motility through modulation of Wnt signaling [170], and has also been shown to interact with scaffolding protein to regulate cell-surface expression of receptors and transporters [158]. In adult tissues, it is expressed at high levels in ovary, brain, and retina [129,157]. Little is known about the role of TPBG in neurons except in the olfactory bulb, where TPBG has been shown to drive developmental changes in the dendritic morphology of granule cell interneurons in an activity-dependent manner, and genetic knockdown of TPBG resulted in impaired odor discrimination [164–166].

In the retina, a comprehensive single-cell drop-seq study identified TPBG as a possible new RBC marker and clustered it with proteins involved in lamination and adhesion [21]. In a subsequent comparative meta-analysis of RBC transcriptomics studies, it was grouped as a protein potentially implicated in synapse assembly [171]. TPBG's diverse functions in other tissues suggest potential roles in retinal morphology, synaptic development, and physiology. Since TPBG has never been thoroughly examined in RBCs, we sought to characterize its expression and distribution in both the adult and developing mouse retina, and in wildtype and TRPM1 knockout retina.

Methods

Antibody characterization

Rabbit anti-5T4 (anti-TPBG-CT) (1:500 [immunofluorescence], 1:5000 [immunoblot]; Abcam; Cambridge, UK; Cat# ab129058; RRID: AB_11144484) is a monoclonal antibody targeting a 15-amino acid synthetic peptide immunogen from amino acids 385-420 of human TPBG, which correspond to amino acids 391-426 of mouse TPBG with 100% sequence identity (BLAST; NCBI; Bethesda, MD). TPBG immunoreactivity was verified by the manufacturer via immunoblot of rat brain, HeLa cell, and HT-1376 cell lysates, and immunoprecipitation from MCF-7 cell lysates and detected broad bands of glycosylated proteins at 70-80 kDa (manufacturer information).

Rabbit anti-5T4 (anti-TPBG-NT) (1:1000; Thermo Fisher Scientific; Waltham, MA, USA; Cat# MA5-32120; RRID: AB_2801549) is a monoclonal antibody raised against amino acids 80-240 of human TPBG, which correspond to amino acids 80-246 of mouse TPBG with 78% sequence identity (BLAST; NCBI; Bethesda, MD). The manufacturer detected a band of glycosylated TPBG at 70-80 kDa via immunoblot of MCF-7 lysate.

Sheep anti-5T4 (anti-TPBG-NT-pAb) (1:500; R&D Systems; Minneapolis, MN, USA; Cat# AF5049; RRID: AB_2272148) is a polyclonal antibody raised against amino acids 30 to 361 of mouse TPBG. The manufacturer used flow cytometry and immunocytochemistry to detect TPBG in the membranes of retinoic acid-treated D3 mouse cell lines (manufacturer information). We confirmed specificity of all three antibodies by immunoprecipitation followed by immunoblotting from wild type mouse retinal lysate and TPBG-transfected HEK293 cells, with all antibodies detecting a broad band around 72 kDa.

Mouse anti-PKCα (1:5000; Sigma-Aldrich; St. Louis, MO, USA; Cat# P5704; RRID: AB_477375) is a monoclonal antibody that recognizes an epitope between amino acids 296-317 on the hinge region of mouse PKCα. The manufacturer detected bands at 80 kDa in immunblots of lysates from SH-SY5Y, SK-N-SH, COS7, and PC12 cell lines (manufacturer information), and we have verified this antibody by immunoblots of retinal lysates from wild type and PKCα knockout mice.

Mouse anti-CACNA1S (1:4000; Abcam; Cat# ab2862; RRID: AB_2069567) is a monoclonal antibody raised against full-length native rabbit CACNA1S subunit purified from the rabbit muscle T-tubule dihydropyridine receptor.

Mouse anti-CtBP2 (1:4000; BD Biosciences; San Jose, CA, USA; Cat# 612044; RRID: AB_399431) is a monoclonal antibody that binds an epitope within amino acids 361-445 the transcription factor CtBP2. The manufacturer used western blot analysis on BC3H1 cell lysates and detected a band at 48 kDa (manufacturer information). This antibody also reacts with ribeye, a component of synaptic ribbons [172], and produces strong immunoreactivity in both nuclei and synaptic ribbons in wild type mouse retina sections.

Mouse anti-calretinin (1:25; Santa Cruz Biotechnology; Dallas, TX, USA; Cat# sc-365956; RRID: AB_10846469) is a monoclonal antibody that recognizes an epitope between amino acids 2-27 at the N-terminus of human calretinin. The manufacturer used western blot analysis to detect bands between 23 and 34 kDa from human cerebellum, human brain, human adrenal gland, and rat cerebellum lysates (manufacturer information). We confirmed specificity by labeling wild type mouse retina sections and detected the characteristic three-band pattern of calretinin in the IPL.

Sheep anti-TRPM1 (1:2000) is a polyclonal antibody raised against a fragment of recombinant polypeptide corresponding to amino acids 1423-1622 of mouse TRPM [49]. We received this antibody from Kirill Martemyanov.

Mouse anti-β-actin (1:2500; Cell Signaling Technology; Danvers, MA, USA; Cat# 8H10D10; RRID: AB_2242334) is a monoclonal antibody that was verified in this study by immunoblot of wild type whole retinal lysates from mice at different developmental stages and shown to produce bands at ~42 kDa. The manufacturer used western blot analysis of extracts from COS, HeLa, C2C12, C6, and CHO cells to confirm immunoreactivity for β-actin.

The secondary antibodies used were AF488 anti-rabbit (1:1000; Jackson ImmunoResearch Labs; West Grove, PA, USA; Cat# 111-545-144; RRID: AB_2338052), AF488 anti-sheep (1:1000; Jackson ImmunoResearch Labs; Cat# 713-545-147; RRID: AB_2340745), Cy3 anti-mouse (1:1000; Jackson ImmunoResearch Labs; Cat# 115-165-003; RRID: AB_2338680), 680RD anti-rabbit (1:15000; LI-COR Biosciences; Lincoln, NE, USA; Cat# 925-68071; RRID: AB_2721181), 680RD anti-goat (sheep) (1:15000; LI-COR Biosciences; Cat# 925-68074; RRID: AB_2650427), and 800CW anti-mouse (1:15000; LI-COR Biosciences; Cat# 925-32212; RRID: AB_2716622).

Expression vector

The TPBG expression vector contains full-length mouse TPBG cDNA (NM_011627.4) inserted into the pCMV-sport6 plasmid (Thermo Fisher Scientific; Cat# 12209) provided by the PlasmID Repository (Clone ID: MmCD00318800; Species ID: 21983; Harvard Medical School; Boston, MA, USA).

Mice

Wild type mice used were C57BL/6J (Jackson Laboratory; Bar Harbor, ME, USA; Cat#000664, RRID: IMSR_JAX:000664). The TRPM1 knockout mice were TRPM1[tm1Lex] (Texas A&M Institute of Genomic Medicine; College Station, TX, USA; [45]. Mice of both sexes were used, and all mice were maintained on a 12-hour light/dark cycle and provided food and water ad libitum. Adult mice were 3-6 months old and postnatal mice were 0 to 13 days old. All animal procedures were in accordance with the National Institutes of Health guidelines and approved by the Oregon Health and Science University Institutional Animal Care and Use Committee.

HEK293 cell transfection

HEK293 cells (ATCC Cat# CRL-1573) were maintained at 37° C and 5% CO_2 in 1X DMEM medium (Thermo Fisher Scientific; Waltham, MA, USA; Cat# 11995-065, RRID: CVCL_0045) supplemented with 10% fetal bovine serum (Gemini Bio-Products Cat# 900-108) and 1% Pen/Strep (Thermo Fisher Scientific; Cat# 15140-122). For protein expression, approximately 10^5 cells were plated on coverslips (Thermo Fisher Scientific; Cat# 12-540-80) coated with poly-l-lysine (Sigma-Aldrich; Cat# P4704) in a 24-well dish. The next day, 0.2 ng of the pCMV-TPBG-sport6 vector was transfected using the Effectene transfection reagent kit (Qiagen; Venlo, Netherlands; Cat# 301525), and expression was assessed by immunostaining approximately 24 hours after transfection.

Immunostaining transfected HEK293 cells

Fixed and permeabilized cells: Cells grown on glass cloverslips were washed with 0.1 M $+Mg^{2+}/+Ca^{2+}$ phosphate buffered saline, pH 7.4 (PBS), fixed for 10 min in 4% paraformaldehyde (PFA), and then washed again with PBS. The cells were permeabilized and blocked by incubation with antibody incubation solution (AIS: 3% normal horse serum, 0.5% Triton X-100, 0.025% NaN_3 in PBS) for 30-60 min. Primary antibody diluted in AIS was added to the cells and incubated at room temperature for 1 hr, before being removed and the cells washed with PBS. Secondary antibody, also diluted in AIS, was added at room temperature for 1 hr, then removed. 1X DAPI was added to the coverslips for 1 min, before being washed off with PBS. The coverslips were then mounted on Super-Frost glass slides in Lerner Aqua-Mount (Thermo Fisher Scientific; Cat# 13800) and sealed.

Live cells: Cells grown on coverslips were washed with PBS and given fresh DMEM medium. Primary antibody was added directly to the medium, and the cells were placed on ice for 1 hr, after which they were washed with PBS, fixed with 4% PFA, and permeabilized with AIS. The remaining steps were identical to the previous section.

Tissue preparation for immunofluorescence

Mouse eyecups were prepared from freshly dissected eyes by cutting behind the ora serrata and removing the cornea and lens. Eyecups were fixed for 30 min by immersion in 4% PFA in PBS. The fixed eyecups were washed in PBS and then cryoprotected via sequential immersion in 10, 20, and 30% sucrose in PBS. The tissue was embedded in Tissue-Tek O.C.T. Compound (Sakura Finetek; Tokyo, Japan; Cat# 4583) and stored frozen at -80° C until

45

sectioning. Sections were cut at 20 μm thickness on a cryostat and then mounted onto Super-Frost glass slides. The slides were air dried and stored at -20° C.

Immunostaining retina sections

Retina sections were thawed and then blocked and permeabilized by incubation at room temperature for 60 min in AIS, and then were incubated in primary antibodies for 1 hr at room temperature. After washing with PBS, the sections were incubated in secondary antibodies diluted in AIS for 1 hr at room temperature. Finally, the sections were incubated for 1 min with 1X DAPI. The slides were washed again in PBS and then mounted with Lerner Aqua-Mount. For the anti-TPBG-CT and anti-TPBG-NT antibodies, retina sections were post-fixed for 10 min in 4% PFA before the blocking and permeabilization step as this was found to improve the immunofluorescence with these antibodies.

Confocal imaging

Immunofluorescence images were taken with a Leica TCS SP8 X white light laser confocal microscope (Leica; Wetzlar, Germany) using a Leica HC PL APO CS2 63x/1.40 oil immersion objective (Leica; Cat# 15506350) and Leica HyD hybrid detectors. Laser lines used were DAPI (405 nm), AF488 (499 nm), Cy3 (554 nm), and AF594 (598 nm). Detection windows used were DAPI (415-489 nm), AF488 (509-544 nm), Cy3 (564-758 nm), and AF594 (608-766 nm). Z-projections intended for comparison were processed in LAS X using identical tissue thickness. See Figure Legends for image stack number and Z-step thickness for each image. Brightness and contrast were adjusted equally across comparison groups using Leica LAS X or ImageJ [111]. The ImageJ "Smooth" tool was used to remove graininess from images.

Quantification of immunofluorescence was achieved by preparing slides with four wild type and four TRPM1 knockout sections and staining them simultaneously. Images were taken of each section with identical laser and detector settings. Brightness and contrast were corrected equally across images using ImageJ. For each section, DAPI and PKCα counterstaining was used to create 20 μm x 20 μm regions in the OPL, the middle of the IPL, and sublamina 5 of the IPL. Two such regions were averaged per layer for each image. Fluorescence intensity was quantified by normalizing the mean intensity of each region to that of a 20 μm x 20 μm region of background fluorescence in the ONL.

46

Immunoblotting

Retinas were extracted from freshly dissected eyes, suspended in chilled lysis buffer (50 mM Tris pH 7.4, 150 mM NaCl, 1 mM EDTA, 1% Triton X-100, 1% deoxycholate, 0.1% SDS) with 1X protease/phosphatase inhibitor cocktail (Cell Signaling Technology; Danvers, MA, USA; Cat# 5872) and homogenized with a Teflon-glass homogenizer. The lysate was centrifuged for 15 min at 16,400 rpm and 4° C, and the pellet was discarded. Lysates were stored at -20° C. Retinal lysates were diluted to $1\mu g/\mu l$ in lysis buffer and brought to 1X NuPAGE LDS Sample Buffer (Thermo Fisher Scientific; Cat# NP0007) and 1X NuPAGE Sample Reducing Agent (Thermo Fisher Scientific; Cat# NP0009). Pre-cast NuPAGE 1mm 4-12% Bis-Tris gels (Thermo Fisher Scientific; Cat# NP0322BOX) were loaded and run at 200 V and 140 mA for 55 min in 1X NuPAGE BOLT SDS Running Buffer (Thermo Fisher Scientific; Cat# B0001). Proteins were transferred onto PVDF membranes using a semi-dry transfer system and 2X NuPAGE Transfer Buffer (Thermo Fisher Scientific; Cat# NP00061) with 10% MeOH at 45 mA for 2 hrs, or a wet transfer system and 1X NuPAGE Transfer Buffer with 5% MeOH at 300mA for 2 hrs. The membranes were then rinsed with methanol and blocked for 1 hr in Odyssey Blocking Buffer TBS (LI-COR Biosciences; Cat# 927-50003) on a shaker at room temperature, before being incubated in primary antibody diluted in Odyssey buffer at 4° C overnight. The membranes were washed 3x5 min in TBST (Tris-buffered saline with 0.1% Tween-20), then incubated in secondary antibody diluted in Odyssey buffer for 1 hr at room temperature before being washed 3x5 min in TBST and left to dry. The dry blots were imaged using a LI-COR Odyssey CLx Imaging System at 700 and 800 nm.

Results

TPBG is expressed in the dendrites and axon terminals of rod bipolar cells.

Two rabbit monoclonal antibodies against different epitopes of human TPBG were used to localize TPBG in mouse retina. The first, anti-TPBG-CT, reacts with an epitope near the PDZ-interacting motif of TPBG's intracellular C-terminal tail, while the second, anti-TPBG-NT, binds within the extracellular N-terminal leucine-rich repeat (LRR) domain of TPBG. On immunoblots of retinal lysates, both antibodies label a single, broad band centered around 70 kDa, consistent with the size of glycosylated TPBG. Wild type mouse retina sections were labeled with either anti-TPBG-CT or anti-TPBG-NT, and the nuclear stain DAPI was used to identify the different retinal layers. The two antibodies gave indistinguishable results, further supporting the specificity of each antibody for TPBG. Immunofluorescent labeling with either anti-TPBG-CT (**Figure 3.1a-c**) or anti-

TPBG-NT (**Figure 3.1d-f**) revealed strong immunoreactivity in the OPL and in two bands in the IPL, one in the middle of the IPL (**arrows**) and the other at the innermost IPL. In the inner nuclear layer (INL), both TPBG antibodies label putative RBC cell bodies near the OPL as well as sparse cell bodies near the IPL (**asterisks**). Immunofluorescent double-labeling of TPBG and PKCα confirmed localization of TPBG to RBCs in retina sections (**Figure 3.1b, c, e, and f**).
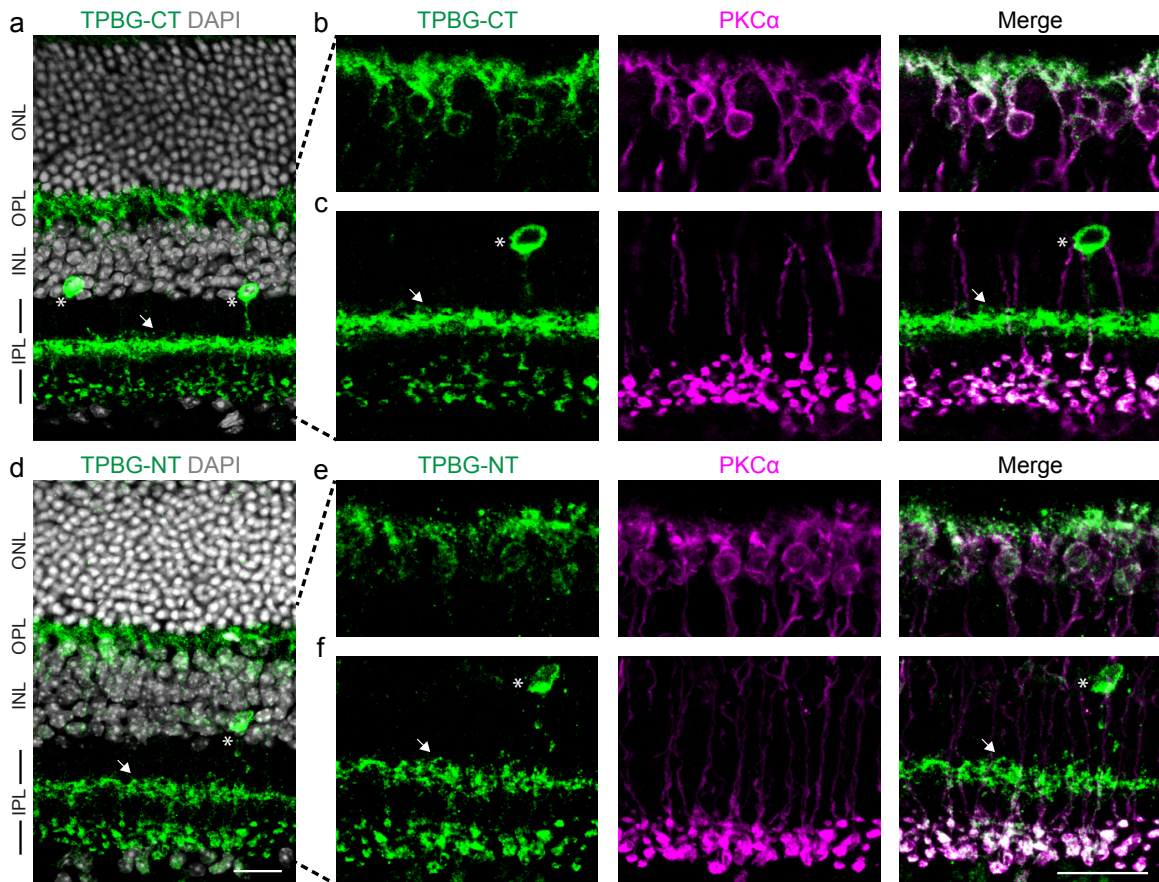
Figure 3.1: TPBG in the mouse retina. Three-channel confocal microscopy of wild type retina labeled with anti-TPBG-CT (**green; a-c**) or anti-TPBG-NT (**green, d-f**). DAPI (**gray; a and c**) was used to highlight the layers of the neural retina and anti-PKCα (**magenta; b and c [1.8X zoom of a] and e and f [1.8X zoom of d]**) was used to identify RBCs. Zoomed images were cropped into OPL (**top**) and IPL (**bottom**) panels to allow for separate intensity and contrast processing. Asterisks mark TPBG-positive cell bodies in the inner INL and arrows point to processes in the middle of the IPL. Sites of co-localization appear white. For a and d, Z-projections of 9 sections were used. For **b, c, e, and f**, Z-projections of 4 sections were used. For all images, the Z-step distance was 0.297 μm. Scale bars: 20 μm. ONL: outer nuclear layer; OPL: outer plexiform layer; INL: inner nuclear layer; IPL: inner plexiform layer.

TPBG immunofluorescence can be seen throughout the dendritic branches of RBCs in the OPL, as well as weaker labeling of their cell bodies in the outer INL (**Figures 3.1b and e**), and their axon terminals in the IPL (**Figure 3.1c and f**). In the OPL, anti-PKCα labels RBC cell bodies and dendrites, with the densest labeling occurring in the proximal dendrites close to the cell bodies. TPBG antibodies labeled the distal RBC dendrites more intensely than anti-PKCα. In the IPL, nearly complete co-localization of TPBG and PKCα in sublamina 5 confirms localization of TPBG

to RBC axon terminals. Finally, a sparse group of cells was also strongly reactive with anti-TPBG antibodies (**Figure 3.1 a, c, d, and f**), with cell bodies (**asterisks**) localized to the inner INL and projections to a dense, narrow layer in the center of the IPL (**arrows**).

In a dissociated retina preparation, anti-TPBG-CT (**Figure 3.2a**) and anti-TPBG-NT (**Figure 3.2b**) labeled PKCα-positive RBCs and, very rarely, a presumed amacrine cell (not shown). TPBG labeling of dissociated RBCs is more widespread throughout the cell compared to labeling of RBCs in retinal sections. This is likely due to disruption of protein synthesis and distribution of immunoreactivity caused by the dissociation procedure.
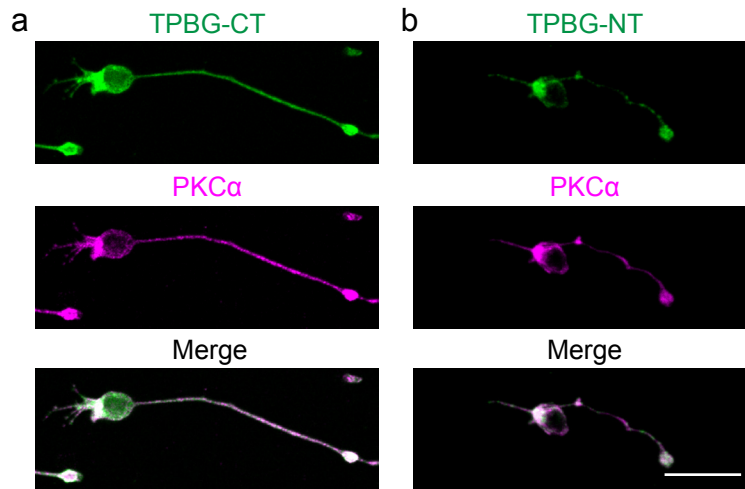
Figure 3.2: TPBG is expressed in rod bipolar cells. Confocal microscopy of dissociated wild type RBCs labeled with anti-TPBG-CT (**green; a**) or anti-TPBG-NT (**green; b**). Anti-PKCα (**magenta**) was used to identify RBCs. Sites of co-localization appear white. Z-projections of 3 sections were used with a Z-step distance of 0.297 μm. Scale bar: 20 μm.

To examine the dendritic distribution of TPBG in the mouse OPL, we compared TPBG-CT immunofluorescence with that of GPR179 and CtBP2 (**Figure 3.3**). GPR179 is localized exclusively to the dendritic tips of ON-bipolar cells where it is responsible for anchoring the RGS7-Gβ5 complex to the postsynaptic membrane [46,48,173] in proximity to mGluR6 [47,174]. To label GPR179, we used a monoclonal antibody to CACNA1S ($Ca_v1.1$) that has been shown to strongly cross-react with retinal GPR179 in the tips of ON-bipolar cell dendrites [175]. TPBG-labeled puncta do not overlap the putative GPR179 puncta at the very tips of the RBC dendrites, but do closely associate with them (**Figure 3.3a**). In the OPL, antibodies against CtBP2 label ribeye, a protein component of horseshoe-shaped synaptic ribbons in both cone and rod synaptic terminals [172]. TPBG immunofluorescent puncta lie within the concavity of a subset of horseshoe-shaped ribbons (**Figure 3.3b, asterisks**), indicating localization to RBC invaginating dendrites. Taken together, the double-labeling with these synaptic markers is consistent with the presence of TPBG in distal

RBC dendrites, but TPBG could not be clearly detected in the dendritic tips using immunofluorescence.
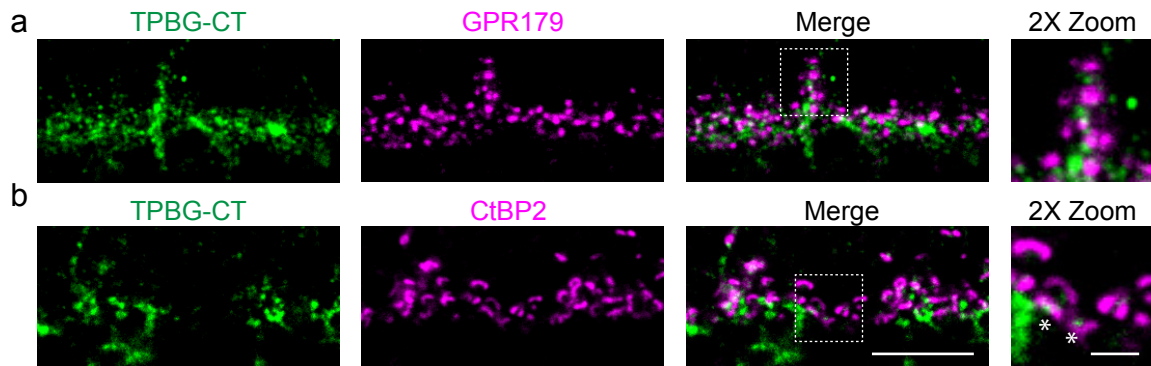
Figure 3.3: TPBG is present in distal RBC dendrites*. Confocal microscopy of wild type retina sections labeled for TPBG (**green**) and GPR179 (**magenta; a**) or CtBP2 (**magenta; b**). 2X zoom of boxed regions (**right panels**). Asterisks mark TPBG-positive puncta within CtBP2-positive synaptic ribbons. Sites of co-localization appear white. Z-projections of 3 sections were used with a Z-step distance of 0.297 μm. Scale bars: 10 μm (main panels); 2.5 μm (zoomed panels).
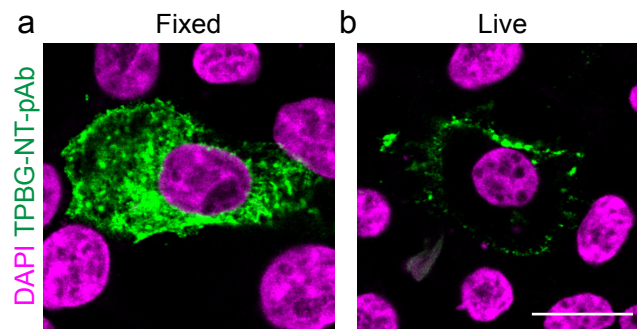
Figure 3.4: TPBG is localized to the plasma membrane in transfected HEK293 cells*. Confocal microscopy of **(a)** fixed and permeabilized and **(b)** live HEK293 cells transfected with cDNA corresponding to full-length mouse TPBG and labeled with an antibody against the extracellular domain of TPBG (anti-TPBG-NT-pAb). The nuclear stain DAPI (**magenta**) was used to label cell nuclei. Scale bars: 20 μm.

TPBG is localized to the plasma membrane in live transfected HEK293 cells.

Based on its structure and similarities with other LRR proteins, TPBG is expected to be oriented in the plasma membrane with its N-terminal LRRs facing the extracellular space and its C-terminus in the cytoplasm. Since immunofluorescence in retina sections could not clearly reveal the distribution of TPBG in RBCs, and because of disruption of surface proteins in dissociated preparations, we aimed to better visualize the distribution and membrane orientation of TPBG using HEK293 cells. HEK293 cells were transfected with full-length mouse TPBG and both fixed and live cells were labeled with a sheep polyclonal antibody against the N-terminal extracellular domain (anti-TPBG-NT pAb) (**Figure 3.4**). In fixed and permeabilized cells, the antibody labeled plasma membrane and cytoplasmic structures (**Figure 3.4a**). In live cells, the antibody only has

access to the extracellular surface; thus, the labeling of live cells (**Figure 3.4b**) confirms the predicted orientation of TPBG with the N-terminal, LRR domain facing the extracellular space.

TPBG is present in sublamina 2/3 of the IPL.

The IPL is divided into two layers corresponding to inputs from ON and OFF bipolar cells and can be further subdivided into five sublamina (2 OFF sublamina and 3 ON sublamina) based on labeling with immunofluorescence markers. One such IPL marker, calretinin, labels three distinct synaptic layers in the IPL corresponding to the sublamina 1/2, 2/3, and 3/4 boundaries [176]. Antibodies against TPBG labeled a dense synaptic layer in the middle of the IPL (**Figure 3.5; arrows**), overlapping with calretinin at the boundary between sublamina 2 and 3 between the ON and OFF regions of the IPL.
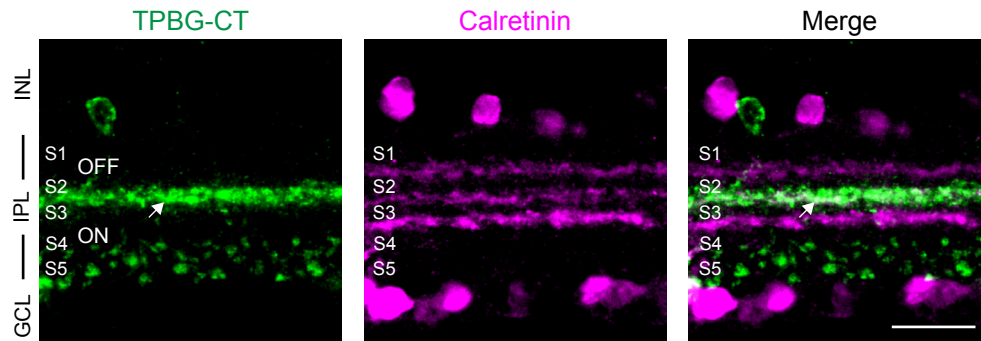
Figure 3.5: TPBG is present in sublamina 2/3 of the IPL. Confocal microscopy of wild type adult retina sections labeled for TPBG-CT (**green**) and calretinin (**magenta**). Layers were determined by DAPI nuclear staining (not shown), and sublamina were labeled based on calretinin staining. Z-projections of 5 sections were used with a Z-step distance of 0.415 μm. INL: inner nuclear layer; IPL: inner plexiform layer; GCL: ganglion cell layer. Scale bar: 10 μm.

TPBG immunofluorescence is reduced in TRPM1 knockout retinas.

Knockout of TRPM1 abolishes the RBC light response and significantly reduces PKCα-dependent phosphorylation in the retina [168]. TPBG shows PKCα-dependent phosphorylation, so to examine whether the loss of TRPM1 alters TPBG localization or expression, we compared wild type and TRPM1 knockout retinas by immunofluorescent labeling and immunoblotting retinal lysates with anti-TPBG-CT. To quantify TPBG expression in retina sections retinal layers were identified using DAPI and PKCα counterstaining and fluorescence intensity from different retinal layers was normalized to the nonspecific background fluorescence in the outer nuclear layer. In TRPM1 knockout retina, TPBG immunoreactivity in RBCs was significantly reduced compared to wild type, but the labeling in processes in sublamina 2/3 of the IPL were unaffected (**Figure 3.6a and b**). For the immunoblot analysis, bands at around 70 kDa corresponding to TPBG were normalized to β-actin bands within each sample to control for changes in total protein between

samples, and the knockout was normalized to the wild type. Surprisingly, there was no change in total TPBG levels as assessed via immunoblot analysis (**Figure 3.6c and d**).
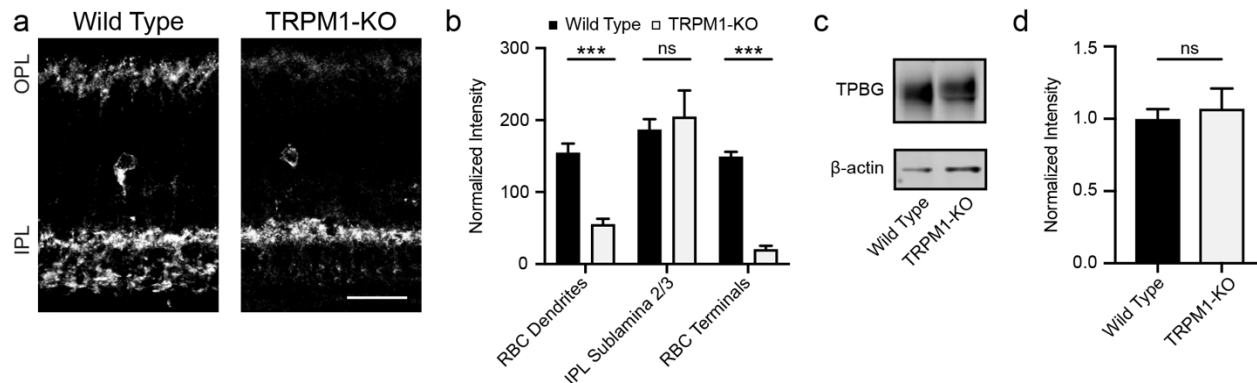
Figure 3.6: TPBG immunofluorescence is reduced in TRPM1-KO retinas. **(a)** Characteristic confocal microscopy of retina sections from wild type and TRPM1 knockout (TRPM1-KO) mice labeled for TPBG-CT. Z-projections of 10 sections were used with a Z-step distance of 0.297μm. **(b)** Quantification (mean + SEM) of TPBG fluorescence from different retinal layers normalized to the background fluorescence in the ONL (student's *t*-tests; RBC dendrites: $p < 0.001$; IPL sublamina 2/3: $p = 0.66$; RBC synaptic terminals: $p < 0.001$). **(c)** Characteristic immunoblot using anti-TPBG-CT and β-actin, and **(d)** quantification (mean + SEM) of TPBG band intensity (~72 kDa) normalized to β-actin (42 kDa) and then to the wild type condition (student's *t*-test: $p = 0.71$). $n = 4$ animals for both immunofluorescence and immunoblot analyses. Scale bar: 20 μm.

TPBG expression in the retina increases the day before eye opening.

To analyze the time-course of TPBG expression in the developing mouse retina, retinal lysates were extracted at different postnatal (P) days and probed via immunoblot with antibodies to TRPM1 and anti-TPBG-CT (**Figure 3.7a**) or anti-TPBG-NT (not shown; identical pattern). Both TPBG antibodies detected a significant increase in retinal TPBG expression the day before eye opening, which occurred between P12 and P13 in all three litters used, and is concomitant with an increase in the expression of TRPM1. Quantification of TPBG band intensities normalized to β-actin and to P0 (**Figure 3.7b**) showed that TPBG expression remains stable until P11, then increases approximately 10-fold by P12 and remains elevated. Quantification of TRPM1 band intensities (**Figure 3.7c**) revealed a similar pattern. The increase in TPBG expression around eye opening was also apparent in sections made from postnatal mouse retinas labeled with the anti-TPBG antibodies (only anti-TPBG-CT shown). TPBG immunofluorescence was undetectable in the P0 retina (not shown). In the P6 retina, the TPBG-positive cell bodies in the inner INL and labeling in sublamina 2/3 of the IPL are just visible (**Figure 3.7d; arrows**). By P11, TPBG can be faintly seen in RBC dendrites in the OPL (**Figure 3.7e; arrowheads**), but is still mostly absent from RBC axon terminals in sublamina 5 of the IPL. At P12 (**Figure 3.7f**), TPBG immunofluorescence in the OPL has dramatically increased, as has RBC axon terminal labeling in the IPL. By P13 (**Figure 3.7g**), after eye opening, RBC dendrites in the OPL are clearly visible when labeled for TPBG.
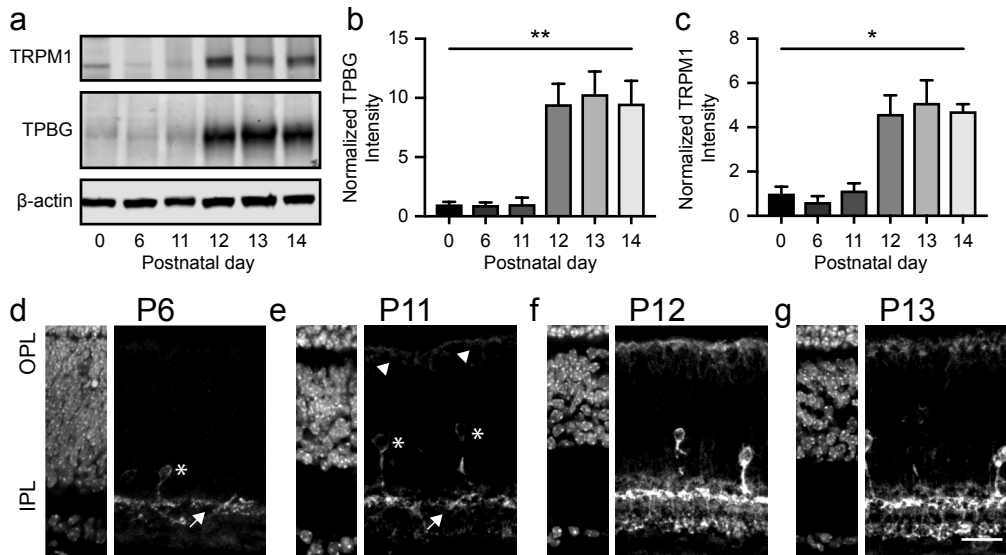
Figure 3.7: TPBG expression in the retina increases the day before eye opening. **(a)** Immunoblot of wild type retinal lysates prepared at different developmental time-points from the same litter and probed for TPBG-CT, TRPM1, and β-actin. Quantification (mean + SEM) of **(b)** TPBG-CT (one-way ANOVA: $F(5.00, 6.113) = 12.35$, $p = 0.0038$) and **(c)** TRPM1 (one-way ANOVA: $F(5.00, 2.778) = 12.95$, $p = 0.037$) immunoblot band intensity normalized to β-actin and then to the P0 timepoint. Confocal immunofluorescence microscopy of wild type mouse retina sections extracted at P6 **(d)**, P11 **(e)**, P12 **(f)**, and P13 **(g)** and labeled with DAPI (**left panels**) or for TPBG-CT (**right panels**). Asterisks mark TPBG-positive cell bodies in the INL, arrows point to processes in the middle of the IPL, and arrowheads point to RBC dendrites in the OPL. Eye opening occurred between P12 and P13. Z-projections of 7 sections were used with a Z-step distance of 1 μm. N=3 litters of at least 6 mice each for both immunofluorescence and immunoblot analyses. Scale bar: 20 μm.

Discussion

In this study, we have described the localization and expression patterns of TPBG in the mouse retina using two antibodies against intracellular and extracellular epitopes of TPBG. We found TPBG immunofluorescence primarily in the dendrites and axon terminals of RBCs, in cell bodies adjacent to the INL, and in processes that stratify in the middle of the IPL (**Figures 3.1 and 3.2**). In the OPL, TPBG labeling was closely associated with the RBC dendrites but was not clearly and consistently detected in the dendritic tips (**Figure 3.3**), localizing near, but not overlapping markers of RBC dendritic tips and rod synaptic ribbons. In HEK293 cells, transfected TPBG was primarily localized to the cell membrane with the N-terminal domain facing the extracellular space (**Figure 3.4**). In sublamina 5 of the IPL, antibodies against TPBG label RBC axon terminals, overlapping strongly with PKCα.

TPBG structure and function.

The N-terminal extracellular region of TPBG contains a heavily glycosylated [128] LRR domain – a common site of protein-protein interactions [151]. Several similarly structured transmembrane proteins have recently been identified as vital for the development of the rod-

RBC synapse or for localization of RBC synaptic transduction components. ELFN1, a synaptic adhesion LRR protein expressed in rod photoreceptors, forms trans-synaptic complexes with mGluR6 in RBC dendrites, and is required for the development of a functional synapse [100,101]. Two other synaptic LRR proteins, LRIT3 and nyctalopin, are required for the localization of TRPM1 to the tips of ON bipolar cell dendrites [49,50,53,54]. Our immunofluorescence data shows that TPBG is localized to RBC dendrites and in the RBC axon terminals. Structural similarities between TPBG and other LRR proteins suggest a possible role in the development or maintenance of RBC synapses.

The C-terminal intracellular region of TPBG is capped with a class 1 PDZ-interacting motif containing two serines (S422 and S424) that we have shown to be targets of PKCα-dependent phosphorylation [168]. Phosphorylation of PDZ-interacting motifs has been shown to regulate binding to PDZ domains. For example, the C-terminal PDZ-interacting motifs of NMDA receptor subunits NR2A and NR2B end with the amino acids SDV, and phosphorylation of the serine blocks binding of the receptor to the PDZ domain of PSD95 [137]. The PDZ-interacting motif of TPBG also ends with the amino acids SDV, but it is not known what PDZ domain proteins may interact with C-terminal TPBG in the retina. In other tissues, TPBG has been demonstrated by yeast two-hybrid screening to bind to the PDZ domain of GIPC1, a scaffolding protein that regulates cell surface expression of GPCRs [158] and that is expressed in RBCs [21]. Through interactions with scaffolding proteins like GIPC1, TPBG could regulate signal transduction by interacting with RGS proteins [177], and alter receptor targeting [178] or degradation [179].

TRPM1-dependent distribution of TPBG in RBCs.

TRPM1 is the mGluR6-coupled nonspecific cation channel responsible for the depolarizing light response in RBCs [43,45,125] and knockout of TRPM1 abolishes the RBC light response. We have previously shown that loss of TRPM1 in the mouse retina significantly reduces PKCα phosphorylation in the OPL [168], which may affect the expression or distribution of PKCα-dependent phosphoproteins such as TPBG. Immunofluorescent labeling of TPBG in RBCs by both antibodies was markedly affected by the loss of TRPM1, with reduced immunofluorescence in TRPM1 knockout retina compared to wild type (**Figure 3.6**). In contrast, TPBG expression in sublamina 2/3 of the IPL was unaffected, and the total amount of TPBG detected by immunoblot was unchanged. Together, our immunofluorescence and immunoblot results suggest that, when TPBG immunofluorescence in RBCs is reduced in the TRPM1 knockout, either TPBG is more diffusely distributed throughout the cells or antibody binding is occluded, potentially by light-dependent or phosphorylation-dependent protein interactions.

TPBG expression in the developing retina.

During retinal development, TPBG expression is undetectable by immunofluorescence at birth. The presence of TPBG in the putative amacrine cells is visible by P6, and in RBCs by P11. RBC expression increases dramatically between P11 and P12, just prior to eye opening (**Figure 3.7**). This pattern of increased expression approaching eye opening matches that of TRPM1, and is coincident with the gene expression patterns of many other proteins associated with the final stages of development of RBC signal transduction machinery and establishment of the rod to RBC synapse [143,180–182]. In embryonic development, TPBG alters Wnt and cytokine signaling to modulate cytoskeletal rearrangement and cell morphology [160,161,170]. In the developing mouse retina, Wnt signaling between rods and RBCs is required for functional synaptic targeting and OPL lamination, and knockout of Wnt5 resulted in rod/RBC mistargeting and the formation of ectopic OPL [183]. Similarly, Ccl5-mediated chemokine signaling was found to be required for RBC axon terminal targeting to AII amacrine cell dendrites in the IPL [184], suggesting that both Wnt- and chemokine-dependent mechanisms are active during RBC dendritic and axonal development. No relationship between TPBG and Wnt or chemokine signaling in the retina have yet been shown. However, as TPBG expression in RBCs increases concurrently with the activation of developmental processes dependent on these signaling pathways, and TPBG regulates both Wnt and chemokine signaling in other tissues, TPBG might be modulating similar signaling pathways in the retina.

TPBG-positive amacrine cells and IPL lamination.

We found that both antibodies against TPBG label an uncharacterized group of cell bodies in the INL and a dense synaptic layer between the ON and OFF sublamina in the IPL (**Figure 3.5**). A TPBG-positive amacrine cell with cell bodies near the IPL and dense processes stratifying in the middle of the IPL was first identified in a study focusing on TPBG in mouse olfactory bulb granule cells [129] and a TPBG-positive amacrine cell type was identified by single-cell transcriptome analysis of retina [185]. TPBG-promoter-driven expression of GFP labels a morphologically similar type of amacrine cell (Gensat Retina Project; www.gensat.org/retina.jsp). Based on similarities in cell body distribution and IPL lamination, we hypothesize that the TPBG-positive cell bodies and 2/3 sublamina labeling both come from the Type 47 (ac53-59) amacrine cell identified via connectomic reconstruction of the IPL, which was shown to receive inputs from cone bipolar cell 5D (XBC) and project outputs to two distinct populations of ganglion cells between the ON and OFF sublamina [26]. The sparse distribution and dense lamination, combined with the connectome data from Helmstaedter et al., indicates that this TPBG-positive amacrine

cell may have a medium-to-wide dendritic field and be coupled to both the ON and OFF pathways. While this evidence suggests that immunofluorescence from cell bodies in the INL and in the middle of the IPL come from the same uncharacterized amacrine cells, we cannot rule out potential contributions from other amacrine cell or ganglion cell synapses.

Summary

This study found that TPBG is localized to the dendrites and axon terminals of RBCs and the cell bodies and dendritic projections of an uncharacterized group of potential amacrine cells in mouse retina. TPBG immunofluorescence, but not total protein, was strongly reduced in the absence of TRPM1, possibly due to changes in protein distribution or protein interactions between knockout and wild type retina. TPBG is expressed in the developing and adult retina, suggesting a potential role both in the development and maintenance of RBC cellular physiology before and after eye opening. Based on TPBG's role in embryonic development, cancer pathogenesis, and the development and morphology of olfactory bulb interneurons, and its structural similarities to other synaptic LRR proteins, it is reasonable to predict that TPBG may be involved in the development and maintenance of RBC synaptic morphology and function.

Chapter 4: Manuscript III

Trophoblast glycoprotein is required for efficient synaptic vesicle release at rod bipolar cell ribbon synapses.

Colin M Wakeham[1], Gaoying Ren[1], Tammie L Haley[1], Qing Shi[1], Robert M Duvoisin[1], Henrique von Gersdorff[2], Catherine W Morgans[1]

[1]Department of Chemical Physiology & Biochemistry, Oregon Health and Science University, Portland, OR 97239, USA
[2]Vollum Institute, Oregon Health and Science University, Portland, OR 97239, USA

Author contributions

Study design: CMW, RD, HvG, CWM; Experimentation: CMW, TH, GR, HS; Data analysis: CMW, RD, HvG, CWM; Figure and manuscript preparation: CMW, RD, HvG, CWM; Editing and review: CMW, RD, HvG, CWM

Abstract

Rod bipolar cells (RBCs) faithfully transmit light-driven signals from rod photoreceptors in the outer retina to third order neurons in the inner retina. Recently, significant work has focused on the investigation of leucine-rich repeat (LRR) proteins that regulate synaptic development and control signal transduction at RBC synapses. We previously identified trophoblast glycoprotein (TPBG) as a novel transmembrane LRR protein localized to the dendrites and axon terminals of RBCs. We now examined the effects of TPBG genetic deletion on RBC physiology in mice using immunofluorescence and electrophysiological techniques. TPBG deletion did not affect the localization of synaptic proteins to the tips of RBC dendrites, TRPM1 currents, or RBC excitability. However, the scotopic electroretinogram showed a significant reduction in oscillatory potentials in the TPBG knockout. Because scotopic oscillatory potentials primarily reflect RBC-driven rhythmic activity of the inner retina, this result suggests that TPBG contributes to downstream signaling from RBCs to third order neurons. Membrane capacitance measurements indicated that TPBG deletion reduces synaptic vesicle exocytosis and subsequent GABAergic reciprocal feedback without altering L-type Ca^{2+} currents. Thus, TPBG is required for efficient neurotransmitter release from RBCs to downstream cells. Our results highlight a novel synaptic role for TPBG at RBC ribbon synapses and support further examination into the precise mechanisms by which TPBG regulates RBC physiology.

Graphical abstract

WT RBC axon terminal   TPBG-KO RBC axon terminal

L-type Ca^{2+} Channel
Glutamate
$GABA_AR$
$GABA_A\rho R$

ERG b-wave

Cl^- Ca^{2+}

TPBG

Reciprocal feedback

Glutamate release

ERG OPs
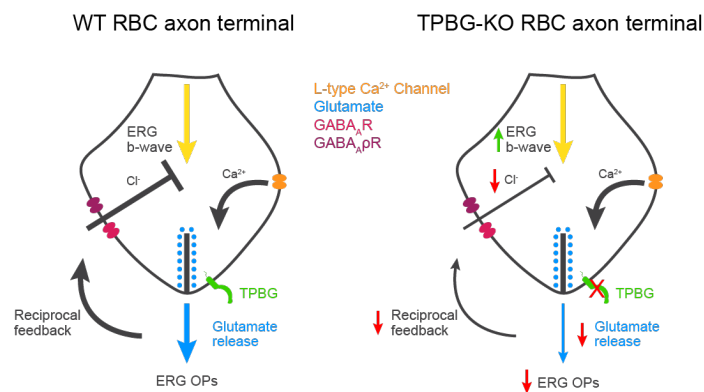
Introduction

Rod bipolar cells (RBCs) receive light-dependent synaptic input from rod photoreceptors in the outer plexiform layer (OPL) and drive retinal output by synapsing with AII amacrine cells (AII-ACs) in the inner plexiform layer (IPL). As the only dedicated bipolar cell in the primary rod visual pathway, RBCs must be able to reliably transmit visual signals over the whole range of rod

58

sensitivity. Accurate transmission of light signals requires precise synaptic targeting and tight control of signal transduction between RBCs and its synaptic partners. Identifying and characterizing the proteins required for the optimization and regulation of RBC synaptic development and function is essential for expanding our understanding of how RBCs contribute to vision.

Leucine-rich repeat (LRR) proteins form a large class of transmembrane proteins, each containing multiple leucine-rich motifs arranged to form extracellular protein binding domains [88,90]. Several LRR proteins identified in RBCs have been implicated in the development and maintenance of synaptic morphology and function. At synapses between photoreceptors and ON-bipolar cells, LRIT3 and nyctalopin are required for the localization of signal transduction components to the post-synaptic compartment [49,50,52–54,99]. In RBC dendrites, LRRTM4 forms a trans-synaptic complex with rod spherules [104], whereas in RBC axon terminals, LRRMT4 is required for functional GABA receptor clustering, reciprocal feedback inhibition, and dyad synapse formation [105]. The ELFN family of LRR proteins form trans-synaptic complexes between photoreceptors and bipolar cells without which functioning connections fail to develop and retinal circuitry is mis-wired [100,102].

We recently identified trophoblast glycoprotein (TPBG, also called 5T4 or WAIF1 (Wnt-activated inhibitory factor 1)) in a phosphoproteomics screen as a novel LRR transmembrane glycoprotein in mouse RBCs that undergoes PKCα-dependent phosphorylation [168]. TPBG contains eight N-terminal extracellular LRR motifs and a short intracellular C-terminal tail with a PDZ-interacting domain [151]. TPBG localizes to the dendrites and synaptic terminals of RBCs and its expression is closely linked to eye opening and TRPM1 expression, suggesting that TPBG may play an important role in RBC development or physiology [186].

Because the role of TPBG in the retina has not been established, we sought to characterize the effects of genetic knockout of TPBG in mouse RBCs using immunofluorescence confocal microscopy and electrophysiological techniques. RBC synapses form specialized active zones, each containing a synaptic ribbon, that permit a greater bandwidth of information transfer than conventional synapses. Ribbon synapses are noted for tight vesicle-Ca^{2+} coupling and a large supply of readily-available synaptic vesicles tethered close to the active zone [12,187,188]. In this study, we report that TPBG is required for efficient synaptic vesicle fusion and neurotransmitter release at RBC ribbon synapses, implicating TPBG in ribbon synapse development and/or function.

Methods

Animals and statistical analysis

Constitutive TPBG knockout (TPBG-KO; KO) mice were B6;129S5-Tpbg[tm1Lex]/Mmucd (MMRRC; UC Davis; Davis, CA, USA; Cat# 031630-UCD; RRID: MMRRC_031630-UCD). KO mice were purchased as cryopreserved sperm and reconstituted into a C57BL/6J (The Jackson Laboratory; Bar Harbor, M; Cat# 000664; RRID: IMSR_JAX:000664) background. Age-matched homozygous wild type (WT) littermates were used as controls. We used mice of both sexes and all mice were maintained on a 12-hour light/dark cycle and provided food and water ad libitum. Animals for immunofluorescence and electroretinogram experiments were 3-6 months old while animals used for patch clamp electrophysiology experiments were 3 months old. All animal procedures were in accordance with the National Institutes of Health guidelines and approved by the Oregon Health & Science University Institutional Animal Care and Use Committee.

Statistical analyses were performed in Prism 9 (GraphPad; San Diego, CA, USA) and reported as mean $\pm$ SEM. We detected significance between conditions using unpaired Welch's *t*-tests and Brown-Forsythe ANOVA tests. Statistical significance is noted by asterisks (not significant (ns): $p > 0.05$; *: $p < 0.05$; **: $p < 0.01$; ***: $p < 0.001$; ****: $p < 0.0001$).

Immunofluorescence

Fresh eyecups were dissected by cutting behind the ora serrata and removing the cornea and lens. For sectioning, eyecups were fixed for 30 min by immersion in fresh 4% paraformaldehyde (PFA) in PBS. The fixed eyecups were washed in PBS and then cryoprotected via sequential immersion in 10, 20, and 30% sucrose in PBS. Sections were cut at 20 μm thickness. Retina sections were post-fixed for 10 minutes in 4% PFA, blocked and permeabilized by incubation at room temperature for one hour in antibody incubation solution (AIS; 3% normal horse serum, 0.5% Triton X-100, 0.025% NaN_3 in PBS), and then incubated in primary antibodies for one hour at room temperature. After washing with PBS, the sections were incubated in secondary antibodies diluted in AIS for one hour at room temperature. The slides were washed again in PBS and then mounted with VECTASHIELD PLUS antifade mounting media with DAPI (Vector Laboratories; Cat# H-2000-10).

For whole mount immunofluorescence, eyecups were fixed for 45 min by immersion in fresh 4% PFA in PBS. The fixed eyecups were washed in PBS then dissected into flat mounts and blocked and permeabilized for one hour in AIS. The retinas were incubated in primary antibodies diluted in AIS for four days at 4° C then washed overnight in PBST (0.05% Triton-X) at

4° C. Retinas were incubated in secondary antibodies in AIS overnight at 4° C then washed again in PBST. Finally, the retinas were mounted with VECTASHIELD PLUS antifade mounting media. Immunofluorescence images were taken with a Leica TCS SP8 X white light laser confocal microscope (Leica Biosystems; Wetzlar, Germany) using a Leica HC PL APO CS2 63x/1.40 oil immersion objective (Leica; Cat# 15506350). Brightness and contrast were adjusted equally across genotypes using Fiji [189]. A Gaussian blur using a radius of 0.5 pixels was used to remove graininess from images. For image analysis of RBC axon terminals, a PKCα binary was created in Fiji using default auto-thresholds to isolate RBC axon terminals. This binary was then merged with the other channels to isolate PKCα-positive fluorescence. See figure legends for specific information on Z-step distance and number of steps.

Immunoblotting

Retinas were extracted from freshly dissected eyes, suspended in chilled lysis buffer (50 mM Tris pH 7.4, 150 mM NaCl, 1 mM EDTA, 1% Triton X-100, 1% deoxycholate, 0.1% SDS) with 1X protease/phosphatase inhibitor cocktail (Cell Signaling Technology; Danvers, MA, USA; Cat# 5872) and homogenized with a Teflon-glass homogenizer. The lysate was centrifuged for 15 minutes at 16,400 rpm and 4° C, and the pellet was discarded. Retinal lysates were diluted to 1 μg/μl in lysis buffer and brought to 1X NuPAGE LDS Sample Buffer (Thermo Fisher Scientific; Cat# NP0007) and 1X NuPAGE Sample Reducing Agent (Thermo Fisher Scientific; Cat# NP0009). Pre-cast NuPAGE 1 mm 4-12% Bis-Tris gels (Thermo Fisher Scientific; Cat# NP0322BOX) were loaded and run at 200 V and 140 mA for 55 minutes in 1X NuPAGE BOLT SDS Running Buffer (Thermo Fisher Scientific; Cat# B0001).

Proteins were transferred onto PVDF membranes a wet transfer system and 1X NuPAGE Transfer Buffer with 5% MeOH at 300 mA for two hours. The membranes were then rinsed with methanol and blocked for one hour in Odyssey Blocking Buffer TBS (LI-COR Biosciences; Cat# 927-50003) on a shaker at room temperature, before being incubated in primary antibody diluted in Odyssey buffer at 4° C overnight. The membranes were washed in TBST (Tris-buffered saline with 0.1% Tween-20), then incubated in secondary antibody diluted in Odyssey buffer for one hour at room temperature before being washed in TBST. Dried blots were imaged using a LI-COR Odyssey CLx Imaging System at 680 and 800 nm.

Electroretinogram recording

Mice were dark-adapted overnight and prepared for recording under dim red light. Anesthesia was initiated via IP injection of ketamine:xylazine (100:10 mg/kg) and maintained with

booster injections (30:3 mg/kg) at approximately 30 minute intervals until completion of the experiment. Body temperature was maintained at 36.5-38° C. Before recording, the pupils were dilated with 2.5% phenylephrine and 1% tropicamide, and the cornea was anesthetized with 1% topical proparacaine. A wire loop placed under the upper teeth was used to draw the mouse into a custom-made holder, which stabilized the head and permitted delivery of 95% O_2/5% CO_2 (carbogen; ~0.25 l/min). The recording was made using a custom contact lens electrode featuring a central platinum wire placed against the cornea with a small drop of hypromellose to prevent drying. A loop electrode placed behind the eye served as a reference electrode and a needle electrode placed in the tail served as a ground. The mice were placed in a Ganzfield sphere and light stimuli were provided by custom 502 nm LED photostimulators. Light stimulus intensity was controlled with neutral density filters and by altering flash duration and was measured post-hoc with an ILT5000 radiometer (International Light; Newburyport, MA; USA) with a scotopic filter. Traces were recorded with customized software (ERGLab; Richard Weleber; Casey Eye Institute; Portland, OR, USA).

Full-field scotopic electroretinograms (ERGs) from both eyes were recorded simultaneously after a series light flashes ranging from 2.29×10^{-5} to 2.57×10^2 cd•s/m^2 (-4.64 to 2.41 log(cd•s/m^2); [87]. For dim intensities (-4.64 to -2 log(cd•s/m^2)), ERGs were the averages of 8-25 light responses with inter-flash intervals of 10 seconds. For mid-range intensities (-2 to 0 log(cd•s/m^2)), three trials were averaged with inter-flash intervals of 20 seconds. For bright intensities (0 to 2.41 log(cd•s/m^2)), two trials were averaged with inter-flash intervals of 30 to 120 seconds.

ERGLab data was exported for offline processing using a custom Python script and the SciPy package (https://docs.scipy.org/doc). Statistical analyses were performed in Prism 9 (GraphPad; San Diego, CA, USA). The start of the flash stimulus was set to time zero and traces were baselined. OPs were isolated with a Butterworth band-pass filter (30-300 Hz) and the "signal.filtfilt" function in SciPy (**Figure 4.2A**). For intensities below -2 log(cd•s/m^2), b-wave amplitudes were measured from baseline-to-peak. For intensities above -2 log(cd•s/m^2), the a-wave amplitudes were measured from baseline-to-trough and b-wave amplitudes were measured from a-wave trough-to-b-wave peak. Where a-waves are present, the b/a-wave ratio was calculated to normalize responses. OP amplitude was measured from trough-to-peak of the largest wave and the OP/b-wave ratio was calculated using b-wave amplitudes from the same recording.

Patch clamp electrophysiology

Retinas were isolated and embedded in 3% low melting point agarose (Sigma; Cat# A0701) in carbogenated bicarbonate-buffered Ames medium (Ames & Nesbett, 1981; Ames Medium w/L-Glutamate; US Biological; Swampscott, MA, USA; Cat# A1372-25) and 200-250 μm slices were prepared with a Leica VT1200 vibrating microtome. For chemically simulated light response experiments, retinas were sliced in carbogenated Ames. For all other recordings, slicing was performed in chilled and carbogenated low-Na$^+$, high-sucrose cutting solution containing (in mM): 210 sucrose, 35 NaHCO$_3$, 20 HEPES, 10 glucose, 6 MgCl$_2$, 3 sodium pyruvate, 2.5 KCl and 0.5 CaCl$_2$ and buffered to pH 7.4 with NaOH. Retina slices were stored at room temperature in carbogenated Ames medium before being transferred to the recording chamber. Heated (31-33° C) Ames medium was continuously perfused over the retinal slices during all patch-clamp recordings.

Thick-walled borosilicate glass pipettes (World Precision Instruments; Sarasota, Fl, USA; Cat# 1B150F-4) were pulled using a Narishige puller-PP830 (Tokyo, Japan). Ultrapure salts were purchased from Sigma-Aldrich (St. Louis, MO, USA). For RBC visualization, the fluorescent tracer Alexa Fluor 594 Hydrazide (100 μM; Thermo Fisher Scientific; Cat# A10438) was added to the pipettes. Whole-cell voltage-clamp and current-clamp recordings were performed in photopic conditions using a double EPC-10 patch clamp amplifier controlled by Patchmaster software (HEKA Elektronik, Lambrecht/Pfalz, Germany) or an Axon Axopatch 200B controlled by pCLAMP software (Molecular Devices; San Jose, CA, USA). Data was acquired at a 20 kHz sampling rate and filtered with a 2.9 kHz low-pass Bessel filter. RBCs were targeted visually using Dodt gradient contrast microscopy and confirmed post-hoc with cell-filling and epifluorescence microscopy. Both pCLAMP and Patchmaster data sets were exported to Igor Pro (WaveMetrics, Lake Oswego, OR, USA) for offline analysis with custom Igor scripts and statistical analysis was performed in Prism. We used a P/10 leak subtraction in voltage-clamp to isolate L-type Ca^{2+} currents and GABAergic feedback currents; leak traces for each trial were baselined, summated, and subtracted from the raw pulse trace.

To record chemically simulated light responses, pipettes were pulled to 10-12 MΩ and backfilled with a potassium gluconate solution containing (in mM): 125 K-gluconate, 8 KCl, 5 HEPES, 1 MgCl$_2$, 1 CaCl$_2$, 3 adenosine 5'-triphosphate magnesium salt (Mg-ATP), 0.5 guanosine 5'-triphosphate disodium salt (Na$_2$-GTP), and 5 EGTA, and pH was adjusted to 7.3 with KOH. The Ames medium was supplemented with 4 μM L-(+)-2-amino-4-phosphonobutyric acid (L-AP4), an mGluR6 agonist to maintain a simulated dark-adapted state. A puffer pipette (12-18 MΩ) was maneuvered into the dendritic field of the target cell, and the cell was patched in voltage-clamp

and held at -60 mV. The potent mGluR6 antagonist [RS]-α-cyclopropyl-4-phophophenylglycine (CPPG) was applied directly to the dendrites using a Picospritzer II (Parker Hannifin; Hollis, NH, USA; 600 μM at 20 psi) for five seconds and the RBC response was recorded. For each cell, four sweeps were recorded at 15-second intervals.

For current-clamp experiments, pipettes were pulled to 9-12 MΩ and backfilled with a potassium gluconate solution containing (in mM): 104 K-gluconate, 10 KCl, 10 HEPES, 4 Mg-ATP, 0.4 Na_2-GTP, 10 Na_2-Phosphocreatine, and 2 EGTA, and pH was adjusted to 7.3 with KOH. The Ames medium was supplemented with 1 mM $CaCl_2$ and the synaptic blockers (in μM): 0.5 strychnine (glycine receptor blocker), 3 gabazine (SR 95531; GABA$_A$ receptor blocker), 50 [1,2,5,6-tetrahydropyridin-4-yl]methylphosphinic acid (TPMPA; GABA$_A\rho$ receptor blocker), and 4 L-AP4 (mGluR6 agonist) to block excitatory and inhibitory inputs. The total external $CaCl_2$ concentration was estimated to be 2.25 mM. Cells were first patched in voltage-clamp and then the amplifier was switched to fast current-clamp mode using the EPC-10 Gentle CC-Switch feature. Resting membrane voltage was recorded at 0 pA and then current was injected for 100 ms from -80 pA to 80 pA in 20 pA steps. Instantaneous voltage was measured as the peak (min or max) voltage immediately after the onset of the current pulse, and sustained voltage was measured as the average over the final 10 ms of the pulse. For each cell, five sets of sweeps were recorded at five-second intervals.

For the remaining experiments, the pipettes were pulled to 5-8 MΩ and backfilled with a cesium gluconate solution containing (in mM): 94 Cs-gluconate, 10 HEPES, 20 tetraethyl ammonium chloride (TEA-Cl), 4 Mg-ATP, 0.4 Na_2-GTP, 10 Na_2-Phosphocreatine, and 2 EGTA, and pH was adjusted to 7.3 with CsOH.

For voltage-clamp time-resolved capacitance recordings, the Ames medium was supplemented with 1 mM $CaCl_2$ and 0.5 strychnine, 3 gabazine, 50 TPMPA, and 4 L-AP4 to isolate L-type Ca^{2+} currents and maximize membrane resistance. Pipettes were wrapped with parafilm to reduce pipette capacitance and electrical noise. Membrane capacitance (C_m), membrane resistance (R_m), and series resistance (R_s) were measured using the "sine + DC" method implemented in Patchmaster software [190–192]. Exocytosis was evoked in voltage-clamp mode with a 100 ms depolarizing pulse from -80 mV to -10 mV to activate L-type Ca^{2+} currents. Resting C_m was measured using a sinusoidal voltage command (200 Hz, 30 mV trough-to-peak) superimposed over the membrane holding potential (-80 mV) and one measurement was generated per cycle (**Figure 4.5A**). An increase in exocytosis (ΔC_m) was measured from the change in C_m values before and after the depolarizing pulse. A baseline was established by averaging the resting C_m over the one second immediately preceding the voltage step. C_m

measurements for 500 ms after repolarization were excluded from analysis to allow for the full decay of evoked conductances, and C_m was averaged over the following 500 ms. Cells were discarded if changes in C_m correlated with changes in R_m or R_s. For each cell, five sets of sweeps were recorded with 15 second intervals. To remove noise, C_m data was filtered through a 5 Hz low-pass FIR filter. When different frequency sinusoidal voltage commands were used (in **Figure 4.5**), recordings were resampled to 200 Hz for ease of comparisons.

To record reciprocal inhibitory currents, the Ames medium was supplemented with 1 mM $CaCl_2$, 4 μM L-AP4 to block spontaneous excitatory inputs from rods, and 0.5 μM strychnine to block glycinergic inhibition. Feedback current was evoked in voltage-clamp mode with a 100 ms depolarizing pulse from -80 mV to -10 mV to activate L-type Ca^{2+} currents and subsequent outward GABAergic inhibitory currents. Inhibitory current amplitudes were measured from baseline established at the peak inward current after depolarization, which was very similar to peak L-type Ca^{2+} currents in **Figure 4.6**. Sustained currents were averaged over the final 10 ms of the depolarizing pulse, and charge transfer was measured as the area between the curve and the baseline. Five sets of sweeps were recorded at five-second intervals.

Results

TPBG is not required for gross RBC morphology

We use the constitutive Tpbg knockout mouse line B6;129S5-Tpbg[tm1Lex]/Mmucd (referred to as TPBG-KO or KO) to analyze the consequences of genetic deletion of TPBG. Wild type (WT) littermates were used as controls. First, we examined the expression and localization of TPBG using immunofluorescence microscopy and immunoblotting. We labeled WT and TPBG-KO retina sections with the nuclear stain DAPI and an antibody against TPBG (**Figure 4.1A**). As previously reported [186], the TPBG antibody labels RBC cell bodies, dendrites, and axon terminals in the WT retina as well as a narrow band in the middle of the IPL corresponding to the processes of TPBG-expressing ACs. TPBG immunofluorescence was absent throughout the KO retina, which we then confirmed with immunoblotting (**Figure 4.1B**) of WT, Het, and KO retinal lysates using β-actin as a loading control. Using an antibody against PKCα in WT and TPBG-KO retina, we found no discernable disruption in morphology of RBC dendrites or axon terminals in KO retinas (**Figure 4.1C**).
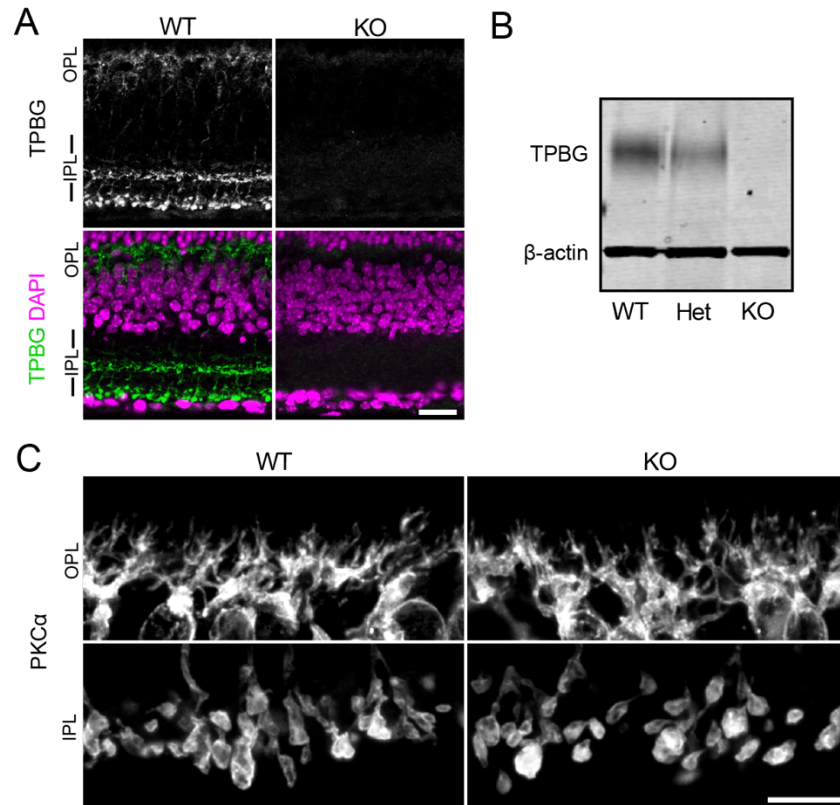
Figure 4.1: TPBG-KO does not alter gross RBC morphology. **(A)** Immunofluorescence confocal microscopy of WT (left) and TPBG-KO (KO; right) retina sections labeled with an antibody against TPBG (green). The nuclear stain DAPI (bottom; magenta) was used to highlight the neuronal layers of the retina. **(B)** Immunoblot of WT, Het, and TPBG-KO (KO) retinal lysates probed for TPBG and the loading control β-actin. The two channels were imaged separately and merged. **(C)** Confocal microscopy of WT (left) and TPBG-KO (KO; right) sections labeled with an antibody against PKCα. Images were cropped into OPL (top) and IPL (bottom) for separate intensity and contrast processing. For all images, Z-projections of 11 sections were used with a Z-step distance of 0.415 μm for a total thickness of 4.57 μm. Intensity and contrast was adjusted equally across genotypes. OPL: outer plexiform layer; IPL: inner plexiform layer. Scale bars: **(A)** 20 μm; **(B)** 10 μm.

Genetic knockout of TPBG alters the scotopic ERG light response

The light response of RBCs is reflected in the b-wave of the dark-adapted (scotopic) full-field electroretinogram (ERG), a commonly-used technique for recording the electrical responses of the whole retina *in vivo*. Different components of the ERG waveform correspond to the activity of specific cell types in the retina. The a-wave is an initial negative deflection corresponding to hyperpolarization of the photoreceptors [193], whereas the b-wave, a larger and slower positive deflection, primarily corresponds to the subsequent depolarization of the ON-type bipolar cells [194]. Rod driven activity can be isolated by dark-adapting the mouse before testing; therefore, the dark-adapted ERG b-wave represents the activity of RBCs in response to light stimuli.
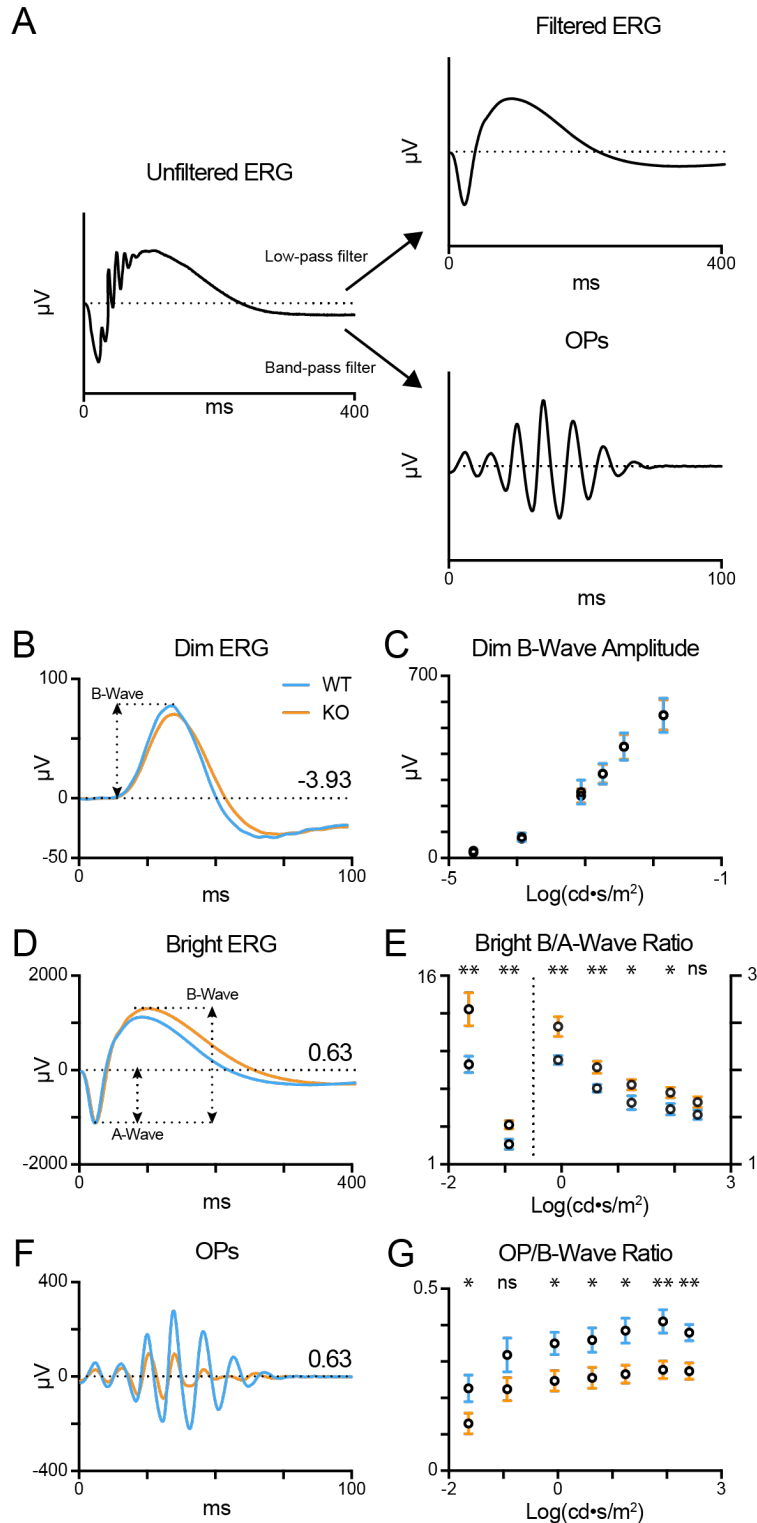
Figure 4.2: TPBG-KO alters the scotopic ERG after bright stimuli. Scotopic electroretinograms (ERGs) were recorded from dark adapted WT (blue; n = 12) and TPBG-KO (KO; orange; n = 14) mice after exposure to varying light stimuli. Stimuli were categorized as dim if no a-wave was present (-4.64 to -2.43 log(cd•s/m^2)) and bright if an a-wave was present (-1.64 to 2.41 log(cd•s/m^2)). **(A)** After baselining, OP contamination was removed from the unfiltered ERG using a low-pass filter (top right) before measuring a-wave and b-wave amplitudes from the filtered ERG. A Butterworth band-pass filter (bottom right) was used to isolate OPs for analysis of OP/b-wave ratios. **(B)** Example average ERG recordings after light stimuli of -3.93 log(cd•s/m^2). Since no a-wave was present, b-wave amplitudes were measured

from baseline to b-wave peak. **(C)** Quantification of b-wave amplitudes recorded after dim stimuli. **(D)** Example average ERG recordings after bright light stimuli of 0.63 log(cd•s/m^2). A-wave amplitudes were measured from baseline to the a-wave trough and b-wave amplitudes were measured from the a-wave trough to the b-wave peak. **(E)** Quantification of b-wave amplitudes normalized to a-wave amplitudes. To ease visualization, data points to the left of the dotted line refer to the left Y axis, and data points to the right of the dotted line refer to the right Y axis. **(F)** Example average oscillatory potentials (OPs) after light stimuli of 0.63 log(cd•s/m^2). **(G)** OP amplitude normalized to b-wave amplitude after bright stimuli. OP amplitudes were measured from the trough to peak of the largest wave. Experiments were performed in 3-6-month-old anesthetized mice. See **Figure 4.11: Figure Supplement 2** for a table of data quantified in **B**, **D** and **F**. Quantified data is presented as the mean ± SEM. Statistical significance was determined using Welch's *t*-tests; ns: $p > 0.05$; *: $p < 0.05$.

We recorded the scotopic ERG light responses in dark-adapted anesthetized WT (blue; *n* = 12) and TPBG-KO (KO; orange; *n* = 14) mice across a wide range of stimulus intensities, from very dim (-4.64 log(cd•s/m^2)) to very bright (2.41 log(cd•s/m^2)). We applied a 60 Hz low-pass filter to remove oscillatory potential (OP) contamination from the ERG a- and b-waves, and a 30-300 Hz Butterworth band-pass filter to isolate OPs for further analysis (**Figure 4.2A**). There was no difference in b-wave amplitude between WT and KO after dim stimuli (**Figure 4.2B and 4.2C**), between -4.64 and -2.43 log(cd•s/m^2). At brighter flash intensities, from -1.64 to 2.41 log(cd•s/m^2), the a-wave was visible and there was no difference in a-wave amplitudes across intensities **(Figure 4.10: Figure Supplement 1)**, indicating that the KO did not affect the rod photoreceptor light responses. Because the ERG b-wave is dependent on upstream photoreceptor activation, which is represented by the a-wave, it is common practice for ERG b-wave amplitudes to be normalized to a-wave amplitudes for comparison across genotypes when the a-wave is present. The TPBG-KO increased the b/a-wave ratio across the range of stimuli intensities (**Figure 4.2E**), indicating a larger and more prolonged RBC light response in TPBG-KO mice.

Oscillatory potentials (OPs) are low amplitude, high frequency waves superimposed over the rising phase of the ERG b-wave and observed after bright stimuli. Previous studies indicate that OPs originate from rhythmic activity in the IPL downstream of the RBC [195]. Because the light response of a dark-adapted retina is primarily rod-driven, OPs can be seen as indirectly correlated to RBC output. We isolated OPs from raw scotopic ERG recordings using a 30-300 Hz Butterworth band-pass filter (**Figure 4.2A**) and measured the trough-to-peak amplitude of the largest wave to compare RBC output between WT and TPBG-KO mice. Because scotopic OPs are driven by RBCs, we normalized the OP amplitude by the b-wave amplitude of the corresponding ERG recording. TPBG-KO OP/b-wave ratios were reduced compared to WT at nearly all stimulus intensities (**Figure 4.2F and G**). TPBG is primarily expressed in RBCs, therefore an effect of TPBG-KO on the OPs is most likely to be due to reduced RBC output onto downstream neurons. See **Figure 4.11: Figure Supplement 2** for a table of the data quantified in **Figure 4.2B**, **D** and **F**.

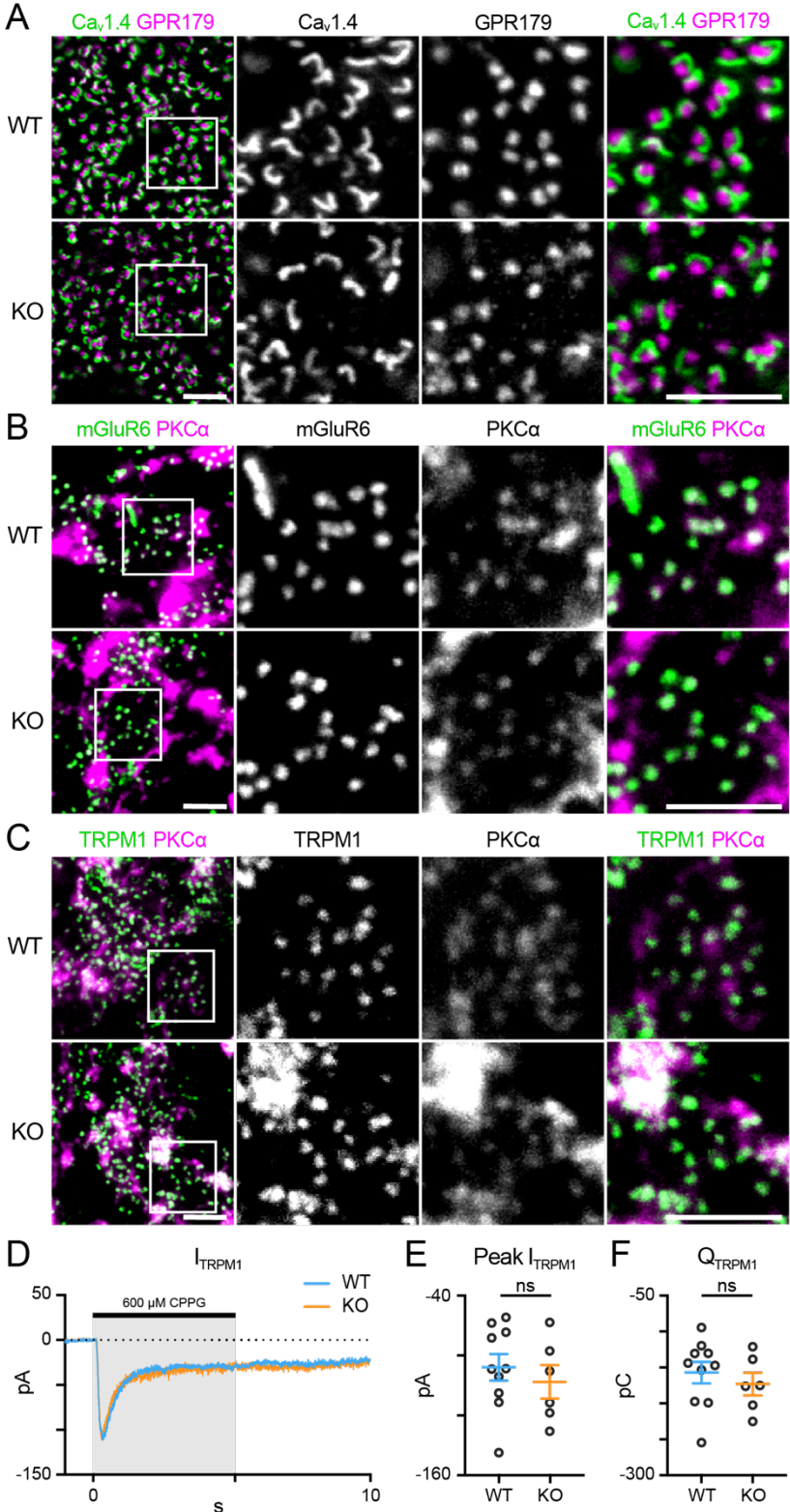*TPBG is not required for synaptic transmission in RBC dendrites*

69

Figure 4.3: TPBG is not required for synaptic transmission in RBC dendrites. **(A-C)** Immunofluorescence confocal microscopy from WT and TPBG-KO whole mount retinas using antibodies against rod and RBC synaptic markers. **(A)** Immunofluorescence labeling of Ca$_v$1.4 (green) and GPR179 (magenta), **(B)** mGluR6 (green) and PKCα (magenta), and **(C)** TRPM1 (green) and PKCα (magenta). Square boxes in the leftmost images indicate regions of interest expanded in the other images. For (**A**), Z-projections of two sections were used with a Z-step distance of 0.297 μm for a total thickness of 0.594 μm. For (**B-C**), Z-projections of ten sections were used for a total thickness of 2.97 μm. All scale bars are 5 μm. **(D-F)** Chemically simulated light responses were recorded at ~33° C in WT (blue; n = 10) and TPBG-KO (KO; orange; n = 6) RBCs following a pulse of 600 µM CPPG for 5 seconds. **(D)** Example CPPG-induced TRPM1 currents. **(E)** Quantification of peak CPPG-induced TRPM1 current (I_{TRPM1}) and **(F)** charge transfer (Q_{TRPM1}) over the five-second duration of the CPPG pulse. Ames medium was supplemented with 4 µM L-AP4. Experiments were performed at ~33° C in 3-month-old mice. Open circles in bar graphs represent single cells and colored bars represent the mean $\pm$ SEM. Statistical significance was determined using Welch's t-tests; ns: $p > 0.05$.

We examined the expression and localization patterns of several critical synaptic proteins that are present in rod photoreceptor axon terminals and RBC dendritic tips and are required for synaptic transmission. RBCs receive input primarily from rod photoreceptors via a sign-inverting signal transduction cascade localized post-synaptically to the distal RBC dendrites. Glutamate released from rod photoreceptors is detected by the group III metabotropic glutamate receptor mGluR6 [40–42,196], which is negatively coupled to the TRPM1 cation channel [43–45,125]. Thus, a light stimulus relieves TRPM1 tonic inhibition, permitting cation influx and subsequent RBC depolarization.

First, we looked at the spatial relationship between presynaptic elements the rod spherule and the invagination of the RBC dendrites (**Figure 4.3A**). We used an antibody against the rod L-type Ca^{2+} channel subunit Ca$_v$1.4 to label the horseshoe-shaped active zone and an antibody that labels GPR179 in RBCs [175]. In normal rod-RBC synapses, GPR179 labeling appears as pairs of puncta (corresponding to two RBC dendrites) within the concavity of the horseshoe-shaped Ca$_v$1.4 immunofluorescence. We observed no difference in immunofluorescence of RBC dendritic tips in relation to the rod active zones between WT (top) and TPBG-KO (KO; bottom) whole mount retinas. Next, we used immunofluorescence double-labeling with PKCα to compare immunofluorescence of the synaptic proteins mGluR6 and TRPM1, both of which are required for signal transduction in RBCs. Because mGluR6 and TRPM1 are expressed in all ON-bipolar cells, co-localization of mGluR6 and TRPM1 puncta with PKCα was indicative of RBC-specific labeling. We observed no difference in mGluR6 (**Figure 4.3B**) or TRPM1 (**Figure 4.3C**) immunofluorescence in WT and TPBG-KO RBCs, indicating that TPBG is not required for the accumulation of the mGluR6-TRPM1 signaling complex in RBC dendrites.

Scotopic ERG recordings to bright stimuli revealed an increased b/a-wave ratio in TPBG-KO mice (Figure 2) indicating an enhanced light response in KO RBCs. Because the RBC light response is initiated by TRPM1, we compared TRPM1 currents between WT (blue; n = 10) and TPBG-KO (KO; orange; n = 6) RBCs by recording chemically simulated light responses in retinal slices in whole-cell voltage-clamp (**Figure 4.3D-F**). In this technique, bath application of the

mGluR6 agonist L-AP4 maintains the retina in a simulated dark-adapted state, and brief puffs of the mGluR6 antagonist, CPPG, onto the dendrites simulates a light flash and evokes TRPM1 currents (**Figure 4.3D**). TPBG-KO did not alter the CPPG-induced TRPM1 peak current (**Figure 4.3E**; WT: -88.24 ± 8.92 pA; KO: -98.04 ± 11.28 pA; Welch's t-test: p = 0.51, $t(10.85)$ = 0.68) or charge transfer (**Figure 4.3F**; WT: -157.10 ± 47.01 pC; KO: -173.10 ± 38.62 pC; Welch's t-test: p = 0.47, $t(12.40)$ = 0.74). These results suggest that TPBG is not required for the formation of functional rod-RBC synapses and that the larger scotopic ERG b/a-wave ratios do not reflect enhanced TRPM1 currents in the TPBG-KO.

TPBG is not required for the formation of RBC synaptic ribbons

Because oscillatory potentials are thought to be generated by the inner retina, and RBCs drive the majority of downstream activity under scotopic conditions, the attenuation of scotopic OPs in the TPBG-KO suggests a deficit in RBC output to third-order neurons. Like rods, RBCs signal to downstream cells using ribbon synapses. A depolarized potential entering the axon terminal prompts the opening of L-type voltage-gated Ca^{2+} channels clustered beneath the ribbons and the resulting influx of Ca^{2+} triggers the fusion (exocytosis) of ribbon-tethered synaptic vesicles [197]. This process requires a close spatial relationship between the Ca^{2+} channels and the docked vesicles near the synaptic ribbons [198]. We used triple immunofluorescence microscopy to examine the relative localization and expression patterns of the L-type Ca^{2+} channel subunit, $Ca_v1.4$, and the synaptic ribbon protein RIBEYE (**Figure 4.4**). Because neither $Ca_v1.4$ nor RIBEYE are specific to RBC axon terminals, we isolated RBC-specific immunofluorescence using a binary mask derived from PKCα immunofluorescence to exclude labeling from other bipolar cells in the IPL. $Ca_v1.4$ and RIBEYE show punctate immunofluorescence in RBC axon terminals and are co-localized or closely apposed. We found no difference between WT and TPBG-KO (KO) $Ca_v1.4$ and RIBEYE immunofluorescence patterns. In both conditions, each RIBEYE punctum was closely associated with a $Ca_v1.4$ punctum, suggesting TPBG is not required for the accumulation of ribbon components in RBC active zones.
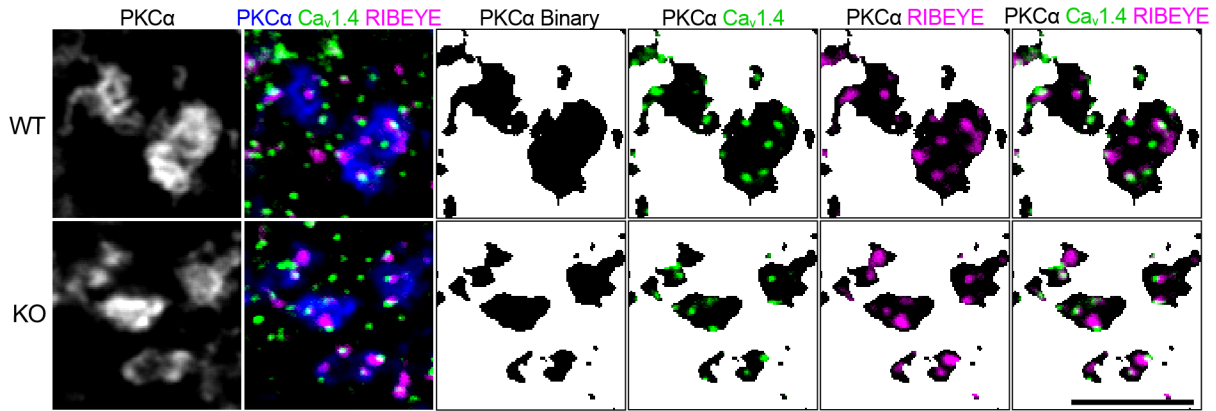
Figure 4.4: TPBG is not required for the co-localization of synaptic proteins in RBC axon terminals. Triple immunofluorescence confocal microscopy of WT and TPBG-KO (KO) whole mount retinas using antibodies against PKCα (blue), Ca$_v$1.4 (Green) and RIBEYE (magenta). To isolate labeling in RBC axon terminals, binary images were created using the PKCα channel and overlayed over the other two channels to generate binary masks. Z-projections of two sections were used with a Z-step distance of 0.297 μm for a total thickness of 0.547 μm. The scale bar is 5 μm.

TPBG is required for efficient exocytosis in RBC synaptic terminals

We did not see any morphological changes in TPBG-KO axon terminals. To examine the effect of TPBG-KO on RBC synaptic output, we recorded time-resolved membrane capacitance (C_m) before and after a depolarizing pulse using the "sine + DC" method [190,191]. High-resolution membrane capacitance changes (ΔC_m) after a depolarizing pulse strongly correlate with vesicle exocytosis in neuroendocrine cells [199,200] and glutamate release from bipolar cell axon terminals [201]. A sinusoidal voltage command (200 Hz at 30 mV trough-to-peak) was superimposed over the holding voltage of -80 mV and exocytosis was evoked by depolarizing the cell to -10 mV to open the L-type voltage-gated Ca^{2+} channels (**Figure 4.5A)**. Membrane capacitance (C_m), membrane resistance (R_m), and series resistance (R_s) were recorded before and after the pulse and ΔC_m was measured as the change in C_m after exocytosis. Changes in R_m and R_s were not correlated with changes in C_m (**Figure 4.5B**).

C_m measurements in RBCs are complicated by the attenuation and filtering of the sinusoidal voltage command amplitude down their narrow axons [191]. We sought to confirm that a low-frequency sinusoidal command reduces attenuation and maximizes RBC C_m changes compared to higher frequencies (**Figure 4.5C-F**) using 200 (n = 6), 400 (n = 4), 800 (n = 4), and 1600 (n = 4) Hz commands. We found no significant difference in the voltage-gated Ca^{2+} current amplitude (I_{Ca}) or charge transfer (Q_{Ca}) across frequencies (not shown), but the ΔC_m (**Figure 4.5C and D**; 200 Hz: 41.94 $\pm$ 4.95 fF; 400 Hz: 19.13 $\pm$ 4.06 fF; 800 Hz: 4.05 $\pm$ 2.91 fF; 1600 Hz: -4.23 $\pm$ 1.40; Brown-Forsythe ANOVA: p < 0.0001, 34.12(2.00, 10.87)) and the resting C_m (**Figure 4.5E and F**; 200 Hz: 5.97 $\pm$ 0.23 pF, 400 Hz: 5.73 $\pm$ 0.12 pF, 800 Hz: 4.81 $\pm$ 0.15 pF, 1600 Hz: 4.04 $\pm$

0.12 pF; Brown-Forsythe ANOVA: p < 0.0001, 25.06(3.00, 11.34)) were greater at 200 Hz compared to higher frequencies. These supplementary results support our decision to examine exocytosis in RBCs using a 200 Hz "sine + DC" protocol.
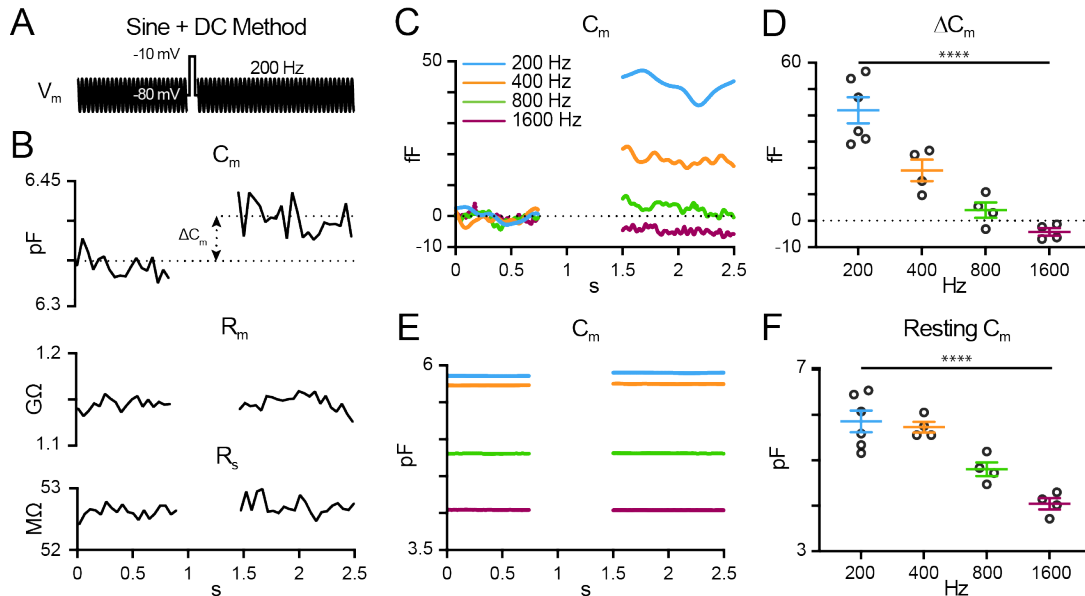

Figure 4.5: Measuring membrane capacitance in RBCs. **(A)** Whole-cell voltage-clamp capacitance recordings were made using the "sine + DC" method. A sinusoidal voltage command (200 Hz at 30 mV trough-to-peak) was superimposed on the holding potential of -80 mV. Membrane capacitance (C_m), membrane resistance (R_m), and series resistance (R_s) were recorded before and after a depolarizing pulse from -80 mV to -10 mV for 100 ms. **(B)** A sample recording from one WT RBC using the sine + DC method as described. The change in membrane capacitance (ΔC_m) was measured as the difference between the C_m before and after the depolarizing pulse. Changes to R_m (middle) and R_s (bottom) were small and do not correlate with changes in C_m. **(C)** Average baseline-subtracted C_m recordings using 200 (blue; *n* = 6), 400 (orange; *n* = 4), 800 (green; *n* = 4), or 1600 (magenta; *n* = 4) Hz sinusoidal voltage commands in WT RBCs. Data for the 200 Hz condition was reused from WT in Figure 4. Traces with higher frequencies were resampled to 200 Hz for ease of comparisons. **(D)** Quantification of ΔC_m. **(E)** Average C_m recordings and **(F)** quantification of resting C_m across frequencies. Resting C_m was measured before the depolarizing pulse. Experiments were conducted at ~33° C in 3-month-old mice. Open circles in bar graphs represent single cells and bars represent the mean ± SEM. Statistical significance was determined using Brown-Forsythe ANOVA tests; ****: *p* < 0.0001.

We use whole-cell voltage-clamp to compare WT (blue; n = 6) and TPBG-KO (KO; orange; n = 7) L-type voltage-gated Ca^{2+} currents and subsequent changes in membrane capacitance to examine RBC synaptic vesicle exocytosis (**Figure 4.6**). Cells where C_m, R_m, and R_s were highly correlated were discarded. The synaptic blockers L-AP4, strychnine, TPMPA, and gabazine were used to block spontaneous activity and help increase and stabilize R_m during recordings. The passive properties of R_m (WT: 1.603 ± 0.24 GΩ; KO: 1.630 ± 0.16 GΩ; Welch's t-test: p = 0.93, t(8.84) = 0.097) and R_s (WT: 50.54 ± 2.33 MΩ; KO: 49.61 ± 1.91 MΩ; Welch's t-test: p = 0.76, t(10.16) = 0.31) were not different between WT and TPBG-KO RBCs. As long as R_m is significantly greater than R_s, ΔC_m should be a faithful approximation of overall exocytosis [190]. With a mean resting C_m of 5.97 pF and a mean R_s of 50.04 MΩ, we can calculate an average voltage-clamp

speed of 298.74 μs – sufficiently fast to clamp the membrane to a 200 Hz sine wave with a 5 ms period.

TPBG-KO had no effect on the voltage-gated Ca^{2+} currents (**Figure 4.6B and C**; WT: -74.99 $\pm$ 4.49 pA, KO: -74.24 $\pm$ 3.41 pA; Welch's *t*-test: p = 0.90, $t(9.73)$ = 0.13) or charge transfer (**Figure 4.6D**; WT: -7.0 $\pm$ 0.38 pC, KO: -6.7 $\pm$ 0.33 pC; Welch's *t*-test: p = 0.57, $t(10.43)$ = 0.58). However, TPBG-KO resulted in a reduction in ΔC_m compared to WT (**Figure 4.6E and F**; WT: 41.94 $\pm$ 4.95 fF, KO: 25.90 $\pm$ 3.91 fF; Welch's *t*-test: p = 0.029, $t(9.95)$ = 2.55), suggesting a decrease in synaptic vesicle exocytosis in the KO. Most interestingly, the efficiency of exocytosis (the ratio of ΔC_m per unit Q_{Ca}) is also reduced in the KO (**Figure 4.6G**; WT: 5.93 $\pm$ 0.50 fF/-pC, KO: 3.76 $\pm$ 0.44 fF/-pC; Welch's *t*-test: p = 0.0077, $t(10.52)$ = 3.28), indicating that TPBG-KO alters the efficiency of RBC vesicle exocytosis without changing L-type voltage-gated Ca^{2+} influx.
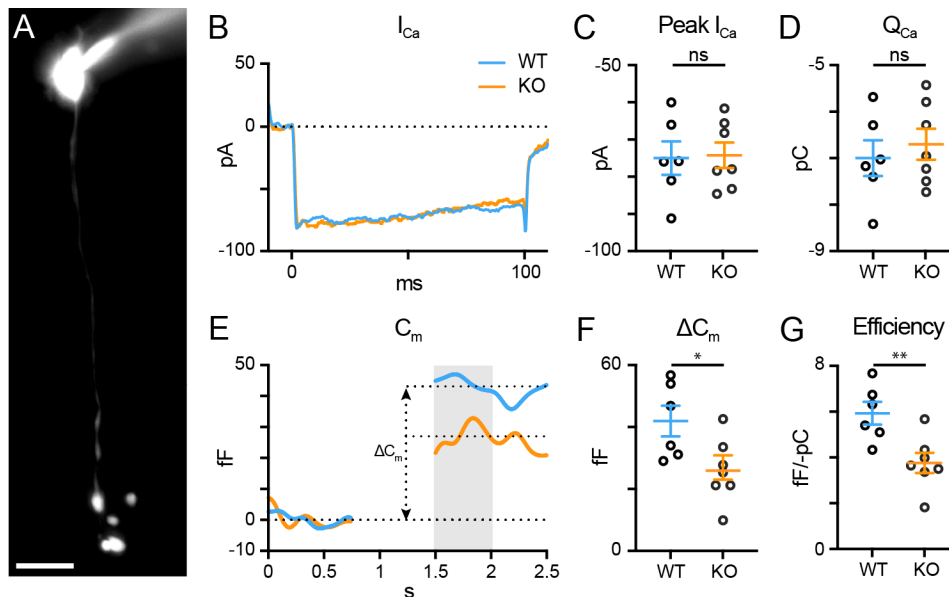
Figure 4.6: TPBG is required for efficient synaptic vesicle release in RBC axon terminals. Whole-cell voltage-clamp recordings were performed at ~33° C in WT (blue; *n* = 6) and TPBG-KO (KO; orange; *n* = 7) RBCs. **(A)** Epifluorescence micrograph of an RBC filled with Alexa Fluor 594 Hydrazide after patch-clamp recording. RBCs were patched and cell type was verified *post-hoc* using epifluorescence microscopy. The scale bar is 10 μm. **(B)** Average L-type voltage-gated Ca^{2+} current traces recorded after a depolarizing pulse from -80 mV to -10 mV for 100 ms. **(C)** Quantification of peak voltage-gated Ca^{2+} current amplitudes (I_{Ca}) and **(D)** charge transfer (Q_{Ca}) over the duration of the pulse. **(E)** Average membrane capacitance (C_m) recordings using a 200 Hz sine + DC protocol. ΔC_m was measured as the difference between baselined resting C_m before and after the depolarizing pulse. Data immediately after the pulse was excluded until C_m stabilized. The gray bar represents the region across which C_m values were averaged. **(F)** Quantification of ΔC_m. **(G)** Quantification of exocytosis efficiency calculated as the absolute value of the change in C_m per unit Q_{Ca}. Ames medium was supplemented with (in µM): 0.5 strychnine, 3 gabazine, 50 TPMPA, and 4 L-AP4. Experiments were conducted at ~33° C in 3-month-old mice. Open circles in bar graphs represent single cells and bars represent the mean $\pm$ SEM. Statistical significance was determined using Welch's *t*-tests; ns: $p > 0.05$; *: $p < 0.05$; **: $p < 0.01$.

TPBG does not alter RBC input resistance or excitability

TPBG-KO amplifies the RBC light response and reduces synaptic vesicle exocytosis, suggesting that TPBG-KO may reduce the gain of RBC synaptic release by shifting RBC excitability. To compare the excitability between WT (blue; *n* = 9) and TPBG-KO (KO; orange; *n* = 11) RBCs, we used current injections (from -80 to 80 pA in 20 pA intervals) in whole-cell current-clamp mode to construct voltage-current relationships and calculate the instantaneous and sustained input resistances (R_{in}). For these experiments, we used the synaptic blockers L-AP4, strychnine, TPMPA, and gabazine to block evoked inputs, thereby isolating RBC-specific voltage responses. **Figure 4.7A** shows similar voltage responses after representative current injections of -80 pA, 0 pA, and +80 pA. The resting membrane potential (V_m) was unchanged in the KO (**Figure 4.7B**; WT: -58.02 ± 4.91 mV, KO: -56.35 ± 4.66 mV; Welch's *t*-test: *p* = 0.81, $t(17.53)$ = 0.25). We found no difference in instantaneous (**Figure 4.7C and D**; WT: 1.31 ± 0.15 GΩ, KO: 1.39 ± 0.09 GΩ; Welch's *t*-test: *p* = 0.64, $t(15.27)$ = 0.48) or sustained R_{in} (**Figure 4.7E and F**; WT: 1.13 ± 0.11 GΩ, KO: 1.05 ± 0.07 GΩ; Welch's *t*-test: *p* = 0.58, $t(14.28)$ = 0.56) between the WT and KO RBCs. These results indicate that a shift in R_{in} and RBC excitability in the TPBG-KO is does not explain the reduced exocytosis. See **Figure 4.12: Figure Supplement 3** for a table of the data quantified in **Figure 4.7C and E**.
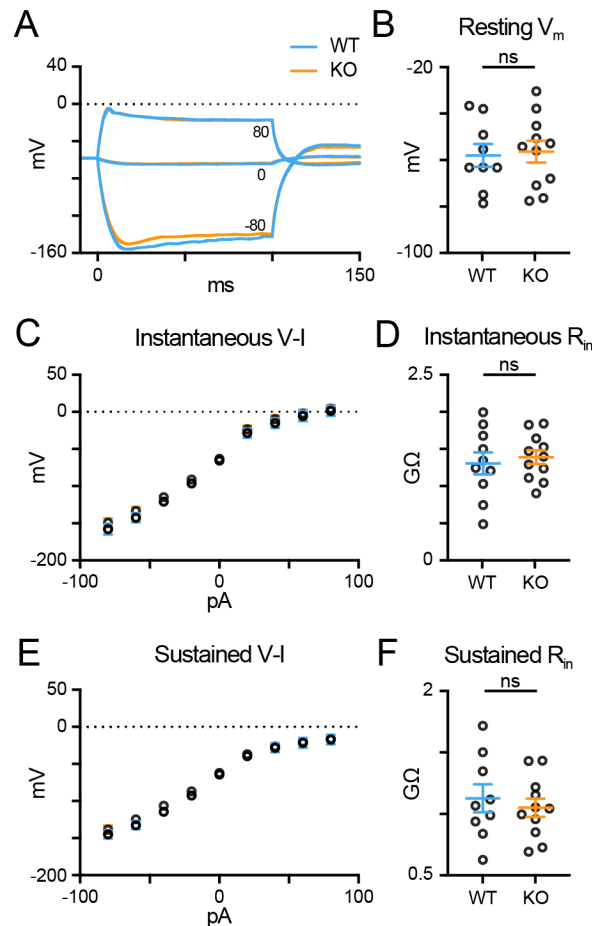
Figure 4.7: TPBG does not alter RBC input resistance or excitability. Whole-cell current-clamp recordings in WT (blue; *n* = 9) and TPBG-KO (KO; orange; *n* = 11) RBCs were used to construct a current-voltage relationship and calculate input resistance (R_{in}). A current injection protocol from -80 pA to 80 pA in 20 pA steps was used with a K-gluconate-based internal solution. **(A)** Average voltage traces following -80 pA, 0 pA, and 80 pA current injections for 100 ms. **(B)** Resting membrane voltages recorded immediately after entering current clamp mode. **(C)** A plot of the voltage-current (V-I) relationship measured at the peak instantaneous voltage during current injections. **(D)** Quantification of instantaneous R_{in}. **(E)** A plot of the sustained V-I relationship measured as the average voltage calculated over the last 10 ms of the current pulse. **(F)** Quantification of the sustained R_{in}. Instantaneous and sustained R_{in} values were calculated by measuring the slope of the linear portion of the V-I curves (from -40 to 40 pA). Ames medium was supplemented with (in µM): 0.5 strychnine, 3 gabazine, 50 TPMPA, and 4 L-AP4. See **Figure 4.12: Figure Supplement 3** for a table of data used in **C** and **E**. Experiments were conducted at ~33° C in 3-month-old mice. For V-I curves, open circles represent the mean and error bars represent SEM. For quantification, open circles represent single cells and bars represent the mean ± SEM. Statistical significance was determined using Welch's *t*-tests; ns: *p* > 0.05.

TPBG-KO reduces reciprocal inhibitory feedback

RBCs drive retinal output via glutamate release into the IPL, which stimulates Ca^{2+}-permeable AMPA receptors in downstream AII amacrine cells (AII-ACs). RBC glutamate release is also detected by A17 amacrine cells (A17-ACs), which when depolarized, release GABA back onto RBC synaptic terminals where it is sensed by $GABA_A$ and $GABA_{A\rho}$ (also called $GABA_C$) Cl⁻ channels (**Figure 4.8A**). An influx of Cl⁻ into the axon terminal through open GABA channels

provides delayed inhibitory feedback by hyperpolarizing the RBC and shaping further RBC glutamate release [59,60,62,202–204]. Each RBC forms a dyad synapse with one AII-AC and one A17-AC [205–208]. As A17-mediated reciprocal feedback is driven by RBC glutamate release, inhibitory feedback currents from A17-ACs are an indirect measure of synaptic vesicle release from RBCs and can help confirm that exocytosis is reduced in the TPBG-KO.
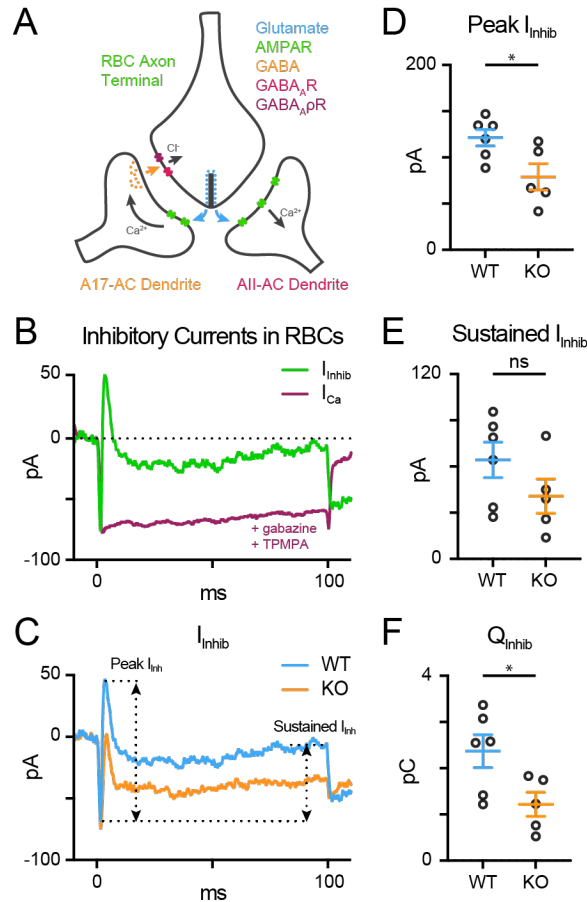
Figure 4.8: TPBG-KO reduces reciprocal inhibitory feedback. **(A)** The dyad synapse arrangement between one RBC, one AII-AC, and one A17-AC in the IPL. Glutamate release by RBCs is detected by Ca^{2+}-permeable AMPA receptors (AMPARs) in AII-AC and A17-AC dendrites. A17-ACs then release GABA back into the IPL which is sensed by $GABA_A$ receptors ($GABA_A$Rs) and $GABA_A\rho$ receptors ($GABA_A\rho$Rs) in the RBC axon terminals. Inhibitory currents are superimposed over L-type voltage-gated Ca^{2+} currents. **(B)** Reciprocal feedback in RBCs was evoked with a 100 ms depolarizing pulse from -80 mV to -10 mV. In the absence of GABA receptor blockers, this depolarizing pulse elicits an inward L-type voltage-gated Ca^{2+} current that is quickly subsumed by outward inhibitory currents (I_{Inhib}; green). These outward currents are abolished by the application of the GABA receptor blockers gabazine and TPMPA (I_{Ca}; magenta). **(C)** Average whole-cell patch-clamp recordings from WT (blue; *n* = 6) and TPBG-KO (KO; orange; *n* = 5) RBCs to compare reciprocal inhibitory feedback after a depolarizing pulse from -80 mV to -10 mV for 100 ms. Current amplitudes and charge transfers were measured from a baseline set to the maximum inward current following depolarization (exemplified by the horizontal dotted line), which was very similar to the L-type voltage-gated Ca^{2+} currents recorded in Figure 5. **(C)** Quantification of peak inhibitory current measured from baseline. **(D)** Quantification of the sustained inhibitory current measured from baseline to the average current over the last 10 ms of the depolarizing pulse. **(E)** Quantification of the charge transfer measured from baseline over the duration of the 100 ms stimulus. Ames medium was supplemented with 0.5 µM strychnine and 4 µM L-AP4. Experiments were performed at ~33° C in 3-month-old mice. Open circles in bar graphs represent single cells and bars represent the mean ± SEM. Statistical significance was determined using Welch's *t*-tests; ns: *p* > 0.05; *: *p* < 0.05.

To test the hypothesis that reduced RBC glutamate release results in smaller inhibitory currents in the TPBG-KO, we used whole-cell voltage-clamp to examine the reciprocal feedback response to a depolarizing pulse from -80 mV to -10 mV for 100 ms in WT (blue; $n = 6$) and TPBG-KO (KO; orange; $n = 5$) RBCs. L-AP4 was used to block spontaneous excitatory inputs and strychnine was used to block glycinergic inhibition. In the absence of GABA receptor blockers, two outward currents can be seen superimposed on the evoked L-type voltage gated Ca^{2+} current (**Figure 4.8B**): a large, fast-activating, fast-inactivating current (labeled Peak I_{Inhib}) and a smaller slowly-activating, non-inactivating current (labeled Sustained I_{Inhib}). Since these two currents likely have different sources, we quantified their amplitudes separately. We found that TPBG-KO reduced the peak inhibitory feedback current (**Figure 4.8C and D**; WT: 121.20 ± 8.83 pA; KO: 78.83 ± 14.23 pA; Welch's t-test: p = 0.04, t(6.92) = 2.52) but not the sustained current (**Figure 4.8C and E**; WT: 64.22 ± 11.52 pA; KO: 40.74 ± 11.16; Welch's t-test: p = 0.18, t(8.94) = 1.46). Lastly, the charge transfer across the duration of the stimulus was also reduced in the TPBG-KO compared to WT (**Figure 4.8F**; WT: 2.37 ± 0.36 pC; KO: 1.22 ± 0.26 pC; Welch's t-test: p = 0.029, t(8.66) = 2.61). Since This supports our previous result that the TPBG-KO suppresses RBC vesicle exocytosis and glutamate release (see **Figure 4.6F**).

It is possible that reciprocal feedback is altered in TPBG-KO due to disrupted expression or clustering of GABA receptors in RBC axon terminals. RBCs express both GABA$_A\alpha$1 and GABA$_A\rho$1 subunits in their axon terminals [209,210]. To see whether TPBG-KO alters GABA receptor expression patterns, we used double immunofluorescence labeling of WT and TPBG-KO whole mount retinas using an antibody against PKCα and antibodies against GABA$_A\alpha$1 and GABA$_A\rho$1 receptor subunits (**Figure 4.9**). As previously, we isolated RBC axon terminal-specific labeling using a binary mask derived from PKCα immunofluorescence. We did not observe any major differences in immunofluorescence between WT (top) and TPBG-KO (KO; bottom) retinas labeled against either GABA$_A\alpha$1 (**Figure 4.9A**) or GABA$_A\rho$1 (**Figure 4.9B**), indicating that impaired GABA receptor expression is likely not reducing inhibitory feedback. This data supports our conclusion that TPBG is required for efficient synaptic vesicle release and glutamate release from RBC axon terminals.
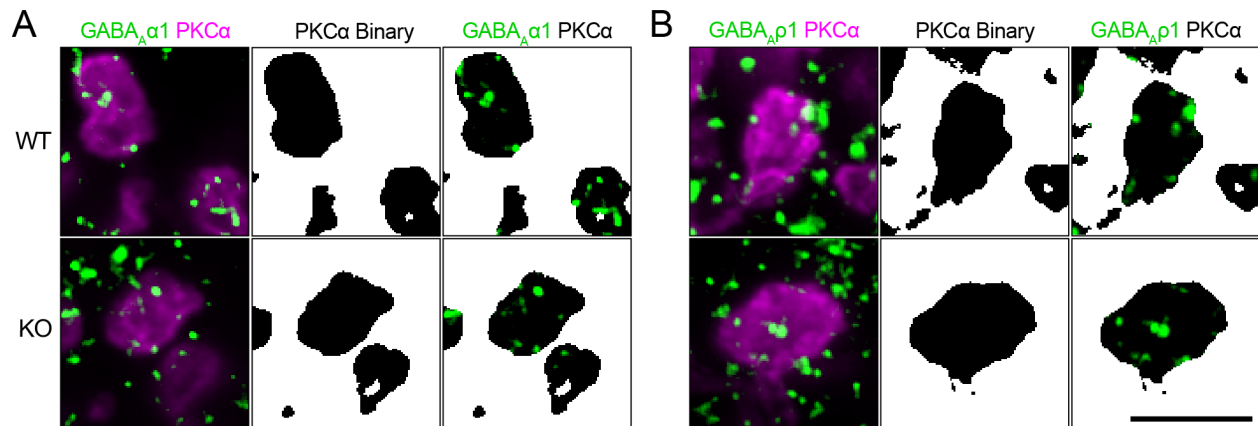
Figure 4.9: TPBG is not required for localization of GABA receptor immunofluorescence. Immunofluorescence confocal microscopy of WT and TPBG-KO (KO) whole mount retinas using an antibody against PKCα (magenta) and antibodies against either the GABA$_A$α1 subunit (**A**; green) or the GABA$_A$ρ1 subunit (**B**; green). To isolate labeling in RBC axon terminals, binaries were created using the PKCα channel and overlayed over the other channels to generate binary masks. For all images, Z-projections of two sections were used with a Z-step distance of 0.297 μm for a total thickness of 0.547 μm. Scale bar is 5 μm.

Discussion

In this study, we characterized the functional consequences of genetic knockout of TPBG in the mouse retina using immunofluorescence and electrophysiological approaches. TPBG-KO did not alter gross RBC morphology in the OPL or IPL as PKCα-labeled RBC dendrites and axon terminals appear normal in both conditions. Because TPBG is localized to both the dendrites and axon terminals of RBCs [186], we sought to examine the effect of TPBG-KO on the RBC synaptic development and physiology in both compartments. We found that dendritic TRPM1 currents activated by CPPG did not change in the TPBG-KO. However, the scotopic OP responses were reduced, suggesting changes in RBC ribbon synapse function. Accordingly, time-resolved C_m measurements and whole-cell recording indicate that glutamate exocytosis and GABAergic feedback are reduced at TPBG-KO RBC synapses. Importantly, we did not detect differences in presynaptic L-type Ca^{2+} current amplitude or changes in Ca^{2+} channel, GABA receptor, or RIBEYE expression and localization. We propose that TPBG plays an important role in fine tuning the synaptic architecture of RBC ribbon synapses to increase exocytosis efficiency.

TPBG and RBC dendrites

We found that TPBG is not required for the normal insertion of RBC dendritic tips inside rod spherules or for normal depolarizing currents through TRPM1 cation channels. Our immunofluorescence and electrophysiological examination of RBC dendrites suggest that TPBG is not essential for basic synaptic function in that compartment. That being said, TPBG

immunofluorescence reveals that large amounts of TPBG are present in RBC dendrites, suggesting some role in dendritic development or function.

TPBG regulates dendritic arborization in mouse olfactory bulb granule cells [165]. TPBG-KO reduced dendritic branching and dendritic migration to synaptic targets. Lentiviral overexpression of TPBG increased dendritic branching complexity and restored dendritic arborization deficits induced by nasal occlusion. In the retina, TPBG may also regulate RBC dendritic branching complexity in the OPL. TPBG is a known regulator of Wnt signaling [170,211], which is required for functional synaptic targeting and OPL lamination in RBCs, therefore TPBG may promote RBC dendritic development through control of the Wnt pathway [212]. We didn't detect a structural or physiological phenotype in RBC dendrites, but thorough evaluation of RBC dendritic maturation and branching using sparse labeling techniques might reveal a more subtle effect of TPBG-KO on dendritic architecture.

TPBG and RBC synaptic vesicle exocytosis

We found a reduction in the OP/b-wave ratios isolated from scotopic ERG recordings in TPBG-KO mice, which we interpret as evidence for decreased RBC output to third-order neurons. While the specific cell types that contribute to OP generation are unknown, it is generally accepted that OPs stem from rhythmic activity in the IPL [213]. Early studies implicated interactions between bipolar cell axon terminals, amacrine cell processes, and ganglion cell dendrites as potential generators of the OPs [195]. Intravitreal injections of glycine into rabbit retinas resulted in morphological changes in many ACs and disappearance of the OPs from the ERG [214] while application of neurotoxic kainate to ganglion cell dendrites diminishes OP amplitude [215]. A more recent study unequivocally implicates multiple distinct generators in the production of early, intermediate, and late OP peaks [216]. The use of APB and CNQX to block synaptic inputs to ON and OFF-bipolar cells significantly diminished intermediate and later OPs but left early OPs intact, suggesting that early OPs are generated by photoreceptors. Intermediate and late OPs have differential sensitivity to tetrodotoxin, which abolished only late OPs, indicating that intermediate OPs are generated by action-potential-independent interactions and late OPs are generated by action-potential-dependent ones [216]. Our OP data shows a much larger attenuation of TPBG-KO OP amplitude in intermediate and late OPs compared to early ones. Thus, the results of these studies support our conclusion that reduced scotopic OP/b-wave ratios are likely due to suppressed rhythmic activity of third-order neurons due to reduced RBC glutamate release.

By simultaneously recording the presynaptic L-type voltage-gated Ca^{2+} currents and subsequent membrane capacitance changes evoked by RBC depolarization, we showed that

TPBG-KO reduced exocytosis compared to WT RBCs despite no change in presynaptic Ca^{2+} currents, indicating reduced exocytosis efficiency in the KO. Exocytosis efficiency is calculated as the exocytosis per unit Ca^{2+} charge transfer. We calculated an exocytosis efficiency of approximately 6 fF/pC (**Figure 4.6G**) in adult mouse RBCs after a 100 ms depolarizing pulse at 33° C. In adult vertebrate auditory hair cells, which also form ribbon synapses, similar exocytosis efficiencies of 5 to 6 fF/pC have been reported after 100 ms pulses [188,217]. Like bipolar cells, hair cell ribbon synapses operate via nanodomain coupling between Ca^{2+} channels and docked vesicles [198]. However, exocytosis efficiency usually increases with shorter depolarizing pulses and can be as high as 16 to 20 fF/pC at immature calyx of Held axon terminals after a 1 ms pulse. The calyx of Held axon terminals contain conventional active zones, not synaptic ribbons, and operate via Ca^{2+} microdomains where Ca^{2+} influx and vesicle exocytosis are less tightly coupled [218]. Further studies will be required to verify the relationship between TPBG and nanodomain coupling at RBC ribbon synapses.

TPBG and synaptic ribbon proteins

Neurotransmitter release from synaptic ribbons can be simplified into three major steps: synaptic docking, Ca^{2+} influx and its detection by Ca^{2+} sensors, and Ca^{2+}-dependent fusion of synaptic vesicles with the presynaptic membrane [12,187]. These are all potential points at which TPBG may be supporting efficient vesicle release from RBCs. Synaptic ribbons are primarily composed of the scaffold protein RIBEYE and are anchored to the presynaptic active zone by a number of cytoskeletal anchoring proteins, including Bassoon and Piccolo [219]. We did not observe a difference in RIBEYE immunofluorescence in WT and TPBG-KO axon terminals, but immunofluorescence does not confirm the correct localization or orientation of the ribbon at the active zone. If TPBG is required for correct localization of the ribbon, exocytosis efficiency may be significantly disrupted in KO RBCs. Vesicle accumulation and transport in RBC synaptic terminals is dependent on F-actin polymerization and is regulated by PKCα [78–82]. We originally identified TPBG as a PKCα-dependent phosphoprotein [168]; thus, it is possible that PKCα controls vesicle docking via actin dynamics in RBC axon terminals through TPBG.

The tight temporal control of vesicle release that is a trademark of synaptic ribbons requires nanodomain-coupling between the L-type channels and Ca^{2+} binding proteins that trigger synaptic vesicle fusion [192,198,220]. $Ca_v1.4$ and RIBEYE appear co-localized by immunofluorescence in both WT and TPBG-KO RBC axon terminals, but a small disruption of this tight coupling might not be detected with immunofluorescence and could have a large effect on glutamate release by slowing the accumulation of Ca^{2+} at the sensor. Nanodomain-coupling likely depends on a close

spatial relationship between the L-type channels and the vesicle release machinery, yet it is not fully known how this clustering is achieved in RBCs. It is possible that TPBG is required for L-type channels clustering such that in its absence, normal nanodomain-coupling is disrupted, Ca^{2+} detection by the ribbon is delayed, and synaptic vesicle fusion is reduced.

Lastly, TPBG could be involved in the mechanics of synaptic vesicle fusion. Vesicle fusion in RBC synapses is accomplished by Ca^{2+}-sensitive synaptotagmins and a complex of three SNARE proteins: synaptobrevin, SNAP-25, and syntaxin 3. Synaptobrevin is an integral membrane protein of the synaptic vesicles, but SNAP-25 and syntaxin 3 are localized to the presynaptic membrane [187,221]. Other proteins implicated in vesicle priming and fusion at ribbon synapses are RIM1, Munc13, and CAPS proteins [188]. These proteins are critical for vesicle fusion and TPBG could interact with them to regulate vesicle exocytosis from RBC synapses.

TPBG and RBC excitability

The responses of a neuron to synaptic input depend on the intrinsic properties of the cell [222]. We found evidence that the TPBG-KO increases the RBC light response while simultaneously reducing synaptic vesicle release, suggesting that the excitability of RBCs could be suppressed in the KO. The excitability of a cell depends on its complement of voltage-gated ion channels and is experimentally determined by comparing the voltage responses to different current injections. In RBCs, instantaneous voltage responses are predominately driven by voltage-gated Ca^{2+} currents which are quickly counteracted by sustained voltage-gated K^+ and HCN channels. Hyperpolarizing voltage-gated K^+ channels open at depolarizing potentials while depolarizing HCN channels open at hyperpolarizing potentials. The competing input from these channels controls both the resting V_m and cell excitability. However, the resting membrane potential and input resistances were unchanged in TPBG-KO RBCs, suggesting that altered excitability is not the mechanism by which the TPBG-KO increases the RBC light response or suppresses RBC output.

TPBG and reciprocal feedback inhibition

To confirm that the TPBG-KO reduces RBC vesicle fusion and glutamate release, we compared GABAergic feedback inhibition between WT and TPBG-KO RBCs. We found attenuation of peak inhibitory currents and inhibitory charge transfer in the TPBG-KO, but no change in sustained inhibitory currents. With glycinergic inhibition blocked by strychnine, the primary remaining source of feedback inhibition in RBCs is A17-mediated GABAergic reciprocal feedback. GABA released from A17-ACs is sensed by two kinetically distinct ionotropic GABA

receptors in RBC axon terminals: $GABA_A$ and $GABA_A\rho$ [209]. $GABA_A$ receptor-mediated current is rapidly-activating, while $GABA_A\rho$-mediated current is slowly-activating [223]. We detected two different inhibitory components: a large, quickly-inactivating current and a smaller, sustained one. Though we did not pharmacologically isolate each current, the kinetics of the inhibitory currents suggest that Peak I_{Inhib} is likely mediated by $GABA_A$ receptors and Sustained I_{Inhib} is likely mediated by $GABA_A\rho$ receptors.

GABAergic reciprocal feedback from A17-ACs might be altered if GABA receptor expression or localization was disrupted by TPBG-KO. $GABA_A$ receptors are large pentameric ion channels usually containing α, β, and γ subunits. Early work indicates that RBC axon terminals express $GABA_A\alpha1$, $\alpha3$, and $\gamma2$ receptor subunits [209], but a recent study found that the $\alpha1$ subunit dominates in adult mice [224]. $GABA_A\rho$ receptors contain only ρ subunits [209]. Therefore, we used antibodies against $GABA_A\alpha1$ and $GABA_A\rho1$ to visualize $GABA_A$ and $GABA_A\rho$ receptor localization and an antibody against $PKC\alpha$ to isolate RBC-specific axon terminals. We did not detect any difference in GABA receptor immunofluorescence in RBC axon terminals between WT and TPBG-KO, indicating that reduced GABAergic feedback is likely not due to disrupted GABA receptor localization.

We found that TPBG-KO increased scotopic ERG b/a-wave ratios recorded from TPBG-KO mice. The scotopic ERG b-wave reflects the depolarization of RBCs initiated by current through TRPM1 non-specific cation channels. Yet, we did not find any difference in CPPG-induced TRPM1 currents between WT and TPBG-KO retinas. Interestingly, pharmacological studies show that blocking inhibitory currents from third-order neurons shapes the scotopic b-wave. In particular, injections of the $GABA_A$ antagonist bicuculline or the $GABA_A\rho$ antagonist TPMPA into the IPL significantly increases the amplitude and duration of the scotopic b-wave [225,226], suggesting that GABAergic feedback from A17-ACs contributes to the shape of the RBC light response. These studies support the conclusion that our enlarged RBC light response is due to reduced reciprocal feedback secondary to reduced RBC glutamate release in the TPBG-KO.

Summary

In conclusion, our findings show that genetic deletion of TPBG attenuates scotopic ERG oscillatory potentials, synaptic vesicle exocytosis, and reciprocal feedback in RBCs. We propose that TPBG is essential for the development or function of ribbon synapses. Further evaluation of TPBG is critical for producing a more comprehensive understanding of its role in fine-tuning RBC synaptic physiology.

Figure Supplements
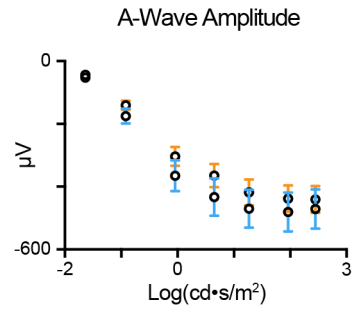
A-Wave Amplitude

Figure 4.10: Figure Supplement 1: TPBG-KO does not alter the scotopic ERG a-wave. Quantification of a-wave amplitudes recorded after bright stimuli. A-waves are measured from baseline to the a-wave trough. Experiments were performed in 3-6-month-old anesthetized mice. Data is presented as the mean ± SEM.

A

Log(cd•s/m^2)	B-Wave (mV)	t-Test (p)
-4.64	WT: 20.83 ± 2.70 KO: 27.63 ± 3.19	0.11 (ns)
-3.93	80.24 ± 16.04 74.29 ± 8.57	0.75 (ns)
-3.06	253.35 ± 46.15 238.59 ± 26.85	0.78 (ns)
-2.74	324.00 ± 39.74 323.40 ± 35.84	0.99 (ns)
-2.43	428.33 ± 52.82 427.48 ± 47.72	0.99 (ns)
-1.85	548.84 ± 66.27 549.76 ± 58.06	0.99 (ns)

B

Log(cd•s/m^2)	B/A-Wave Ratio	t-Test (p)	OP/B-Wave Ratio	t-Test (p)
-1.64	WT: 8.94 ± 0.650 KO: 13.33 ± 1.310	0.0075 **	WT: 0.23 ± 0.037 KO: 0.13 ± 0.028	0.049 *
-0.93	2.60 ± 0.400 4.14 ± 0.330	0.0074 **	0.32 ± 0.046 0.22 ± 0.032	0.11 (ns)
-0.06	2.11 ± 0.048 2.46 ± 0.110	0.0069 **	0.35 ± 0.030 0.25 ± 0.028	0.020 *
0.63	1.81 ± 0.040 2.03 ± 0.064	0.0074 **	0.36 ± 0.033 0.26 ± 0.029	0.0276 *
1.24	1.65 ± 0.074 1.84 ± 0.056	0.049 *	0.39 ± 0.034 0.27 ± 0.025	0.0104 *
1.93	1.58 ± 0.060 1.76 ± 0.056	0.040 *	0.41 ± 0.032 0.28 ± 0.024	0.0033 **
2.41	1.53 ± 0.051 1.66 ± 0.056	0.09 (ns)	0.38 ± 0.023 0.27 ± 0.023	0.0031 **

Figure 4.11: Figure Supplement 2: TPBG-KO alters the scotopic ERG after bright stimuli. (A) Full dataset of dim b-wave amplitudes and p-values used in Figure 2B for all dim stimuli. (B) Full dataset of b/a-wave ratios and OP/b-wave ratios used in Figures 2D and F including p-values for all bright stimuli. Experiments were performed in 3-6-month-old anesthetized mice. Data is presented as mean ± SEM. Statistical significance was determined using Welch's t-tests; ns: p > 0.05; *: p < 0.05; **: p < 0.01.

Current (pA)	Instantaneous Voltage (mV)	t-test (p)	Current (pA)	Sustained Voltage (mV)	t-test (p)
A			**B**		
-80	WT: -100.06 ± 7.07 KO: -92.84 ± 5.91	0.44 (ns)	-80	WT: -86.78 ± 5.76 KO: -82.16 ± 5.38	0.57 (ns)
-60	-84.49 ± 6.10 -77.11 ± 5.29	0.37 (ns)	-60	-74.51 ± 5.29 -68.31 ± 4.17	0.37 (ns)
-40	-62.91 ± -4.59 -58.47 ± 4.28	0.49 (ns)	-40	-56.37 ± 3.97 -49.97 ± 3.49	0.24 (ns)
-20	-38.24 ± 2.98 -35.73 ± 3.25	0.44 (ns)	-20	-34.64 ± 2.63 -30.59 ± 2.51	0.28 (ns)
0	-7.49 ± 1.11 -6.83 ± 0.63	0.62 (ns)	0	-6.27 ± 0.91 -5.74 ± 0.55	0.63 (ns)
20	29.64 ± 6.26 32.93 ± 4.94	0.69 (ns)	20	18.44 ± 4.35 19.39 ± 3.47	0.87 (ns)
40	42.83 ± 6.47 46.74 ± 5.05	0.64 (ns)	40	29.75 ± 6.17 30.06 ± 4.59	0.97 (ns)
60	52.54 ± 6.88 54.11 ± 4.99	0.86 (ns)	60	36.46 ± 6.75 36.30 ± 4.62	0.98 (ns)
80	59.47 ± 6.66 60.58 ± 5.05	0.90 (ns)	80	40.93 ± 6.65 40.28 ± 4.72	0.94 (ns)

Figure 4.12: Figure Supplement 3: TPBG does not alter the voltage-current relationship in RBCs. **(A)** Full dataset used to plot the instantaneous V-I curve in **Figure 6C** and the corresponding *p*-values. **(B)** Full dataset used to plot the sustained V-I curve in **Figure 6E** and the corresponding *p*-values. Experiments were conducted at ~33° C in 3-month-old mice. Data is presented as mean ± SEM. Statistical significance was determined using Welch's *t*-tests; ns: $p > 0.05$.

Chapter 5: Discussion and Future Directions

Summary

This thesis describes the characterization of trophoblast glycoprotein (TPBG), a novel transmembrane protein in the mouse retina. Chapter 1 introduces the neural organization of the retina generally and the rod pathway specifically with an emphasis on the synaptic proteins involved in signal transduction between rods, rod bipolar cells (RBCs), and downstream amacrine cells (A17-ACs and AII-ACs). Chapter 1 also touches on the diverse morphological, developmental, and synaptic functions of leucine rich repeat (LRR) proteins in the retina which share structural similarities with TPBG. Chapter 2, published in the Journal of Proteomics [168], describes the TMT-based proteomics screen we used to identify TPBG as a protein with potentially significant implications for RBC function and PKCα-dependent RBC modulation. Chapter 3, published in the Journal of Comparative Neurology [186], presents an immunofluorescence and immunoblot examination of the localization and expression patterns of TPBG in the developing and adult retina. Lastly, Chapter 4 is an unpublished investigation of the function of TPBG in RBCs by exploring the consequences of TPBG knockout using immunofluorescence and electrophysiological techniques. Although the work presented in this dissertation establishes a solid foundation for understanding TPBG in the retina, there are many remaining questions that must be addressed to unravel roles of TPBG. This final chapter addresses several of the potential directions for examination of TPBG in future studies.

Future Directions

TPBG binding partners

One important way to determine TPBG's role in RBC physiology is to identify its binding partners. TPBG contains two potential protein binding domains: the extracellular N-terminal LRR domain and the intracellular C-terminal PDZ-interacting domain, each of which may participate in separate mechanisms. We performed several preliminary co-immunoprecipitation-based unbiased proteomics screens to identify TPBG binding partners. First, we used the OHSU Proteomics Core to identify proteins that precipitated with TPBG in WT mouse retinal lysates. The sample was enriched with TPBG as well as a few potentially interesting binding partners, including BASP1 (Brain Acid Soluble Protein 1, also called NAP-22 and CAP-23).

Next, we performed the same experiment with WT and TPBG-KO retina lysate preparations and we used two TPBG antibodies: one against the extracellular domain (TPBG-NT) and one against the intracellular domain (TPBG-CT). Because antibody binding to a specific region of TPBG may preclude interactions at the antibody binding sites, we anticipated that an N-

terminal antibody would be more likely to precipitate C-terminal binding partners and a C-terminal antibody would be more likely to precipitate N-terminal binding partners. TPBG was strongly enriched in the WT samples from both antibodies and, as expected, absent in the TPBG-KO samples. Once again, BASP1 co-precipitated with TPBG using the TPBG-NT antibody, suggesting possible interactions between the two proteins at the TPBG C-terminal binding site.

Like TPBG, BASP1 shows robust expression during development but reduced expression in most adult tissues. In developing neurons, BASP1 is enriched in axonal growth cones [227] where it regulates cytoskeletal dynamics [228]. In adult neocortical and hippocampal neurons, BASP1 is localized to the presynaptic membrane and on synaptic vesicles where it interacts with dynamin [229], synaptojanin-1 [230], and caspase-3 [231] – three proteins required for synaptic vesicle cycling and trafficking. BASP1 may be an important mediator of TPBG function in RBCs and probing interactions between BASP1 and TPBG could illuminate a mechanism by which TPBG regulates RBC synaptic physiology. This potential connection will be explored further by the Morgans lab in the future.

There are several ways to improve the reliability and increase the success of unbiased co-immunoprecipitation-based proteomics experiments. First, because TPBG is a transmembrane protein, membrane fractionation can be used to significantly enrich for TPBG and its potential binding partners. Membrane fractionation takes advantage of the fact that transmembrane proteins contain hydrophobic regions and can be separated from hydrophilic cytosolic proteins using detergents. Sucrose gradients can be used to isolate synaptic plasma membrane fractions. Because RBCs extend processes across the retina, a split retina preparation could be used to isolate RBC dendrites from axon terminals to study each compartment separately.

The probability that binding partners co-precipitate with TPBG depends on the strength of both the binding interactions, which may be weak or transient, as well as properties of the detergents used to solubilize the cellular contents. Crosslinking can significantly increase the likelihood that binding partners precipitate with TPBG. Crosslinking agents stabilize protein interactions by covalently linking bound proteins together. The crosslinking agents DSP and DTSSP can be used to probe TPBG's extracellular and intracellular binding partners. DSP is lipophilic and membrane-permeable and can be used to crosslink the intracellular C-terminal binding partners of TPBG. DTSSP is hydrophilic and will only crosslink extracellular cell surface proteins; thus, it can be used to crosslink extracellular N-terminal binding partners of TPBG.

Lastly, the technology and techniques available for proteomics screens have improved significantly even in the last few years. Our previous experiments were biased against membrane proteins for two reasons; first: hydrophobic transmembrane regions lack charged lysine and

arginine residues required for cleavage by trypsin, and second: the peptides derived from transmembrane regions are not very soluble in urea. Both issues reduce the ability to detect transmembrane proteins. A new technique called S-trap digestion allows for the use of SDS, a much stronger detergent, to solubilize peptides for chromatographic separation [232]. Also, the new generation of LCMS/MS machines are much better at detecting low-abundance peptides [233]. Combined, these techniques will significantly increase the ability to detect TPBG binding partners using proteomics.

TPBG binding partners may depend on its phosphorylation state. Our proteomics data suggests that TPBG's C-terminal PDZ-interacting motif contains two serine residues that may be phosphorylated under certain circumstances. Phosphorylation of PDZ-interacting domains typically prevents protein interactions [152], so phosphorylation of C-terminal TPBG may regulate interactions with intracellular proteins. To test the phosphorylation-dependence of TPBG interactions, the previously described co-immunoprecipitation screens could be performed using PMA-treated WT and PKCα-KO retinas. PMA treatment increased the rate of TPBG phosphorylation more than 13-fold in WT compared to PKCα-KO [168]. If phosphorylation regulates C-terminal interactions, we would expect to see different proteins co-precipitating from the WT and PKCα-KO tissue. We could also acutely manipulate the activity of PKCα in WT retinas, and therefore potentially the subsequent phosphorylation state of TPBG, pharmacologically. For example, WT retinas could be treated with either PMA or the PKCα inhibitor, Bis-1, before co-immunoprecipitation. This technique would eliminate any potential developmental compensation present in the PKCα-KO.

The relationship between PKCα and TPBG

In Chapter 2, we identified TPBG as a novel PKCα-dependent phosphoprotein in the mouse retina, but our results did not establish the nature of the relationship between the two proteins. Two different TPBG phosphopeptide species derived from its C-terminal intracellular tail were significantly more likely to be phosphorylated in wild type retinas than in PKCα knockout retinas: LTNLS**S**N**S**DV and LTNLSSN**S**DV [168]. However, TPBG may not be a direct phosphorylation target of PKCα, as it is possible that these serine residues may instead be phosphorylated by a different kinase whose activity is regulated by PKCα. As we previously pointed out, the C-terminal tail of TPBG does not conform to the PKCα consensus sequence RRX**S**X(R/K)R (from Kinase.net) where the positively charged flanking arginine and lysine residues are thought to be important for targeting [234]. Evidence suggests, however, that linear amino acid sequence is less important than tertiary structure in determining the likelihood of

phosphorylation by PKCα, as some known PKCα substrates show considerable deviation from the consensus phosphorylation site [134]. The C-terminal tail of TPBG is expected to be flexible and it is possible that this allows the phosphorylated serine residues (S422 and S424) to be brought close to upstream lysine and arginine residues (R384, K385, K388, and K389) to form a PKCα consensus sequence [168].

A kinase assay can be used to determine whether PKCα directly phosphorylates the C-terminal tail of TPBG. A kinase assay takes advantage of ATP as a source of phosphate used for protein phosphorylation and can measure the rate of ADP accumulation as phosphorylation by PKCα progresses. If PKCα directly phosphorylates TPBG, the accumulation of ADP when PKCα is mixed with a C-terminal TPBG peptide should be significantly greater than that when PKCα is combined with a scrambled peptide control. A good negative control for this experiment would be the introduction of the TPBG peptide but with both serine residues replaced with alanine residues. Alanine residues have a similar size as serine residues but cannot be phosphorylated by serine/threonine kinases like PKCα. Thus, the inclusion of alanine residues should not stimulate the production of ADP even if C-terminal TPBG is a direct target of PKCα phosphorylation.

If interactions with TPBG are phosphorylation-dependent, TPBG may also affect RBC physiology in a phosphorylation-dependent manner; it would be interesting to manipulate the phosphorylation state of C-terminal TPBG in RBCs and then record membrane capacitance responses to a depolarizing step. If we saw a difference in the evoked membrane capacitance jumps, this would indicate that PKCα may regulate RBC ribbon synapses via TPBG. In WT mice, PMA and Bis-I could be used to acutely manipulate PKCα activity and therefore the phosphorylation state of TPBG. One could also use the PKCα-KO mouse to examine the consequences of unphosphorylated TPBG throughout development, though this could be confounded by other effects of PKCα. Another powerful way to manipulate the phosphorylation state of TPBG is through genetic knock-in of engineered TPBG into the TPBG-KO mouse. The phosphorylatable serine residues in TPBG's C-terminal tail could be replaced with alanine residues to prevent phosphorylation or with aspartic acid residues to mimic phosphorylation. Membrane capacitance experiments like those in Chapter 4 would indicate whether the reduced exocytosis phenotype we saw in the TPBG-KO is recapitulated by one of the phosphorylation states and not the other. This combination of acute manipulation and knockout experiments would help illuminate whether TPBG's effect on synaptic vesicle release is dependent on PKCα and phosphorylation.

Ultrastructural examination of TPBG in the WT and TPBG-KO retina

In Chapter 3, we localized TPBG to the dendrites and axon terminals of RBCs but were unable to pinpoint the exact location of TPBG using immunofluorescence. Immunofluorescence localization of proteins is restricted by the suitability of the antibodies used and by the fundamental constraints of light microscopy which limit resolution. We can avoid the resolution limit of light microscopy using immunogold labeling and electron microscopy. Immunogold labeling uses the same principles as immunofluorescence, except secondary antibodies are conjugated to colloidal gold particles instead of fluorescent dyes. Gold is denser than most cellular components and therefore gold-labeled structures will stand out as high-contrast dark spots on an electron micrograph. Furthermore, electron microscopy has approximately 1000-fold smaller resolution limit than light microscopy (~0.2 nm compared to ~200 nm) allowing for a much closer examination of protein subcellular localization. With immunogold labeling, we can determine the localization of TPBG relative to other synaptic structures in RBC dendrites and axon terminals.

We can also use electron microscopy to examine the consequences of TPBG-KO on RBC synaptic morphology. As discussed in Chapter 1, knockout of several LRR proteins in the retina resulted in morphological deficits at both rod-to-RBC and RBC-to-AII/A17 synapses. It is possible that TPBG-KO causes similar structural deficits. Focused Ion Beam Scanning Electron Microscopy (FIB-SEM) is a relatively new imaging technique that allows for high-resolution 3D reconstruction of cell architecture. As the name suggests, FIB-SEM uses a focused ion beam to cut extremely thin sections through the tissue to achieve an unprecedented 4 nm Z-resolution. With this technique, we can generate high-resolution datasets from the OPL and IPL to reconstruct populations of RBC dendritic tips and axon terminals and compare the morphology and geometry of RBC synaptic contacts. In Chapter 4, we didn't find any effect of TPBG-KO on gross RBC dendritic morphology, but our analysis was limited by immunofluorescence. There may be more subtle morphological deficits in RBC dendrites in the TPBG-KO mouse that could be illuminated with electron microscopy. We found that TPBG-KO reduces exocytosis and synaptic vesicle release in RBC axon terminals. With FIB-SEM, we could compare the morphology of ribbon synapses between WT and TPBG-KO retinas to determine whether TPBG is required for normal synapse architecture. Even a slight change in localization or orientation of the synaptic ribbon, for example, could have profound effects on synaptic vesicle release.

TPBG and control of synaptic vesicle release

Though ribbon synapses are characterized by a large ready-releasable pool of synaptic vesicles, the capability for sustained release of neurotransmitter requires constant replenishment

of vesicles to the ribbon [12]. Previous studies indicate that vesicle replenishment in RBCs is PKCα-dependent, suggesting that PKCα may regulate vesicle replenishment through TPBG. The rate of vesicle replenishment can be examined using paired-pulse depression. Large depolarizations exhaust the ready-releasable pool of vesicles and result in a short period of depressed exocytosis in response to a second pulse. This synaptic depression is alleviated by vesicle replenishment [235–237]. By varying the interval between pulses, we can compare vesicle replenishment rates between WT and TPBG-KO RBCs. If the duration of paired-pulse synaptic depression is increased in the TPBG-KO, this would suggest that TPBG is required for synaptic vesicle replenishment in RBCs.

Tight control of synaptic vesicle release in RBCs requires extremely close physical coupling between the Ca^{2+} source and the Ca^{2+} sensors that trigger vesicle fusion such that there is a minimal delay between Ca^{2+} influx and Ca^{2+} binding. This closely-coupled system is called a nanodomain, and any small disruption of this co-localization would significantly affect the kinetics of RBC glutamate release to downstream neurons [198]. Exocytosis efficiency is a measure of exocytosis per unit of L-type Ca^{2+} channel charge transfer and our data in Chapter 4 suggests a relaxed coupling between the Ca^{2+} influx and the synaptic vesicle release machinery in the KO. We did not see any effect of TPBG-KO on the co-localization of $Ca_v1.4$ and RIBEYE, but we would not expect a slight disruption of a nanodomain system to be detectable via immunofluorescence as the physical distances involved are well below the resolution limit of light microscopy.

The nanodomain coupling of synaptic vesicle release can be tested by examining the effects of various exogenous Ca^{2+} buffers on exocytosis with patch-clamp electrophysiology. This experiment takes advantage of differing sensitivities of nanodomains to buffering by different Ca^{2+} chelators. Ca^{2+} chelators can disrupt synaptic vesicle release by intercepting Ca^{2+} as it diffuses from the its source to the sensor. Due to the very tight coupling between the Ca^{2+} source and Ca^{2+} sensor, nanodomain-controlled exocytosis is insensitive to the slow Ca^{2+} chelator EGTA [220]. However, if normal nanodomain coupling is disrupted by TPBG-KO such that the L-type Ca^{2+} channels are located slightly farther away from the Ca^{2+}-binding proteins at the synaptic ribbon, exocytosis might become sensitive to Ca^{2+} buffering by EGTA. We could compare the effects of 20 mM EGTA on exocytosis in WT and TPBG-KO RBCs. If TPBG is required for normal nanodomain architecture, we could expect that 20 mM EGTA would reduce or abolish exocytosis in TPBG-KO RBCs but have no effect on exocytosis in WT RBCs with intact nanodomains.

The downstream consequences of TPBG-KO

We found that TPBG-KO significantly reduces synaptic vesicle exocytosis from RBCs onto third-order amacrine cells. It would be interesting to examine the consequences of TPBG-KO at different points downstream of RBCs. The first way to examine the effects of TPBG-KO on downstream signaling is with whole-cell patch-clamp recording of coupled RBCs and AII-ACs. RBCs release glutamate into the IPL which is detected by calcium-permeable AMPA receptors in AII-AC dendrites. AII-AC cell bodies are easily visualized and patched in the slice and their identity can be confirmed by dye filling and examining the morphology of the cells with fluorescence. If the AII-AC cell and an RBC located directly above are patched, there is a high likelihood that the cells will be coupled [204]. Depolarizing the upstream RBC will initiate glutamate release and elicit an inward AMPA receptor-mediated Ca^{2+} current in the downstream AII-AC. This technique can be used to compare AII-AC currents between WT and TPBG-KO retinas to determine whether TPBG-KO results in reduced activation of AII-ACs or whether there are compensatory changes in AII-AC physiology as a result of reduced presynaptic output.

Another technique we could use to probe the downstream consequences of TPBG-KO is multi-electrode array (MEA) recording from populations of RGCs. RGCs are the only output neurons of the retina, so any effect of TPBG-KO on vision must be encoded by RGC action potentials. An MEA is a small chip containing hundreds or thousands of regularly spaced microscopic electrodes that can be draped across the nerve fiber layer of a whole mount retina to record action potentials from surrounding RGCs. Once a retina is placed on the MEA, it can be exposed to various complex light stimuli to evoke specific responses from specific types of RGCs. Software can then be used isolate and identify the responses of each RGC subtype. For example, an ON-type RGC will show an increased action potential firing rate when the stimulus gets brighter, whereas an OFF-type RGC will respond to the same stimulus with a decreased firing rate. Similarly, a direction-selective RGC will respond with an increased firing rate to a stimulus entering its receptive field from a specific direction and will suppress its firing rate in response to the stimulus entering from other directions. We can compare the MEA responses from WT and TPBG-KO retinas to identify differences in RGC activity between the two conditions, which could help reveal how control of synaptic vesicle release in RBCs affects retinal output.

Finally, we could examine the consequences of TPBG-KO on vision in live animals by measuring the optomotor response (OMR) in WT and TPBG-KO mice. The OMR is a highly conserved innate reflex behavior that elicits stereotypical head movements in unrestrained animals when exposed to a moving visual scene. WT mice placed on a platform in a rotating drum covered with vertical light and dark stripes will move their heads to follow the movement of the

stripes, whereas mice with visual deficits fail to track the stripes [238]. The thickness of the stripes, the contrast between light and dark stripes, and the speed of rotation can be altered to assess various components of visual performance. Furthermore, the intensity of the light stripes can be reduced to allow for the examination of scotopic visual perception in dark-adapted animals. Comparing the OMR may reveal deficits in visual behavior in TPBG-KO mice, which could help illuminate how regulation of RBC synaptic vesicle release affects perception.

Conclusion

Vision is a principal means by which humans and other animals interact with the world and visual impairment significantly impacts survival and damages quality of life. Revealing the molecular events and proteins underlying visual function is essential to producing a more comprehensive understanding of retinal physiology and to developing new solutions to address visual dysfunctions. Additionally, many mechanisms in the neural retina are conserved in other brain regions. Exploring the function of novel retinal proteins like TPBG is critical to expanding our collective understanding of vision and the nervous system as a whole.

References

1. Jékely, G. Evolution of phototaxis. *Philosophical Transactions Royal Soc B Biological Sci* **364**, 2795–2808 (2009).

2. Whippo, C. W. & Hangarter, R. P. Phototropism: Bending towards enlightenment. *Plant Cell* **18**, 1110–1119 (2006).

3. Nilsson, D.-E. The evolution of eyes and visually guided behaviour. *Philosophical Transactions Royal Soc B Biological Sci* **364**, 2833–2847 (2009).

4. Lamb, T. D., Collin, S. P. & Pugh, E. N. Evolution of the vertebrate eye: opsins, photoreceptors, retina and eye cup. *Nat Rev Neurosci* **8**, 960–976 (2007).

5. Masland, R. H. The neuronal organization of the retina. *Neuron* **76**, 266–280 (2012).

6. Masland, R. H. The fundamental plan of the retina. *Nat Neurosci* **4**, 877–886 (2001).

7. Demb, J. B. & Singer, J. H. Functional circuitry of the tetina. *Annu Rev Vis Sc* **1**, 263–289 (2015).

8. Jeon, C.-J., Strettoi, E. & Masland, R. H. The major cell populations of the mouse retina. *J Neurosci* **18**, 8936–8946 (1998).

9. Kolb, H., Linberg, K. A. & Fisher, S. K. Neurons of the human retina: A Golgi study. *J Comp Neurol* **318**, 147–187 (1992).

10. Okawa, H. & Sampath, A. P. Optimization of single-photon response transmission at the rod-to-rod bipolar synapse. *Physiology* **22**, 279–286 (2007).

11. Sampath, A. P. & Rieke, F. Selective transmission of single photon responses by saturation at the rod-to-rod bipolar synapse. *Neuron* **41**, 431–443 (2004).

12. Dieck, S. T. & Brandstätter, J. H. Ribbon synapses of the retina. *Cell Tissue Res* **326**, 339–346 (2006).

13. Thoreson, W. B. & Hays, C. L. How ribbons make 'sense' for vision. *Biochem* **42**, 36–41 (2020).

14. Thoreson, W. B., Babai, N. & Bartoletti, T. M. Feedback from horizontal cells to rod photoreceptors in vertebrate retina. *J Neurosci Official J Soc Neurosci* **28**, 5691–5 (2008).

15. Kamermans, M. & Spekreijse, H. The feedback pathway from horizontal cells to cones A mini review with a look ahead. *Vision Res* **39**, 2449–2468 (1999).

16. Ahnelt, P. K. & Kolb, H. The mammalian photoreceptor mosaic-adaptive design. *Prog Retin Eye Res* **19**, 711–777 (2000).

17. Zhang, A., Zhang, J. & Wu, S. M. Electrical coupling, receptive fields, and relative rod/cone inputs of horizontal cells in the tiger salamander retina. *J Comp Neurol* **499**, 422–431 (2006).

18. Mangel, S. C. Analysis of the horizontal cell contribution to the receptive field surround of ganglion cells in the rabbit retina. *J Physiology* **442**, 211–234 (1991).

19. Thoreson, W. B. & Mangel, S. C. Lateral interactions in the outer retina. *Prog Retin Eye Res* **31**, 407–441 (2012).

20. Ströh, S. *et al.* Eliminating glutamatergic input onto horizontal cells changes the dynamic range and receptive field organization of mouse retinal ganglion cells. *J Neurosci* **38**, 2015–2028 (2018).

21. Shekhar, K. *et al.* Comprehensive classification of retinal bipolar neurons by single-cell transcriptomics. *Cell* **166**, 1308-1323.e30 (2016).

22. Tsukamoto, Y. & Omi, N. Classification of mouse retinal bipolar cells: Type-specific connectivity with special reference to rod-driven AII amacrine pathways. *Front Neuroanat* **11**, 92 (2017).

23. Mariani, A. P. The neuronal organization of the outer plexiform layer of the primate retina. *Int Rev Cytol* **86**, 285–320 (1984).

24. Ishida, A. T., Stell, W. K. & Lightfoot, D. O. Rod and cone inputs to bipolar cells in goldfish retina. *J Comp Neurol* **191**, 315–335 (1980).

25. Boycott, B. B. & Wässle, H. Morphological classification of bipolar cells of the primate retina. *Eur J Neurosci* **3**, 1069–1088 (1991).

26. Helmstaedter, M. *et al.* Connectomic reconstruction of the inner plexiform layer in the mouse retina. *Nature* **500**, 168–174 (2013).

27. Badea, T. C. & Nathans, J. Quantitative analysis of neuronal morphologies in the mouse retina visualized by using a genetically directed reporter. *J Comp Neurology* **480**, 331–351 (2004).

28. Lin, B. & Masland, R. H. Populations of wide-field amacrine cells in the mouse retina. *J Comp Neurol* **499**, 797–809 (2006).

29. Macneil, M. A., Heussy, J. K., Dacheux, R. F., Raviola, E. & Masland, R. H. The shapes and numbers of amacrine cells: Matching of photofilled with Golgi-stained cells in the rabbit retina and comparison with other mammalian species. *J Comp Neurol* **413**, 305–326 (1999).

30. Yan, W. *et al.* Mouse retinal cell atlas: Molecular identification of over sixty amacrine cell types. *J Neurosci* **40**, 5177–5195 (2020).

31. Franke, K. *et al.* Inhibition decorrelates visual feature representations in the inner retina. *Nature* **542**, 439–444 (2017).

32. Graydon, C. W. *et al.* Synaptic transfer between rod and cone pathways mediated by AII amacrine cells in the mouse retina. *Curr Biol* **28**, 2739-2751.e3 (2018).

33. Sanes, J. R. & Masland, R. H. The types of retinal ganglion cells: Current status and implications for neuronal classification. *Annu Rev Neurosci* **38**, 1–26 (2015).

34. Berson, D. Strange vision: ganglion cells as circadian photoreceptors. *Trends Neurosci* **26**, 314–320 (2003).

35. Yau, K. W. Phototransduction mechanism in retinal rods and cones. The Friedenwald Lecture. *Invest Ophth Vis Sci* **35**, 9–32 (1994).

36. Kawamura, S. Phototransduction, excitation and adaptation. *Neurobiology and clinical aspects of the outer retina* 105–131 (1995).

37. Li, S. *et al.* Morphological diversity of the rod spherule: A study of serially reconstructed electron micrographs. *Plos One* **11**, e0150024 (2016).

38. Nemitz, L., Dedek, K. & Janssen-Bienhold, U. Rod bipolar cells require horizontal cells for invagination into the terminals of rod photoreceptors. *Front Cell Neurosci* **13**, 423 (2019).

39. Morgans, C. W., Brown, R. L. & Duvoisin, R. M. TRPM1: The endpoint of the mGluR6 signal transduction cascade in retinal ON-bipolar cells. *Bioessays* **32**, 609–614 (2010).

40. Vardi, N., Duvoisin, R., Wu, G. & Sterling, P. Localization of mGluR6 to dendrites of ON bipolar cells in primate retina. *J Comp Neurol* **423**, 402–412 (2000).

41. Nakajima, Y. *et al.* Molecular characterization of a novel retinal metabotropic glutamate receptor mGluR6 with a high agonist selectivity for L-2-amino-4-phosphonobutyrate. *J Biological Chem* **268**, 11868–73 (1993).

42. Masu, M. *et al.* Specific deficit of the ON response in visual transmission by targeted disruption of the mGluR6 gene. *Cell* **80**, 757–765 (1995).

43. Shen, Y. *et al.* A transient receptor potential-like channel mediates synaptic transmission in rod bipolar cells. *J Neurosci* **29**, 6088–6093 (2009).

44. Koike, C., Numata, T., Ueda, H., Mori, Y. & Furukawa, T. TRPM1: A vertebrate TRP channel responsible for retinal ON bipolar function. *Cell Calcium* **48**, 95–101 (2010).

45. Morgans, C. W. *et al.* TRPM1 is required for the depolarizing light response in retinal ON-bipolar cells. *Proc National Acad Sci* **106**, 19174–19178 (2009).

46. Orlandi, C., Cao, Y. & Martemyanov, K. A. Orphan receptor GPR179 forms macromolecular complexes with components of metabotropic signaling cascade in retina ON-bipolar neurons. *Invest Ophth Vis Sci* **54**, 7153–7161 (2013).

47. Ray, T. A. *et al.* GPR179 Is required for high sensitivity of the mGluR6 signaling cascade in depolarizing bipolar cells. *J Neurosci* **34**, 6334–6343 (2014).

48. Orhan, E. *et al.* Further insights into GPR179: Expression, localization, and associated pathogenic mechanisms leading to complete congenital stationary night blindness. *Invest Ophth Vis Sci* **54**, 8041–8050 (2013).

49. Cao, Y., Posokhova, E. & Martemyanov, K. A. TRPM1 forms complexes with nyctalopin in vivo and accumulates in postsynaptic compartment of ON-bipolar neurons in mGluR6-dependent manner. *J Neurosci* **31**, 11521–11526 (2011).

50. Pearring, J. N. *et al.* A role for nyctalopin, a small leucine-rich repeat protein, in localizing the TRP melastatin 1 channel to retinal depolarizing bipolar cell dendrites. *J Neurosci* **31**, 10060–10066 (2011).

51. Gregg, R. G. *et al.* Identification of the gene and the mutation responsible for the mouse nob phenotype. *Invest Ophth Vis Sci* **44**, 378–384 (2003).

52. Hasan, N. *et al.* Presynaptic expression of LRIT3 transsynaptically organizes the postsynaptic glutamate signaling complex containing TRPM1. *Cell Reports* **27**, 3107-3116.e3 (2019).

53. Neuillé, M. *et al.* LRIT3 differentially affects connectivity and synaptic transmission of cones to ON- and OFF-bipolar cells. *Invest Ophth Vis Sci* **58**, 1768–1778 (2017).

54. Neuillé, M. *et al.* LRIT3 is essential to localize TRPM1 to the dendritic tips of depolarizing bipolar cells and may play a role in cone synapse formation. *Eur J Neurosci* **42**, 1966–1975 (2015).

55. Heidelberger, R. & Matthews, G. Calcium influx and calcium current in single synaptic terminals of goldfish retinal bipolar neurons. *J Physiology* **447**, 235–256 (1992).

56. Gao, F. & Wu, S. M. Multiple types of spontaneous excitatory synaptic currents in salamander retinal ganglion cells. *Brain Res* **821**, 487–502 (1999).

57. Matthews, G. Synaptic mechanisms of bipolar cell terminals. *Vision Res* **39**, 2469–2476 (1999).

58. Mennerick, S. & Matthews, G. Ultrafast exocytosis elicited by calcium current in synaptic terminals of retinal bipolar neurons. *Neuron* **17**, 1241–1249 (1996).

59. Hartveit, E. Reciprocal synaptic interactions between rod bipolar cells and amacrine cells in the rat retina. *J Neurophysiol* **81**, 2923–2936 (1999).

60. Chávez, A. E., Singer, J. H. & Diamond, J. S. Fast neurotransmitter release triggered by Ca influx through AMPA-type glutamate receptors. *Nature* **443**, 705–708 (2006).

61. Chávez, A. E. & Diamond, J. S. Diverse mechanisms underlie glycinergic feedback transmission onto rod bipolar cells in rat retina. *J Neurosci* **28**, 7919–7928 (2008).

62. Chávez, A. E., Grimes, W. N. & Diamond, J. S. Mechanisms underlying lateral GABAergic feedback onto rod bipolar cells in rat retina. *J Neurosci* **30**, 2330–2339 (2010).

63. Eggers, E. D. & Lukasiewicz, P. D. GABA A, GABA C and glycine receptor-mediated inhibition differentially affects light-evoked signaling from mouse retinal rod bipolar cells. *J Physiology* **572**, 215–225 (2006).

64. Frazao, R., Nogueira, M. I. & Wässle, H. Colocalization of synaptic GABAC-receptors with GABAA-receptors and glycine-receptors in the rodent central nervous system. *Cell Tissue Res* **330**, 1–15 (2007).

65. Hull, C. & von Gersdorff, H. Fast endocytosis is inhibited by GABA-mediated chloride influx at a presynaptic terminal. *Neuron* **44**, 469–482 (2004).

66. Veruki, M. L. & Hartveit, E. AII (Rod) amacrine cells form a network of electrically coupled interneurons in the mammalian retina. *Neuron* **33**, 935–946 (2002).

67. Wässle, H. Parallel processing in the mammalian retina. *Nat Rev Neurosci* **5**, 747–757 (2004).

68. Sassoe-Pognetto, M., Wassle, H. & Grunert, U. Glycinergic synapses in the rod pathway of the rat retina: cone bipolar cells express the alpha 1 subunit of the glycine receptor. *J Neurosci* **14**, 5131–5146 (1994).

69. Pang, J., Gao, F. & Wu, S. M. Light-evoked current responses in rod bipolar cells, cone depolarizing bipolar cells and AII amacrine cells in dark-adapted mouse retina. *J Physiology* **558**, 897–912 (2004).

70. Dunn, F. A., Doan, T., Sampath, A. P. & Rieke, F. Controlling the gain of rod-mediated signals in the mammalian retina. *J Neurosci* **26**, 3959–3970 (2006).

71. Ke, J.-B. *et al.* Adaptation to background light enables contrast coding at rod bipolar cell synapses. *Neuron* **81**, 388–401 (2014).

72. Szikra, T. *et al.* Rods in daylight act as relay cells for cone-driven horizontal cell–mediated surround inhibition. *Nat Neurosci* **17**, 1728–1735 (2014).

73. Nakashima, S. Protein kinase C (PKC): Regulation and biological function. *J Biochem* **132**, 669–675 (2002).

74. Greferath, U., Grünert, U. & Wässle, H. Rod bipolar cells in the mammalian retina show protein kinase C-like immunoreactivity. *J Comp Neurol* **301**, 433–442 (1990).

75. Haverkamp, S., Ghosh, K. K., Hirano, A. A. & Wässle, H. Immunocytochemical description of five bipolar cell types of the mouse retina. *J Comp Neurol* **455**, 463–476 (2003).

76. Haverkamp, S., Haeseleer, F. & Hendrickson, A. A comparison of immunocytochemical markers to identify bipolar cell types in human and monkey retina. *Visual Neurosci* **20**, 589–600 (2003).

77. Osborne, N. N., Broyden, N. J., Barnett, N. L. & Morris, N. J. Protein kinase C (α and β) immunoreactivity in rabbit and rat retina: Effect of phorbol esters and transmitter agonists on

immunoreactivity and the translocation of the enzyme from cytosolic to membrane compartments. *J Neurochem* **57**, 594–604 (1991).

78. Berglund, K., Midorikawa, M. & Tachibana, M. Increase in the pool size of releasable synaptic vesicles by the activation of protein kinase C in goldfish retinal bipolar cells. *J Neurosci* **22**, 4776–4785 (2002).

79. Tachibana, M. Regulation of transmitter release from retinal bipolar cells. *Prog Biophysics Mol Biology* **72**, 109–133 (1999).

80. Minami, N., Berglund, K., Sakaba, T., Kohmoto, H. & Tachibana, M. Potentiation of transmitter release by protein kinase C in goldfish retinal bipolar cells. *J Physiology* **512**, 219–225 (1998).

81. Job, C. & Lagnado, L. Calcium and protein kinase C regulate the actin cytoskeleton in the synaptic terminal of retinal bipolar cells. *J Cell Biology* **143**, 1661–1672 (1998).

82. Doussau, F. & Augustine, G. J. The actin cytoskeleton and neurotransmitter release: An overview. *Biochimie* **82**, 353–363 (2000).

83. Gillette, M. A. & Dacheux, R. F. Protein kinase modulation of GABAA currents in rabbit retinal rod bipolar cells. *J Neurophysiol* **76**, 3070–86 (1996).

84. Feigenspan, A. & Bormann, J. Modulation of GABAC receptors in rat retinal bipolar cells by protein kinase C. *J Physiology* **481**, 325–330 (1994).

85. Rampino, M. A. F. & Nawy, S. A. Relief of Mg2+-dependent inhibition of TRPM1 by PKCα at the rod bipolar cell synapse. *J Neurosci* **31**, 13596–13603 (2011).

86. Ruether, K. *et al.* PKCα is essential for the proper activation and termination of rod bipolar cell response. *Invest Ophth Vis Sci* **51**, 6051–6058 (2010).

87. Xiong, W.-H. *et al.* The effect of PKCα on the light response of rod bipolar cells in the mouse retina. *Invest Ophth Vis Sci* **56**, 4961–4974 (2015).

88. Kobe, B. & Deisenhofer, J. The leucine-rich repeat: a versatile binding motif. *Trends Biochem Sci* **19**, 415–421 (1994).

89. Kobe, B. & Deisenhofer, J. A structural basis of the interactions between leucine-rich repeats and protein ligands. *Nature* **374**, 183–186 (1995).

90. Kobe, B. & Kajava, A. V. The leucine-rich repeat as a protein recognition motif. *Curr Opin Struc Biol* **11**, 725–732 (2001).

91. Morgans, C. W., Ren, G. & Akileswaran, L. Localization of nyctalopin in the mammalian retina. *Eur J Neurosci* **23**, 1163–1171 (2006).

92. Bech-Hansen, N. T. *et al.* Loss-of-function mutations in a calcium-channel α1-subunit gene in Xp11.23 cause incomplete X-linked congenital stationary night blindness. *Nat Genet* **19**, 264–267 (1998).

93. Pusch, C. M. *et al.* The complete form of X-linked congenital stationary night blindness is caused by mutations in a gene encoding a leucine-rich repeat protein. *Nat Genet* **26**, 324–327 (2000).

94. Chang, B. *et al.* The nob2 mouse, a null mutation in Cacna1f: Anatomical and functional abnormalities in the outer retina and their consequences on ganglion cell visual responses. *Visual Neurosci* **23**, 11–24 (2006).

95. Ball, S. L., Pardue, M. T., McCall, M. A., Gregg, R. G. & Peachey, N. S. Immunohistochemical analysis of the outer plexiform layer in the nob mouse shows no abnormalities. *Visual Neurosci* **20**, 267–272 (2003).

96. Ueno, A. *et al.* Lrit1, a retinal transmembrane protein, regulates selective synapse formation in cone photoreceptor cells and visual acuity. *Cell Reports* **22**, 3548–3561 (2018).

97. Sarria, I. *et al.* LRIT1 modulates adaptive changes in synaptic communication of cone photoreceptors. *Cell Reports* **22**, 3562–3573 (2018).

98. Zeitz, C. *et al.* Whole-exome sequencing identifies LRIT3 mutations as a cause of autosomal-recessive complete congenital stationary night blindness. *Am J Hum Genetics* **92**, 67–75 (2013).

99. Hasan, N. *et al.* LRIT3 is required for nyctalopin expression and normal ON and OFF pathway signaling in the retina. *Eneuro* **7**, ENEURO.0002-20.2020 (2020).

100. Cao, Y. *et al.* Mechanism for selective synaptic wiring of rod photoreceptors into the retinal circuitry and its role in vision. *Neuron* **87**, 1248–1260 (2015).

101. Dunn, H. A., Patil, D. N., Cao, Y., Orlandi, C. & Martemyanov, K. A. Synaptic adhesion protein ELFN1 is a selective allosteric modulator of group III metabotropic glutamate receptors in trans. *Proc National Acad Sci* **115**, 201722498 (2018).

102. Cao, Y. *et al.* Interplay between cell-adhesion molecules governs synaptic wiring of cone photoreceptors. *Proc National Acad Sci* **117**, 23914–23924 (2020).

103. Dunn, H. A., Zucca, S., Dao, M., Orlandi, C. & Martemyanov, K. A. Distinct neuronal expression patterns of ELFN1 and ELFN2: Trans-synaptic modulators of group III mGluRs. *Mol Psychiatr* **24**, 1769–1769 (2019).

104. Agosto, M. A. & Wensel, T. G. LRRTM4 is a member of the transsynaptic complex between rod photoreceptors and bipolar cells. *J Comp Neurol* **529**, 221–233 (2020).

105. Sinha, R. *et al.* LRRTM4: A novel regulator of presynaptic inhibition and ribbon synapse arrangements of retinal bipolar cells. *Neuron* **105**, 1007-1017.e5 (2020).

106. Berntson, A., Smith, R. G. & Taylor, W. R. Transmission of single photon signals through a binary synapse in the mammalian retina. *Visual Neurosci* **21**, 693–702 (2004).

107. Abd-El-Barr, M. M. *et al.* Genetic dissection of rod and cone pathways in the dark-adapted mouse retina. *J Neurophysiol* **102**, 1945–1955 (2009).

108. Thompson, A. *et al.* Tandem mass tags: A novel quantification strategy for comparative analysis of complex protein mixtures by MS/MS. *Anal Chem* **75**, 1895–1904 (2003).

109. Erickson, B. K. *et al.* Evaluating multiplexed quantitative phosphopeptide analysis on a hybrid quadrupole mass filter/Linear ion trap/Orbitrap mass spectrometer. *Anal Chem* **87**, 1241–1249 (2015).

110. Plubell, D. L. *et al.* Extended multiplexing of tandem mass tags (TMT) labeling reveals age and high fat diet specific proteome changes in mouse epididymal adipose tissue. *Mol Cell Proteomics* **16**, 873–890 (2017).

111. Rueden, C. T. *et al.* ImageJ2: ImageJ for the next generation of scientific image data. *Bmc Bioinformatics* **18**, 529 (2017).

112. Schindelin, J., Rueden, C. T., Hiner, M. C. & Eliceiri, K. W. The ImageJ ecosystem: An open platform for biomedical image analysis. *Mol Reprod Dev* **82**, 518–529 (2015).

113. Kettenbach, A. N. & Gerber, S. A. Rapid and reproducible single-stage phosphopeptide enrichment of complex peptide mixtures: Application to general and phosphotyrosine-Specific phosphoproteomics experiments. *Anal Chem* **83**, 7635–7644 (2011).

114. Paulo, J. A. *et al.* Effects of MEK inhibitors GSK1120212 and PD0325901 in vivo using 10-plex quantitative proteomics and phosphoproteomics. *Proteomics* **15**, 462–473 (2015).

115. Eng, J. K., McCormack, A. L. & Yates, J. R. An approach to correlate tandem mass spectral data of peptides with amino acid sequences in a protein database. *J Am Soc Mass Spectr* **5**, 976–989 (1994).

116. Käll, L., Canterbury, J. D., Weston, J., Noble, W. S. & MacCoss, M. J. Semi-supervised learning for peptide identification from shotgun proteomics datasets. *Nat Methods* **4**, 923–925 (2007).

117. Taus, T. *et al.* Universal and confident phosphorylation site localization using phosphoRS. *J Proteome Res* **10**, 5354–5362 (2011).

118. Gentleman, R. C. *et al.* Bioconductor: open software development for computational biology and bioinformatics. *Genome Biol* **5**, R80 (2004).

119. Robinson, M. D., McCarthy, D. J. & Smyth, G. K. edgeR: a Bioconductor package for differential expression analysis of digital gene expression data. *Bioinformatics* **26**, 139–140 (2010).

120. Robinson, M. D. & Oshlack, A. A scaling normalization method for differential expression analysis of RNA-seq data. *Genome Biol* **11**, R25 (2010).

121. Benjamini, Y. & Hochberg, Y. Controlling the false siscovery rate: A practical and powerful approach to multiple testing. *J Royal Statistical Soc Ser B Methodol* **57**, 289–300 (1995).

122. Perez-Riverol, Y. *et al.* The PRIDE database and related tools and resources in 2019: improving support for quantification data. *Nucleic Acids Res* **47**, gky1106- (2018).

123. Gabriel, R., Lesauter, J., Silver, R., Garcia-España, A. & Witkovsky, P. Diurnal and circadian variation of protein kinase C immunoreactivity in the rat retina. *J Comp Neurol* **439**, 140–150 (2001).

124. Nishizuka, Y. Intracellular signaling by hydrolysis of phospholipids and activation of protein kinase C. *Science* **258**, 607–614 (1992).

125. Koike, C. *et al.* TRPM1 is a component of the retinal ON bipolar cell transduction channel in the mGluR6 cascade. *Proc National Acad Sci* **107**, 332–337 (2010).

126. Boycott, B. B. & Dowling, J. E. Organization of the primate retina: Light microscopy. *Philosophical Transactions Royal Soc Lond Ser B Biological Sci* **255**, 109–184 (1969).

127. Dowling, J. E. & Boycott, B. B. Organization of the primate retina: electron microscopy. *Proc Royal Soc Lond Ser B Biological Sci* **166**, 80–111 (1966).

128. Shaw, D. M. *et al.* Glycosylation and epitope mapping of the 5T4 glycoprotein oncofoetal antigen. *Biochem J* **363**, 137–145 (2002).

129. Imamura, F. *et al.* A leucine-rich repeat membrane protein, 5T4, is expressed by a subtype of granule cells with dendritic arbors in specific strata of the mouse olfactory bulb. *J Comp Neurol* **495**, 754–768 (2006).

130. Garg, R., Caino, M. C. & Kazanietz, M. G. Regulation of transcriptional networks by PKC isozymes: Identification of c-rel as a key transcription factor for PKC-regulated genes. *Plos One* **8**, e67319 (2013).

131. Ritchie, M. E. *et al.* limma powers differential expression analyses for RNA-sequencing and microarray studies. *Nucleic Acids Res* **43**, e47–e47 (2015).

132. Chen, X., Zhao, X., Abeyweera, T. P. & Rotenberg, S. A. Analysis of substrates of protein kinase C isoforms in human breast cells by the traceable kinase method. *Biochemistry-us* **51**, 7087–7097 (2012).

133. Garbett, D., LaLonde, D. P. & Bretscher, A. The scaffolding protein EBP50 regulates microvillar assembly in a phosphorylation-dependent manner. *J Cell Biology* **191**, 397–413 (2010).

134. Duarte, M. L. *et al.* Protein folding creates structure-based, noncontiguous consensus phosphorylation motifs recognized by kinases. *Sci Signal* **7**, ra105–ra105 (2014).

135. Lee, Y.-H., Park, J.-W. & Bae, Y.-S. Regulation of protein kinase CK2 catalytic activity by protein kinase C and phospholipase D2. *Biochimie* **121**, 131–139 (2016).

136. Malkani, N. *et al.* Increased IGFBP-1 phosphorylation in response to leucine deprivation is mediated by CK2 and PKC. *Mol Cell Endocrinol* **425**, 48–60 (2016).

137. Chung, H. J., Huang, Y. H., Lau, L.-F. & Huganir, R. L. Regulation of the NMDA receptor complex and trafficking by activity-dependent phosphorylation of the NR2B subunit PDZ ligand. *J Neurosci* **24**, 10248–10259 (2004).

138. Liu, Z. *et al.* Snail regulated by PKC/GSK-3β pathway is crucial for EGF-induced epithelial-mesenchymal transition (EMT) of cancer cells. *Cell Tissue Res* **358**, 491–502 (2014).

139. Moore, S. F. *et al.* Dual regulation of glycogen synthase kinase 3 (GSK3)α/β by protein kinase C (PKC)α and akt promotes thrombin-mediated integrin αIIbβ3 activation and granule secretion in platelets. *J Biol Chem* **288**, 3918–3928 (2013).

140. Farrugia, A. J. & Calvo, F. The Borg family of Cdc42 effector proteins Cdc42EP1–5. *Biochem Soc T* **44**, 1709–1716 (2016).

141. Huttlin, E. L. *et al.* A tissue-specific atlas of mouse protein phosphorylation and expression. *Cell* **143**, 1174–1189 (2010).

142. Villén, J., Beausoleil, S. A., Gerber, S. A. & Gygi, S. P. Large-scale phosphorylation analysis of mouse liver. *Proc National Acad Sci* **104**, 1488–1493 (2007).

143. Blackshaw, S. *et al.* Genomic analysis of mouse retinal development. *Plos Biol* **2**, e247 (2004).

144. Huang, J., Possin, D. E. & Saari, J. C. Localizations of visual cycle components in retinal pigment epithelium. *Mol Vis* **15**, 223–34 (2009).

145. Bonilha, V. L. *et al.* Support for a proposed retinoid-processing protein complex in apical retinal pigment epithelium. *Exp Eye Res* **79**, 419–422 (2004).

146. Nawrot, M. *et al.* Cellular retinaldehyde-binding protein interacts with ERM-binding phosphoprotein 50 in retinal pigment epithelium. *Invest Ophth Vis Sci* **45**, 393–401 (2004).

147. Yu, K. *et al.* Expression of protein kinase C isoforms in cultured human retinal pigment epithelial cells. *Graefe's Archive Clin Exp Ophthalmol* **245**, 993–999 (2006).

148. Kishi, H., Mishima, H. K. & Yamashita, U. Growth regulation of retinal pigment epithelial (RPE) cells in vitro. *Curr Eye Res* **13**, 661–668 (1994).

149. Sheu, S.-J. *et al.* Transforming growth factor-β regulates human retinal pigment epithelial cell phagocytosis by influencing a protein kinase C-dependent pathway. *Graefe's Archive Clin Exp Ophthalmol* **232**, 695–701 (1994).

150. Kishi, H., Mishima, H. K. & Yamashita, U. Involvement of the protein kinase pathway in melanin synthesis by chick retinal pigment epithelial cells. *Cell Biol Int* **24**, 79–83 (2000).

151. Zhao, Y., Malinauskas, T., Harlos, K. & Jones, E. Y. Structural insights into the inhibition of wnt signaling by cancer antigen 5T4/wnt-activated inhibitory factor 1. *Structure* **22**, 612–620 (2014).

152. Lee, H.-J. & Zheng, J. J. PDZ domains and their binding partners: structure, specificity, and modification. *Cell Commun Signal* **8**, 8 (2010).

153. Ward, C. M., Barrow, K., Woods, A. M. & Stern, P. L. The 5T4 oncofoetal antigen is an early differentiation marker of mouse ES cells and its absence is a useful means to assess pluripotency. *J Cell Sci* **116**, 4533–4542 (2003).

154. Ward, C. M., Eastham, A. M. & Stern, P. L. Cell surface 5T4 antigen is transiently upregulated during early human embryonic stem cell differentiation: Effect of 5T4 phenotype on neural lineage formation. *Exp Cell Res* **312**, 1713–1726 (2006).

155. Southall, P. *et al.* Immunohistological distribution of 5T4 antigen in normal and malignant tissues. *Brit J Cancer* **61**, 89–95 (1990).

156. Barrow, K. M., Ward, C. M., Rutter, J., Ali, S. & Stern, P. L. Embryonic expression of murine 5T4 oncofoetal antigen is associated with morphogenetic events at implantation and in developing epithelia. *Dev Dynam* **233**, 1535–1545 (2005).

157. King, K. W., Sheppard, F. C., Westwater, C., Stern, P. L. & Myers, K. A. Organization of the mouse and human 5T4 oncofoetal leucine-rich glycoprotein genes and expression in foetal and adult murine tissues. *Biochimica Et Biophysica Acta Bba - Gene Struct Expr* **1445**, 257–270 (1999).

158. Awan, A. *et al.* 5T4 Interacts with TIP-2/GIPC, a PDZ protein, with implications for metastasis. *Biochem Bioph Res Co* **290**, 1030–1036 (2002).

159. Carsberg, C. J., Myers, K. A., Evans, G. S., Allen, T. D. & Stern, P. L. Metastasis-associated 5T4 oncofoetal antigen is concentrated at microvillus projections of the plasma membrane. *J Cell Sci* **108**, 2905–2916 (1995).

160. McGinn, O. J., Marinov, G., Sawan, S. & Stern, P. L. CXCL12 receptor preference, signal transduction, biological response and the expression of 5T4 oncofoetal glycoprotein. *J Cell Sci* **125**, 5467–5478 (2012).

161. Southgate, T. D. *et al.* CXCR4 mediated chemotaxis is regulated by 5T4 oncofetal glycoprotein in mouse embryonic cells. *Plos One* **5**, e9982 (2010).

162. Pukrop, T. & Binder, C. The complex pathways of Wnt 5a in cancer progression. *J Mol Med* **86**, 259–266 (2008).

163. Weeraratna, A. T. *et al.* Wnt5a signaling directly affects cell motility and invasion of metastatic melanoma. *Cancer Cell* **1**, 279–288 (2002).

164. Takahashi, H. *et al.* A subtype of olfactory bulb interneurons is required for odor detection and discrimination behaviors. *J Neurosci* **36**, 8210–8227 (2016).

165. Yoshihara, S.-I. *et al.* 5T4 glycoprotein regulates the sensory input-dependent development of a specific subtype of newborn interneurons in the mouse olfactory bulb. *J Neurosci* **32**, 2217–2226 (2012).

166. Yoshihara, S.-I., Takahashi, H. & Tsuboi, A. Molecular mechanisms regulating the dendritic development of newborn olfactory bulb interneurons in a sensory experience-dependent manner. *Front Neurosci-switz* **9**, 514 (2016).

167. Euler, T., Haverkamp, S., Schubert, T. & Baden, T. Retinal bipolar cells: elementary building blocks of vision. *Nat Rev Neurosci* **15**, 507–519 (2014).

168. Wakeham, C. M. *et al.* Identification of PKCα-dependent phosphoproteins in mouse retina. *J Proteomics* **206**, 103423 (2019).

169. Hole, N. & Stern, P. A 72 kD trophoblast glycoprotein defined by a monoclonal antibody. *Brit J Cancer* **57**, 239–246 (1988).

170. Kagermeier-Schenk, B. *et al.* Waif1/5T4 inhibits Wnt/β-catenin signaling and activates noncanonical Wnt pathways by modifying LRP6 subcellular localization. *Dev Cell* **21**, 1129–1143 (2011).

171. Woods, S. M., Mountjoy, E., Muir, D., Ross, S. E. & Atan, D. A comparative analysis of rod bipolar cell transcriptomes identifies novel genes implicated in night vision. *Sci Rep-uk* **8**, 5506 (2018).

172. Schmitz, F., Königstorfer, A. & Südhof, T. C. RIBEYE, a component of synaptic ribbons. *Neuron* **28**, 857–872 (2000).

173. Tayou, J. *et al.* Regulator of G protein signaling 7 (RGS7) can exist in a homo-oligomeric form that is regulated by Gαo and R7-binding protein. *J Biol Chem* **291**, 9133–9147 (2016).

174. Morgans, C. W. *et al.* Gβ5–RGS complexes co-localize with mGluR6 in retinal ON-bipolar cells. *Eur J Neurosci* **26**, 2899–2905 (2007).

175. Hasan, N., Ray, T. A. & Gregg, R. G. CACNA1S expression in mouse retina: Novel isoforms and antibody cross-reactivity with GPR179. *Visual Neurosci* **33**, E009 (2016).

176. Haverkamp, S. & Wässle, H. Immunocytochemical analysis of the mouse retina. *J Comp Neurol* **424**, 1–23 (2000).

177. Vries, L. D., Lou, X., Zhao, G., Zheng, B. & Farquhar, M. G. GIPC, a PDZ domain containing protein, interacts specifically with the C terminus of RGS-GAIP. *Proc National Acad Sci* **95**, 12340–12345 (1998).

178. Hu, L. A. *et al.* GIPC interacts with the β1-adrenergic receptor and regulates β1-adrenergic receptor-mediated ERK activation. *J Biol Chem* **278**, 26295–26301 (2003).

179. Wieman, H. L. *et al.* An essential role for the Glut1 PDZ-binding motif in growth factor regulation of Glut1 degradation and trafficking. *Biochem J* **418**, 345–367 (2009).

180. Dorrell, M. I., Aguilar, E., Weber, C. & Friedlander, M. Global gene expression analysis of the developing postnatal mouse retina. *Invest Ophth Vis Sci* **45**, 1009–1019 (2004).

181. Mu, X. *et al.* Gene expression in the developing mouse retina by EST sequencing and microarray analysis. *Nucleic Acids Res* **29**, 4983–4993 (2001).

182. Zhang, C., Kolodkin, A. L., Wong, R. O. & James, R. E. Establishing wiring specificity in visual system circuits: From the retina to the brain. *Annu Rev Neurosci* **40**, 1–30 (2016).

183. Sarin, S. *et al.* Role for Wnt signaling in retinal neuropil development: Analysis via RNA-seq and in vivo somatic CRISPR mutagenesis. *Neuron* **98**, 109-126.e8 (2018).

184. Duncan, D. S. *et al.* Ccl5 mediates proper wiring of feedforward and lateral inhibition pathways in the inner retina. *Front Neurosci-switz* **12**, 702 (2018).

185. Macosko, E. Z. *et al.* Highly parallel genome-wide expression profiling of individual cells using nanoliter droplets. *Cell* **161**, 1202–1214 (2015).

186. Wakeham, C. M., Ren, G. & Morgans, C. W. Expression and distribution of trophoblast glycoprotein in the mouse retina. *J Comp Neurol* **528**, 1660–1671 (2020).

187. Morgans, C. W. Neurotransmitter release at ribbon synapses in the retina. *Immunol Cell Biol* **78**, 442–446 (2000).

188. Moser, T., Grabner, C. P. & Schmitz, F. Sensory processing at ribbon synapses in the retina and the cochlea. *Physiol Rev* **100**, 103–144 (2020).

189. Schindelin, J. *et al.* Fiji: an open-source platform for biological-image analysis. *Nat Methods* **9**, 676–682 (2012).

190. Gillis, K. D. Admittance-based measurement of membrane capacitance using the EPC-9 patch-clamp amplifier. *Pflügers Archiv* **439**, 655–664 (2000).

191. Oltedal, L. & Hartveit, E. Transient release kinetics of rod bipolar cells revealed by capacitance measurement of exocytosis from axon terminals in rat retinal slices. *J Physiology* **588**, 1469–1487 (2010).

192. Balakrishnan, V., Puthussery, T., Kim, M.-H., Taylor, W. R. & von Gersdorff, H. Synaptic vesicle exocytosis at the dendritic lobules of an inhibitory interneuron in the mammalian retina. *Neuron* **87**, 563–575 (2015).

193. Robson, J. G. & Frishman, L. J. The rod-driven a-wave of the dark-adapted mammalian electroretinogram. *Prog Retin Eye Res* **39**, 1–22 (2014).

194. Stockton, R. A. & Slaughter, M. M. B-wave of the electroretinogram. A reflection of ON bipolar cell activity. *J Gen Physiology* **93**, 101–122 (1989).

195. Ogden, T. E. The oscillatory waves of the primate electroretinogram. *Vision Res* **13**, 1059-IN4 (1973).

196. Xu, Y. *et al.* mGluR6 deletion renders the TRPM1 channel in retina inactive. *J Neurophysiol* **107**, 948–957 (2012).

197. von Gersdorff, H., Vardi, E., Matthews, G. & Sterling, P. Evidence that vesicles on the synaptic ribbon of retinal bipolar neurons can be rapidly released. *Neuron* **16**, 1221–1227 (1996).

198. Jarsky, T., Tian, M. & Singer, J. H. Nanodomain control of exocytosis is responsible for the signaling capability of a retinal ribbon synapse. *J Neurosci* **30**, 11885–11895 (2010).

199. Neher, E. & Marty, A. Discrete changes of cell membrane capacitance observed under conditions of enhanced secretion in bovine adrenal chromaffin cells. *Proc National Acad Sci* **79**, 6712–6716 (1982).

200. Klyachko, V. A. & Jackson, M. B. Capacitance steps and fusion pores of small and large-dense-core vesicles in nerve terminals. *Nature* **418**, 89–92 (2002).

201. Kim, M.-H. & von Gersdorff, H. Postsynaptic plasticity triggered by Ca2+-permeable AMPA receptor activation in retinal amacrine cells. *Neuron* **89**, 507–520 (2016).

202. Hartveit, E. Membrane currents evoked by ionotropic glutamate receptor agonists in rod bipolar cells in the rat retinal slice preparation. *J Neurophysiol* **76**, 401–422 (1996).

203. Euler, T. & Masland, R. H. Light-evoked responses of bipolar cells in a mammalian retina. *J Neurophysiol* **83**, 1817–1829 (2000).

204. Singer, J. H. & Diamond, J. S. Sustained Ca2+ entry elicits transient postsynaptic currents at a retinal ribbon synapse. *J Neurosci* **23**, 10923–10933 (2003).

205. Raviola, E. & Dacheux, R. F. Excitatory dyad synapse in rabbit retina. *Proc National Acad Sci* **84**, 7324–7328 (1987).

206. Famiglietti, E. V. & Kolb, H. A bistratified amacrine cell and synaptic cirucitry in the inner plexiform layer of the retina. *Brain Res* **84**, 293–300 (1975).

207. McGuire, B., Stevens, J. & Sterling, P. Microcircuitry of bipolar cells in cat retina. *J Neurosci* **4**, 2920–2938 (1984).

208. Grimes, W. N., Zhang, J., Graydon, C. W., Kachar, B. & Diamond, J. S. Retinal parallel processors: More than 100 independent microcircuits operate within a single interneuron. *Neuron* **65**, 873–885 (2010).

209. Fletcher, E. L., Koulen, P. & Wässle, H. GABAA and GABAC receptors on mammalian rod bipolar cells. *J Comp Neurol* **396**, 351–365 (1998).

210. Palmer, M. J. Functional segregation of synaptic GABAA and GABAC receptors in goldfish bipolar cell terminals. *J Physiology* **577**, 45–53 (2006).

211. He, P. *et al.* Trophoblast glycoprotein promotes pancreatic ductal adenocarcinoma cell metastasis through Wnt/planar cell polarity signaling. *Mol Med Rep* **12**, 503–509 (2015).

212. Tsuboi, A. LRR-containing oncofetal trophoblast glycoprotein 5T4 shapes neural circuits in olfactory and Visual Systems. *Front Mol Neurosci* **13**, 581018 (2020).

213. Wachtmeister, L. Oscillatory potentials in the retina: what do they reveal. *Prog Retin Eye Res* **17**, 485–521 (1998).

214. Korol, S., Leuenberger, P. M., Englert, U. & Babel, J. In vivo effects of glycine on retinal ultrastructure and averaged electroretinogram. *Brain Res* **97**, 235–251 (1975).

215. Vaegan & Millar, T. J. Effect of kainic acid and NMDA on the pattern electroretinogram, the scotopic threshold response, the oscillatory potentials and the electroretinogram in the urethane anaesthetized cat. *Vision Res* **34**, 1111–1125 (1994).

216. Dong, C.-J., Agey, P. & Hare, W. A. Origins of the electroretinogram oscillatory potentials in the rabbit retina. *Visual Neurosci* **21**, 533–543 (2004).

217. Chen, M. & von Gersdorff, H. How to build a fast and highly sensitive sound detector that remains robust to temperature shifts. *J Neurosci* **39**, 7260–7276 (2019).

218. Kushmerick, C., Renden, R. & von Gersdorff, H. Physiological temperatures reduce the rate of vesicle pool depletion and short-term depression via an acceleration of vesicle recruitment. *J Neurosci* **26**, 1366–1377 (2006).

219. Zanazzi, G. & Matthews, G. The molecular architecture of ribbon presynaptic terminals. *Mol Neurobiol* **39**, 130–148 (2009).

220. Eggermann, E., Bucurenciu, I., Goswami, S. P. & Jonas, P. Nanodomain coupling between Ca2+ channels and sensors of exocytosis at fast mammalian synapses. *Nat Rev Neurosci* **13**, 7–21 (2012).

221. Morgans, C. W., Brandstätter, J. H., Kellerman, J., Betz, H. & Wässle, H. A SNARE complex containing syntaxin 3 is present in ribbon synapses of the retina. *J Neurosci* **16**, 6713–6721 (1996).

222. Schulz, D. J. *et al.* Cellular excitability and the regulation of functional neuronal identity: From gene expression to neuromodulation. *J Neurosci* **26**, 10362–10367 (2006).

223. Grimes, W. N. *et al.* Complex inhibitory microcircuitry regulates retinal signaling near visual threshold. *J Neurophysiol* **114**, 341–353 (2015).

224. Sinha, R. *et al.* Transient expression of a GABA receptor subunit during early development is critical for inhibitory synapse maturation and function. *Curr Biol* **31**, 4314-4326.e5 (2021).

225. Dong, C.-J. & Hare, W. A. Contribution to the kinetics and amplitude of the electroretinogram b-wave by third-order retinal neurons in the rabbit retina. *Vision Res* **40**, 579–590 (2000).

226. Dong, C.-J. & Hare, W. A. Temporal modulation of scotopic visual signals by A17 amacrine cells in mammalian retina in vivo. *J Neurophysiol* **89**, 2159–2166 (2003).

227. Widmer, F. & Caroni, P. Identification, localization, and primary structure of CAP-23, a particle-bound cytosolic protein of early development. *J Cell Biology* **111**, 3035–3047 (1990).

228. Laux, T. *et al.* Gap43, Marcks, and Cap23 modulate Pi(4,5)p2 at plasmalemmal rafts, and regulate cell cortex actin dynamics through a common mechanism. *J Cell Biol* **149**, 1455–1472 (2000).

229. Ueno, S., Miyoshi, H., Maruyama, Y., Morita, M. & Maekawa, S. Interaction of dynamin I with NAP-22, a neuronal protein enriched in the presynaptic region. *Neurosci Lett* **675**, 59–63 (2018).

230. Takaichi, R. *et al.* Inhibitory effect of NAP-22 on the phosphatase activity of synaptojanin-1. *J Neurosci Res* **90**, 21–27 (2012).

231. Han, M.-H. *et al.* The novel caspase-3 substrate Gap43 is involved in AMPA receptor endocytosis and long-term depression. *Mol Cell Proteomics* **12**, 3719–3731 (2013).

232. HaileMariam, M. *et al.* S-Trap, an ultrafast sample-preparation approach for shotgun proteomics. *J Proteome Res* **17**, 2917–2924 (2018).

233. Yu, Q. *et al.* Benchmarking the Orbitrap Tribrid Eclipse for next generation multiplexed proteomics. *Anal Chem* **92**, 6478–6485 (2020).

234. Nishikawa, K., Toker, A., Johannes, F.-J., Songyang, Z. & Cantley, L. C. Determination of the specific substrate sequence motifs of protein kinase C isozymes. *J Biol Chem* **272**, 952–960 (1997).

235. von Gersdorff, H. & Matthews, G. Depletion and replenishment of vesicle pools at a ribbon-type synaptic terminal. *J Neurosci* **17**, 1919–1927 (1997).

236. Gomis, A., Burrone, J. & Lagnado, L. Two actions of calcium regulate the supply of releasable vesicles at the ribbon synapse of retinal bipolar cells. *J Neurosci* **19**, 6309–6317 (1999).

237. Singer, J. H. & Diamond, J. S. Vesicle depletion and synaptic depression at a mammalian ribbon synapse. *J Neurophysiol* **95**, 3191–3198 (2006).

238. Abdeljalil, J. *et al.* The optomotor response: A robust first-line visual screening method for mice. *Vision Res* **45**, 1439–1446 (2005).